Doctoral Dissertations and Master's Theses

Fall 12-14-2023

Verification and Validation of Robot Manipulator Adaptive Control with Actuator Deficiency

Sebastian Comeaux
Embry-Riddle Aeronautical University, comeauxs@my.erau.edu

Follow this and additional works at: https://commons.erau.edu/edt

Part of the Navigation, Guidance, Control and Dynamics Commons

By

A Thesis Submitted to the Faculty of Embry-Riddle Aeronautical University

In Partial Fulfillment of the Requirements for the Degree of

Master of Science in Aerospace Engineering

Embry-Riddle Aeronautical University

Daytona Beach, Florida

By

THESIS COMMITTEE

_____   _____

_____

_____   _____
Graduate Program Coordinator,   Date
Dr. Hever Moncayo

_____   _____
Dean of the College of Engineering,   Date
Dr. James W. Gregory

_____   _____
Associate Provost of Academic Support,   Date
Dr. Kelly Austin

All the power and glory to my Heavenly Father, whose steadfast love is only rivaled by my mother's and father's, whose support for my dreams has never wavered.

ACKNOWLEDGMENTS

ABSTRACT

This work addresses the joint tracking problem of robotic manipulators with uncertain dynamical parameters and actuator deficiencies, in the form of an uncertain control effectiveness matrix, through adaptive control design, simulation, and experimentation. Specifically, two novel adaptive controller formulations are implemented and tested via simulation and experimentation. The proposed adaptive control formulations are designed to compensate for uncertainties in the dynamical system parameters as well as uncertainties in the control effectiveness matrix that pre-multiplies the control input. The uncertainty compensation of the dynamical parameters is achieved via the use of the desired model compensation–based adaptation, while the uncertainties related to the control effectiveness matrix are dealt with via two fundamentally different novel adaptation methods, namely with bound-based and projection operator-based methods. The stability of the system states and convergence of the error terms to the origin are proven via Lyapunov–based arguments. Extensive numerical studies are performed on a two–link planar robotic device, and experimental studies are preformed on Quansers QArm to illustrate the effectiveness of both adaptive controllers. In the experimental validation of the theory, both adaptive controllers demonstrate remarkable resilience, maintaining control of the Quanser QArm even with up to an 80% control input deficiency. After tuning the gains, both joints satisfactorily tracked the desired trajectories. When evaluating the entire experiment, the norm of the square of the total error is averaged. The bound-based controller exhibited an average error of $2.816°$ across all cases, while the projection operator-based controller had a reduced average error of $1.012°$ across all cases. Furthermore, over time, there is a noticeable decrease in error for both joints. These results underscore the robustness and effectiveness of the proposed adaptive controllers, even under substantial actuator deficiencies. The results highlight the significance of achieving near-perfect system knowledge and the careful selection of controls for desirable system performance.

TABLE OF CONTENTS

LIST OF FIGURES

Figure   **Page**

Figure   **Page**

Figure   **Page**

LIST OF TABLES

<div align="center">

Nomenclature

</div>

$(\cdot)^{\mathrm{T}}$	Transpose
$(\cdot)^{-1}$	Inverse
$\triangleq$	Equality by definition
$\lVert \cdot \rVert$	Euclidean norm of a matrix
$\lvert \cdot \rvert$	Norm of a variable
$\mathrm{diag}(a)$	Diagonal matrix with the entries of vector a on its diagonal
$\mathrm{Proj}(\cdot, \cdot)$	Projection operator
$\mathbb{R}$	Set of real numbers
$\mathbb{R}^{n}$	Set of $n \times 1$ real column vectors
$\mathbb{R}^{n \times p}$	Set of $n \times p$ real matrices
$\mathbb{R}_{+}$	Set of positive real numbers
$\mathbb{D}^{n \times n}$	Set of $n \times n$ real matrices with diagonal scalar entries
$\mathbb{D}_{+}^{n \times n}$	Set of $n \times n$ positive-definite real matrices with diagonal scalar entries
I_{n}	$n \times n$ identity matrix
$\lambda_{min}(A)$	Minimum eigenvalue of the matrix $A \in \mathrm{R}^{n \times n}$
θ_{i}	i^{th} Joint angle
$\dot{\theta}_{i}$	Joint angular velocity
$\ddot{\theta}_{i}$	Joint angular acceleration
ϕ_{i}	New mapped joint angle parameter

τ_i	i^{th} Joint torque
$\tau(t)$	Control input vector
Λ	Control effectiveness matrix
λ_{ci}	Distance to center of mass
L_i	Original arm length parameter
ϕ_i	New mapped i^{th} joint angle parameter
β	Angle between L_2 and λ_2
m_i	Mass of the ith link
I_i	i^{th} mass moment of inertia
T_i	Kinetic energy
P_i	Potential energy
λ_i	New mapped arm length parameter
$\mathbf{b}_i$	Standard basis vector with its ith entry being one and all other entries being zero
$(\cdot)_{mn}$	Relating the torque on the mth joint to the corresponding n^{th} kinematic term
$(\cdot)_i$	Corresponding to the ith joint
x	System state
y	System output
$q(t)$	Joint positions
$\dot{q}(t)$	Joint velocities
$\ddot{q}(t)$	Joint accelerations

$q_d, \dot{q}_d, \ddot{q}_d$	Desired joint positions, velocities, and accelerations
$M(q)$	Positive definite and symmetric inertia matrix
$M(q_d)$	Desired inertia matrix
$N(q, \dot{q})$	Nonlinear terms in the robot model
$N(q_d, \dot{q}_d)$	Desired nonlinear terms
V_m	Centripetal-Coriolis matrix
F_d	Friction matrix
$G(q)$	Gravity matrix
$G(q_d)$	Desired gravity matrix
$e(t)$	Joint level tracking error term
$r(t)$	Filtered tracking error term
ϕ	Unknown model parameter vector
$\hat{\phi}(t)$	Estimation of an unknown model parameter vector
$\tilde{\phi}(t)$	Estimation error of the unknown model parameter vector
δ_Λ	Unknown part of the control effectiveness matrix
$\hat{\delta}_\Lambda(t)$	Estimation of the unknown part of the control effectiveness matrix
$\tilde{\delta}_\Lambda(t)$	Estimation error of the unknown part of the control effectiveness matrix
$r(t)$	Filtered tracking error
K_r	Control gain matrix
k_n	Damping gain

μ	Constant, positive definite, proportional, and diagonal control gain matrix
Γ	Constant and diagonal learning rate matrix for $\hat{\phi}(t)$
γ	Constant and diagonal learning rate matrix for $\hat{\delta}_\Lambda(t)$
$Y(q,\dot{q},\ddot{q})$	Regressor matrix
$Y_\mathrm{d}(q_\mathrm{d},\dot{q}_\mathrm{d},\ddot{q}_\mathrm{d})$	Desired version of the regression matrix
$\mathscr{X}(t)$	Auxiliary term
$z(t)$	Combined error vector
$\rho(\cdot), \rho_1(\cdot), \rho_2(\cdot)$	Positive bounding functions
$\zeta_1, \zeta_2, \zeta_3, \zeta_4$	Known constant positive bounds
Ω	Convex hypercube with minimum and maximum bounds for the parameter vector
Ω_{ε_0}	Another convex hypercube within Ω with adjusted bounds
$\theta_i^{min}, \theta_i^{max}$	Minimum and maximum bounds for the ith component of the parameter vector
ε_0	Sufficiently small constant
c_i	$\cos(i^{th}$ joint angle)
s_i	$\sin(i^{th}$ joint angle)
c_{ij}	$\cos(i^{th}$ joint angle $+ j^{th}$ joint angle)
s_{ij}	$\sin(i^{th}$ joint angle $+ j^{th}$ joint angle)
i	Current
R	Resistance
L	Inductance

$\frac{di}{dt}$ Rate of change of current

K_e Back electromotive force (EMF) constant

K_t Motor torque constant

PID   Proportional, integral, derivative

PWM   Pulse width modulation

SAC   Standard adaptive controller

BAC   Bound-based adaptive controller

PAC   Projection operator-based adaptive controller

1 Introduction

This thesis delves into the critical exploration of the implementation of adaptive control of robotic manipulators, particularly under the influence of uncertainties and actuator deficiencies. Chapter 1 elucidates the significance of this research and provides a diverse review of relevant literature. Chapter 2 offers an in-depth background on the Quanser QArm, including the derivation of necessary equations of motion, providing context for the theoretical constructs validated using the Quanser QArm robotic manipulator. In Chapter 3, the model formulation for a standard adaptive controller is presented, complemented by motivational experimental results. This is succeeded by the exposition of the theoretical contributions to the dynamic model. Chapter 4 and Chapter 5 respectively detail the simulation results and the experimental results, including a discussion on these findings. Finally, Chapter 6 provides a conclusion to this work.

1.1 Importance of Research

This research addresses the challenging and relevant problem of adaptive control of robotic manipulators with uncertain dynamical parameters and actuator deficiencies. These uncertainties can affect the performance and stability of the robotic manipulators, especially in scenarios where precise and robust tracking is required [4]. The existing methods for adaptive control of robotic manipulators have some limitations, such as requiring exact knowledge of the control effectiveness matrix, assuming constant or bounded uncertainties, or relying on fault detection and isolation schemes. This thesis fundamentally builds upon the work presented in [5], which introduced innovative adaptive controller designs to compensate for the unknown control effectiveness matrix. In fact, this thesis primarily focuses on the verification and experimental validation of this paper's theoretical constructs. Therefore, substantial portions of the original work from this paper are replicated in this thesis to provide a comprehensive context for the experimental validation. The technical objectives of this thesis are to experimentally validate the theoretical and simulated results presented in the referenced paper and to maintain control of a robotic manipulator with potentially high actuator deficiencies.

The foundational research of this thesis makes several significant contributions and introduces

novel concepts. Firstly, it presents a new Lyapunov-like function, a new projection operator-based design, and a new bound-based design, for the adaptive control of robotic manipulators with actuator deficiencies. Secondly, it establishes the asymptotic stability and tracking performance of the robotic manipulators under both controller designs. Lastly, this thesis validates theoretical results through both numerical simulations on a 2-degree-of-freedom serial robotic arm and experimental studies using the Quanser QArm robotic manipulator.

The implications of this research are far-reaching. It enhances the robustness and effectiveness of robotic manipulators in various scenarios, including industrial automation, medical robotics, and space exploration. It also provides new insights and tools for adaptive control theory and, more importantly, that they work in practice.

Furthermore, there are many possible future directions and open problems that can follow this work. These include extending the results to cooperative or networked robot systems, dealing with nonlinear and time-varying uncertainties, designing output feedback controllers, and incorporating learning mechanisms. This work serves as a stepping stone for further advancements in this field.

1.2 Review of the Relevant Literature

A significant challenge in the realm of robot manipulator control pertains to compensating for dynamic and/or kinematic uncertainties. From a theoretical standpoint, when the dynamic model of a robot manipulator exhibits structured or parametric uncertainties, adaptive control techniques become the preferred approach. To address kinematic uncertainties, several research efforts have focused on adaptive task space tracking control. In [6], Cheah introduced an adaptive law for estimating uncertain kinematic model parameters, particularly for the approximate Jacobian method. Notably, this method does not necessitate task space velocity and the inverse of the approximate Jacobian matrix. Cheah et al. [7, 8] proposed an approximate Jacobian controller for robot manipulators with uncertainties in kinematics and Jacobian, all without relying on task space velocity and the inverse Jacobian matrix. In [9], Cheah presented methods involving approximate transpose Jacobian and inverse Jacobian for set-point control of non-redundant robots with parametric kinematic uncertainties. For dynamic uncertainties, adaptive control formulations have been ex-

plored in several works. Zergeroglu et al. [10], Xian et al. [11] feature an adaptive controller designed to achieve asymptotic operational space tracking despite parametric uncertainties related to the dynamic model. Tatlicioglu et al. [12, 13] developed a quaternion-based adaptive full-state feedback controller for redundant robot manipulators afflicted by parametric uncertainties in their dynamic model. Tatlicioglu et al. [14, 15] present an adaptive feedback linearizing control strategy to compensate for parametric uncertainties in dynamics.

In the realm of addressing uncertainties in robot control, the literature explores various learning-based control strategies. Initial contributions to repetitive learning control in the context of robotic systems have been made by researchers [16–18]. However, it is important to note that these control schemes can only ensure asymptotic convergence under specific and restrictive conditions on the underlying plant dynamics. To enhance the robustness of the control methods put forth in [16] and [17], modifications have been introduced in the form of a so-called Q-filter within the repetitive update rule. Furthermore, in an effort to improve the robustness of the previously proposed repetitive learning algorithm, researchers in [19] and [20] have devised a scheme that leverages the use of Kernel functions in the update rule. In their pursuit of enhancing the robustness of repetitive learning controllers, Sadegh et al. [21] introduce a saturated update rule. Additionally, in [22], the authors present a full-state feedback learning controller that not only achieves asymptotic tracking but is also supported by a stability analysis based on Lyapunov principles. In [23], [24], and [25], a novel approach is taken by employing a model-free observer in conjunction with an innovative feedforward learning component. This approach resulted in the design of an output feedback repetitive learning controller tailored for robotic manipulators with periodic trajectories. Importantly, this method ensures asymptotic tracking despite the uncertainties stemming from the robot's dynamics and the absence of velocity measurements. In [26], an adaptive operational space controller is introduced for redundant robots, considering time-varying uncertainties and tasks without knowledge of their bounds. Recent research has also delved into adaptive control for robot end-effector motion, as seen in [27] and [28]. It is worth noting that nearly all of these approaches require the robot dynamics to conform to a specific form, typically the linear parametrization

3

property.

In the pursuit of addressing the complex problem of joint tracking in robotic manipulators with uncertain dynamical parameters and actuator deficiencies, numerous researchers have proposed diverse methodologies [4, 29–39].

1.2.1 Relevant Approaches in the Presence of Unknown Control Effectiveness

Here, various strategies that have been employed to control uncertain robotic manipulators with unknown control effectiveness are given, with their unique perspectives and solutions. In robotic manipulator dynamics, the diminution in effectiveness is conceptualized as a constant, diagonal matrix that multiplies the control input [30]. This matrix is referred to by various names such as the control effectiveness matrix [34–36], actuator torque coefficient matrix [30], transmission matrix [37], constant torque matrix [38], and actuator health condition matrix [39]. In this work, however, the term control effectiveness matrix is favored. From a control-theoretic perspective, the uncertainty of the control effectiveness matrix implies that the control input is not relayed to the system as intended, necessitating the need for compensation. By examining these varied approaches, we aim to gain a deeper understanding of the problem at hand and the effectiveness of our proposed adaptive controllers in comparison. Below, a summary of relevant approaches are given.

Liu et al. [30] present an online monitoring system of actuator degradation and failures, where an adaptive fault-tolerant control method for robot manipulators is used. Specifically, the paper introduces a new parametric dynamic model that incorporates the actuator torque coefficients and proposes an adaptive control scheme that can compensate for the model uncertainty and monitor the actuator performance on-line. The authors also discuss how the proposed algorithm can be used to detect actuator failures using the parameter deviation and commanded torque magnitude as indicators. The paper demonstrates the effectiveness of the proposed method through theoretical analysis and simulation results. The drawback of the method given in this paper is using over-parameterization, which complicates the solution.

Tao et al. [29] present an adaptive actuator failure compensation scheme for a cooperative

manipulator system with parameter uncertainties. The scheme uses multiple individual failure compensators and direct adaptation of controller parameters to handle uncertain actuator failures and parameter uncertainties. The scheme ensures closed-loop stability and asymptotic output tracking of the system output, despite the failures. The effectiveness of the scheme is verified by simulation results of a benchmark cooperative manipulator system with two degrees of freedom and three actuators. The difference of the methods given in this paper is that the formulation is based on task-space (not joint-space) control.

Luca et al. [31] present a method for detecting and isolating actuator faults in robot manipulators using generalized momenta. The method does not require acceleration estimates or simulation of the nominal robot dynamics and covers a general class of input faults. The method is based on comparing the nominal input torque and the generalized momenta, which are decoupled from the effects of faults and inputs. The method generates residuals that are linearly driven by the faults and can be used for fault identification. The method is tested on a two-revolute joint planar robot under gravity and different types of actuator faults and shows good performance in reconstructing the faults and a decoupled behavior of the residuals. The authors also discuss the advantages of using generalized momenta for fault detection and isolation and the limitations of the method in terms of model accuracy and disturbance rejection. The drawback of the method given in this paper is using the results in Liu [30] with less computation required but still using over-parameterization

2 QArm Model

In this section, a comprehensive overview of the experimental plant, specifically the QArm robotic manipulator, is provided. This includes detailed specifications and the underlying dynamic equations, thereby establishing a robust context for the forthcoming experimental results. Subsequently, we elucidate the transformation process between the output of the adaptive controller, namely the commanded torque, and the corresponding input of the QArm robotic manipulator.

2.1 QArm Dynamics

For the experimental results of this thesis, the Quanser QArm Modern Manipulator Arm is used, which is a 4-degree-of-freedom (DOF) serial robotic manipulator with a tendon-based two-stage gripper and an RGBD camera. The QArm is designed for modern engineering education and academic research applications [2]. See Figure 2.1 for the QArm in the FAST Lab at Embry-Riddle Aeronautical University.
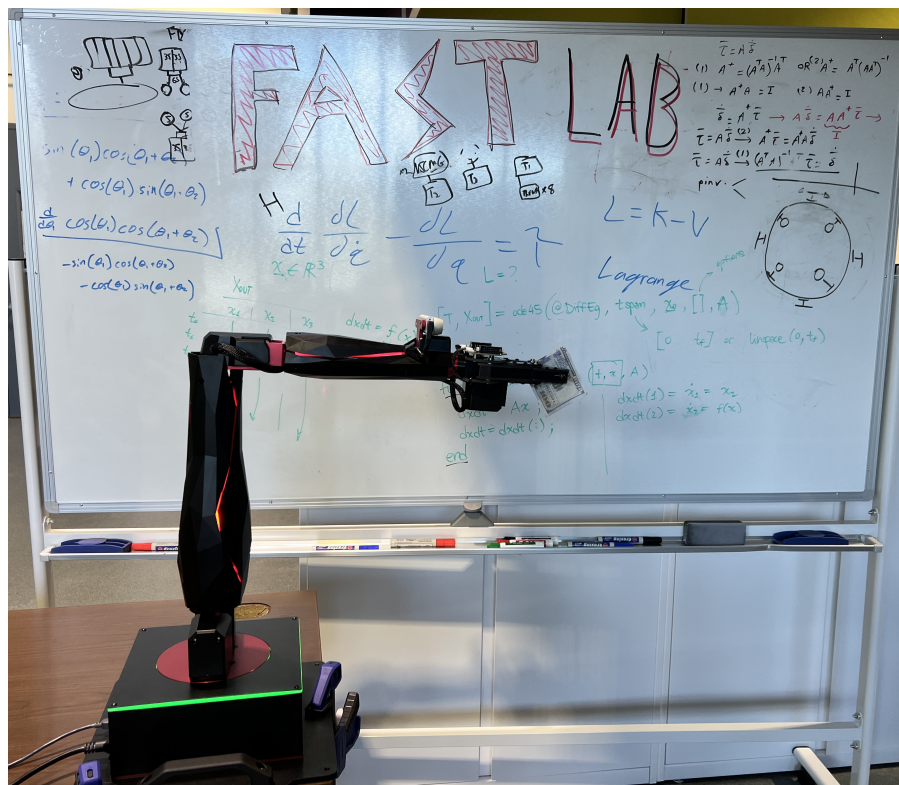
Figure 2.1 Picture of the Quanser QArm in the FAST Lab. FAST Lab website: [1]

To use the QArm most effectively for research purposes it is important to understand its geometry, dynamics, kinematics, and built-in control system. If the tip of the two-stage gripper arm is located at some point in space that we call $\vec{p}$, then this point can be defined by its position vector, $[p_x, p_y, p_z]^T$, called the task space, or some combination of joint angles, $[\theta_1 \ \theta_2 \ \theta_3 \ \theta_4]$, called the joint space.

The dynamics of the QArm represent a highly complex nonlinear system that describes the motion of the 4 joints of the system: the base joint, the shoulder joint, the elbow joint, and the wrist joint. The geometry of the system can be seen in Figure 2.2, where the lengths of each arm the location of each joint and their corresponding joint frame, as well as how each of the direction of joint angles and angular velocities, are shown.
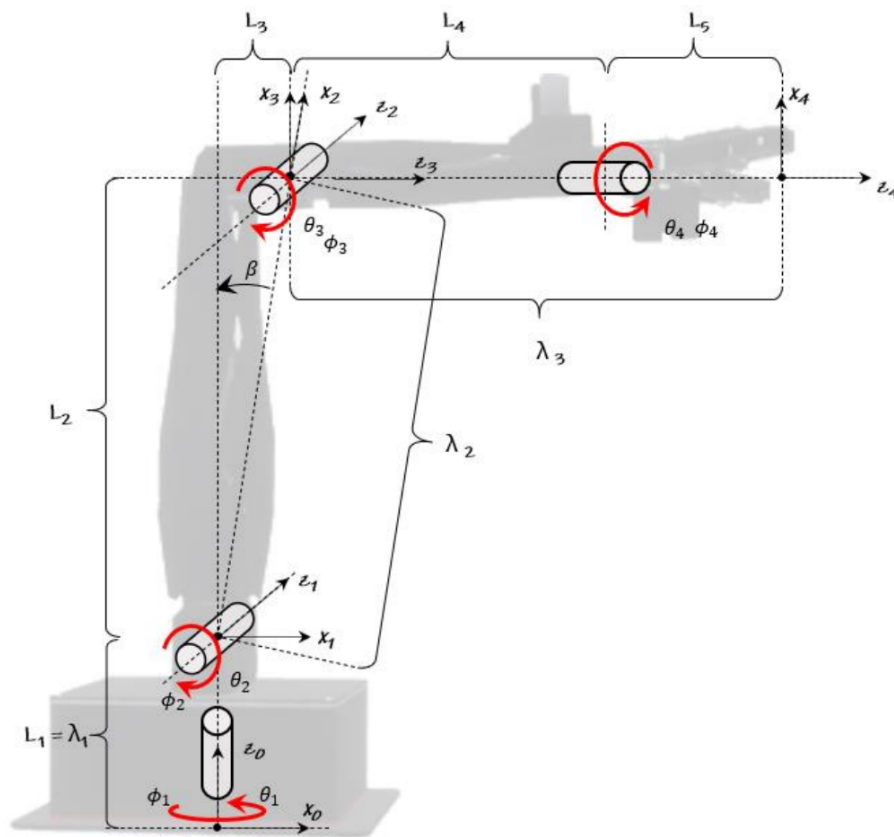
Figure 2.2 Frame diagram for the Quanser QArm manipulator [2].

Furthermore, as the arm moves, the locations of the centers of mass of each link change which affects the dynamics of the system, as illustrated in Figure 2.3. Studying these figures can help in understanding the dynamics of the system, specifically how each link interacts with other links.
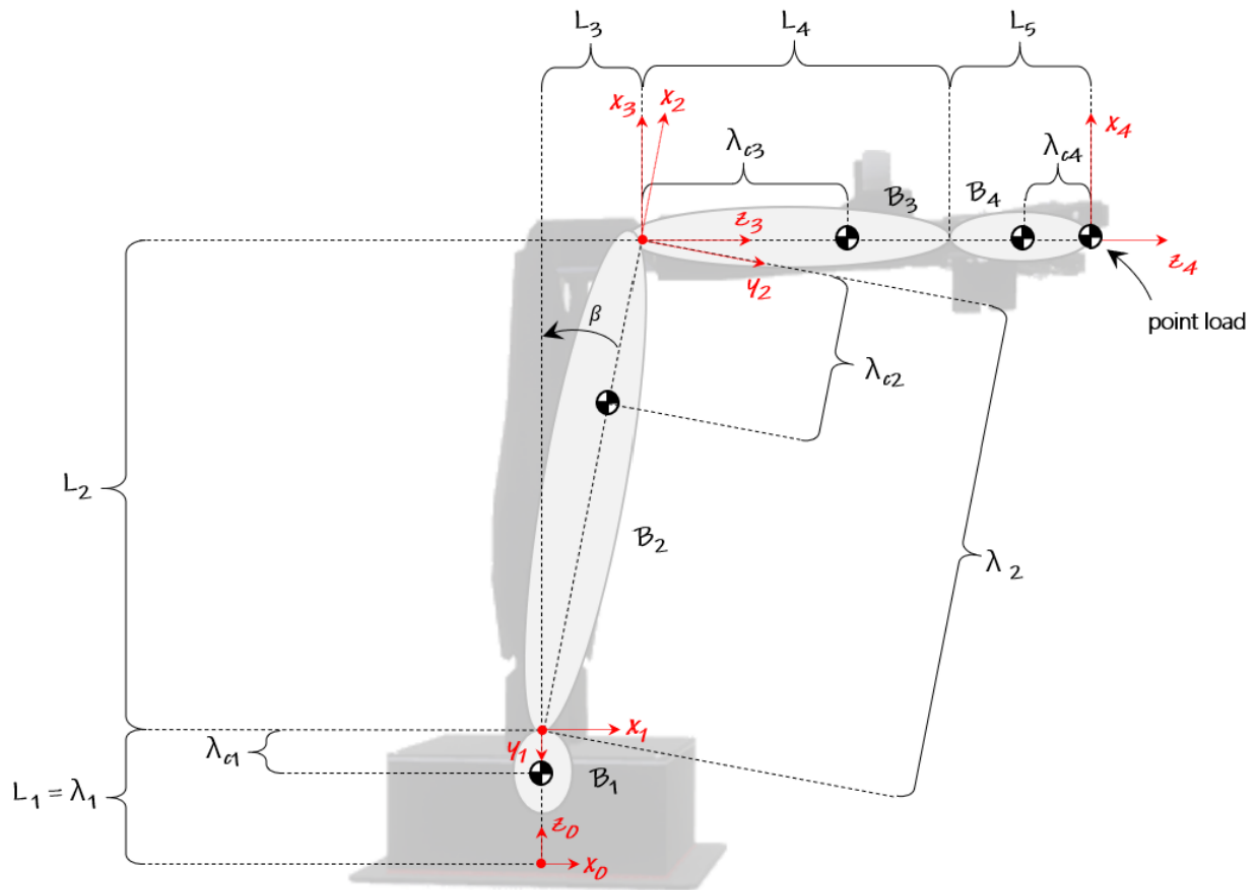
Figure 2.3 Rigid body diagram for the Quanser QArm manipulator [2].

The QArm is capable of two types of kinematics: forward kinematics and inverse kinematics. Forward kinematics uses transformation matrices to provide a mapping from the joint space to the task space. Inverse kinematics uses transformation matrices to do the opposite and provide a mapping from task space to joint space. The system can also be described using the Lagrangian, which uses the kinetic energies T_i and potential energies P_i of the system joint to derive the equations of motion. This thesis uses the joint space to control the robotic manipulator using novel adaptive

controllers. It is important to understand the Lagrangian dynamics because they are how the joint torques are derived.

The equations of motion are derived using the Lagrangian method; however, for the purposes of this thesis, a full derivation of the kinetic and potential energies is not given. These derivations can be found on the Quanser QArm website under "USER MANUALS" [2]. To create the mathematical model of the nonlinear system, this section starts with the completed Lagrangian to obtain the equations of motion. The Lagrangian in this system is defined as the sum of all the kinetic and potential energies of each joint, which is expressed in Equation (2.1).

$$\mathcal{L} = \sum_{n=1}^{4} T_n - \sum_{n=1}^{4} P_n \tag{2.1}$$

Plugging in the values for T_n (kinetic energy) and P_n (potential energy) for each joint and calculating the summation we get Equation 2.2,

$$
\begin{aligned}
\mathcal{L} = \Bigg(&\frac{1}{2}I_{1A} + \frac{1}{2}m_2\left(\lambda_2 - \lambda_{c2}\right)^2 c_2^2 + \frac{1}{2}I_{2A}s_2^2 + \frac{1}{2}I_{2L}c_2^2 + \frac{1}{2}m_3\lambda_2^2c_2^2 + \frac{1}{2}m_3\lambda_{c3}^2s_{23}^2 \\[2mm]
&-m_3\lambda_2\lambda_{c3}c_2s_{23} + \frac{1}{2}I_{3L}s_{23}^2 + \frac{1}{2}I_{3A}c_{23}^2 + \frac{1}{2}m_4\left(\lambda_3 - \lambda_{c4}\right)^2 s_{23}^2 + \frac{1}{2}m_4\lambda_2^2c_2^2 \\[2mm]
&-m_4\left(\lambda_3 - \lambda_{c4}\right)\lambda_2c_2s_{23} + \frac{1}{2}I_{4L}s_{23}^2 + \frac{1}{2}I_{4A}c_{23}^2 \\[2mm]
&+\frac{1}{2}m_L\lambda_3^2s_{23}^2 + \frac{1}{2}m_L\lambda_2^2c_2^2 - m_L\lambda_2\lambda_3c_2s_{23} \Bigg)\dot{\theta}_1^2 \\[2mm]
&+ \Bigg(\frac{1}{2}m_2\left(\lambda_2 - \lambda_{c2}\right)^2 + \frac{1}{2}I_{2L} + \frac{1}{2}m_3\lambda_2^2 + \frac{1}{2}m_3\lambda_{c3}^2 - m_3\lambda_2\lambda_{c3}s_3 + \frac{1}{2}I_{3L} \\[2mm]
&+\frac{1}{2}m_4\left(\lambda_2 + \lambda_3 - \lambda_{c4}\right)^2 + \frac{1}{2}I_{4L} + \frac{1}{2}m_L\lambda_2^2 + \frac{1}{2}m_L\lambda_3^2 - m_L\lambda_2\lambda_3s_3 \Bigg)\dot{\theta}_2^2 \\[2mm]
&+ \Bigg(\frac{1}{2}m_3\lambda_{c3}^2 + \frac{1}{2}I_{3L} + \frac{1}{2}m_4\left(\lambda_{c4} - \lambda_3\right)^2 + \frac{1}{2}I_{4L} + \frac{1}{2}m_L\lambda_3^2 \Bigg)\dot{\theta}_3^2 \\[2mm]
&+ \Bigg(\frac{1}{2}I_{4A} \Bigg)\dot{\theta}_4^2 - \Bigg(I_{4A}c_{23} \Bigg)\dot{\theta}_1\dot{\theta}_4
\end{aligned}
$$

9

$$+\left(m_3\lambda_{c3}^2 - m_3\lambda_{c3}\lambda_2 s_3 + I_{3L} + m_4\left(\lambda_3 - \lambda_{c4} - \lambda_2 s_3\right)\left(\lambda_3 - \lambda_{c4}\right)\right.$$

$$\left.+I_{4L} - m_L\left(\lambda_3^2 - \lambda_2\lambda_3 s_3\right)\right)\dot{\theta}_2\dot{\theta}_3$$

$$-m_1 g\left(\lambda_1 - \lambda_{c1}\right) - m_2 g\left(\lambda_1 - \left(\lambda_2 - \lambda_{c2}\right)s_2\right) - m_3 g\left(\lambda_1 - \lambda_2 s_2 - \lambda_{c3}c_{23}\right)$$

$$-m_4 g\left(\lambda_1 - \lambda_2 s_2 - \left(\lambda_3 - \lambda_{c4}\right)c_{23}\right) - m_L g\left(\lambda_1 - \lambda_2 s_2 - \lambda_3 c_{23}\right). \tag{2.2}$$

For the experimental results of this thesis, only the shoulder and elbow joints, θ_2 and θ_3, are used; therefore the equations for the torque of the base and wrist do not need to be derived. The following equation can be used to derive the necessary joint torques, which are the inputs into the system:

$$\tau_i = \frac{d}{dt}\left(\frac{d\mathscr{L}}{d\dot{\theta}_i}\right) - \frac{d\mathscr{L}}{d\theta_i}. \tag{2.3}$$

The second joint is the shoulder joint, which sits just above the top of the control box and has a range of motion between $-85°$ and $+85°$. This joint is very complicated because it must take into account the moment of inertia of every joint beside the base, which has a small moment of inertia (MOI). The torque required by this joint is given by

$$\tau_2 = \frac{d}{dt}\left(\frac{d\mathscr{L}}{d\dot{\theta}_2}\right) - \frac{d\mathscr{L}}{d\theta_2}. \tag{2.4a}$$

$$\frac{d\mathscr{L}}{d\dot{\theta}_2} = \left(m_2\left(\lambda_2 - \lambda_{c2}\right)^2 + I_{2L} + m_3\lambda_2^2 + m_3\lambda_{c3}^2 - 2m_3\lambda_2\lambda_{c3}s_3 + I_{3L}\right.$$

$$\left.+m_4\left(\lambda_2 + \lambda_3 - \lambda_{c4}\right)^2 + I_{4L} + m_L\lambda_2^2 + m_L\lambda_3^2 - 2m_L\lambda_2\lambda_3 s_3\right)\dot{\theta}_2$$

$$+\left(m_3\lambda_{c3}^2 - m_3\lambda_{c3}\lambda_2 s_3 + I_{3L}\right.$$

$$\left.+m_4\left(\lambda_3 - \lambda_{c4} - \lambda_2 s_3\right)\left(\lambda_3 - \lambda_{c4}\right) + I_{4L} - m_L\left(\lambda_3^2 - \lambda_2\lambda_3 s_3\right)\right)\dot{\theta}_3. \tag{2.4b}$$

$$\frac{d}{dt}\left(\frac{d\mathscr{L}}{d\dot{\theta}_2}\right) = \left(m_2\left(\lambda_2 - \lambda_{c2}\right)^2 + I_{2L} + m_3\lambda_2^2 + m_3\lambda_{c3}^2 - 2m_3\lambda_2\lambda_{c3}s_3 + I_{3L}\right.$$

$$+m_4\left(\lambda_2+\lambda_3-\lambda_{c4}\right)^2+I_{4L}+m_L\lambda_2^2+m_L\lambda_3^2-2m_L\lambda_2\lambda_3s_3\Big)\ddot{\theta}_2$$

$$+\Big(m_3\lambda_{c3}^2-m_3\lambda_{c3}\lambda_2s_3+I_{3L}$$

$$+m_4\left(\lambda_3-\lambda_{c4}-\lambda_2s_3\right)\left(\lambda_3-\lambda_{c4}\right)+I_{4L}-m_L\left(\lambda_3^2-\lambda_2\lambda_3s_3\right)\Big)\ddot{\theta}_3$$

$$-\Big(2m_3\lambda_2\lambda_{c3}c_3+2m_L\lambda_2\lambda_3c_3\Big)\dot{\theta}_2\dot{\theta}_3$$

$$-\Big(m_3\lambda_{c3}\lambda_2c_3+m_4\lambda_2c_3\left(\lambda_3-\lambda_{c4}\right)-m_L\left(\lambda_2\lambda_3c_3\right)\Big)\dot{\theta}_3^2. \tag{2.4c}$$

$$\frac{d\mathscr{L}}{d\theta_2}=\Big(-m_2\left(\lambda_2-\lambda_{c2}\right)^2s_2c_2+I_{2A}s_2c_2-I_{2L}s_2c_2-m_3\lambda_2^2s_2c_2+m_3\lambda_{c3}^2s_{23}c_{23}$$

$$+m_3\lambda_2\lambda_{c3}s_2s_{23}-m_3\lambda_2\lambda_{c3}c_2c_{23}+I_{3L}S_{23}c_{23}-I_{3A}s_{23}c_{23}+m_4\left(\lambda_3-\lambda_{c4}\right)^2s_{23}c_{23}$$

$$-m_4\lambda_2^2s_2c_2+m_4\left(\lambda_3-\lambda_{c4}\right)\lambda_2s_2s_{23}-m_4\left(\lambda_3-\lambda_{c4}\right)\lambda_2c_2c_{23}+I_{4L}s_{23}c_{23}$$

$$-I_{4A}s_{23}c_{23}+m_L\lambda_3^2s_{23}c_{23}-m_L\lambda_2^2s_2c_2+m_L\lambda_2\lambda_3s_2s_{23}-m_L\lambda_2\lambda_3c_2c_{23}\Big)\dot{\theta}_1^2$$

$$+\Big(I_{4A}s_{23}\Big)\dot{\theta}_1\dot{\theta}_4+m_2g\left(\lambda_2-\lambda_{c2}\right)c_2+m_3g\left(\lambda_2c_2-\lambda_{c3}s_{23}\right)$$

$$+m_4g\left(\lambda_2c_2-\left(\lambda_3-\lambda_{c4}\right)s_{23}\right)+m_Lg\left(\lambda_2c_2-\lambda_3s_{23}\right). \tag{2.4d}$$

Plugging in Equations 2.4b, 2.4c, and 2.4d, into 2.4a, one obtains:

$$\tau_2=\Big(m_2\left(\lambda_2-\lambda_{c2}\right)^2+I_{2L}+m_3\lambda_2^2+m_3\lambda_{c3}^2-2m_3\lambda_2\lambda_{c3}s_3+I_{3L}+m_4\lambda_2+\lambda_3$$

$$-\lambda_{c4}^2+I_{4L}+m_L\lambda_2^2+m_L\lambda_3^2-2m_L\lambda_2\lambda_3s_3\Big)\ddot{\theta}_2$$

$$+\Big(\{m_3\lambda_{c3}^2-m_3\lambda_{c3}\lambda_2s_3+I_{3L}+m_4\left(\lambda_3-\lambda_{c4}-\lambda_2s_3\right)\left(\lambda_3-\lambda_{c4}\right)$$

$$+I_{4L}-m_L\left(\lambda_3^2-\lambda_2\lambda_3s_3\right)\Big)\ddot{\theta}_3$$

$$-\Big(-m_2\left(\lambda_2-\lambda_{c2}\right)^2s_2c_2+I_{2A}s_2c_2-I_{2L}s_2c_2-m_3\lambda_2^2s_2c_2+m_3\lambda_{c3}^2s_{23}c_{23}$$

$$+m_3\lambda_2\lambda_{c3}s_2s_{23}-m_3\lambda_2\lambda_{c3}c_2c_{23}+I_{3L}s_{23}c_{23}-I_{3A}s_{23}c_{23}+m_4\left(\lambda_3-\lambda_{c4}\right)^2s_{23}c_{23}$$

$$-m_4\lambda_2^2 s_2 c_2 + m_4\left(\lambda_3 - \lambda_{c4}\right)\lambda_2 s_2 s_{23} - m_4\left(\lambda_3 - \lambda_{c4}\right)\lambda_2 c_2 c_{23} + I_{4L} s_{23} c_{23}$$

$$-I_{4A} s_{23} c_{23} + m_L\lambda_3^2 s_{23} c_{23} - m_L\lambda_2^2 s_2 c_2 + m_L\lambda_2\lambda_3 s_2 s_{23} - m_L\lambda_2\lambda_3 c_2 c_{23}\Big)\dot{\theta}_1^2$$

$$-\left(m_3\lambda_{c3}\lambda_2 c_3 + m_4\lambda_2 c_3\left(\lambda_3 - \lambda_{c4}\right) - m_L\left(\lambda_2\lambda_3 c_3\right)\right)\dot{\theta}_3^2 - \left(I_{4A} s_{23}\right)\dot{\theta}_1\dot{\theta}_4$$

$$-\left(2m_3\lambda_2\lambda_{c3} c_3 + 2m_L\lambda_2\lambda_3 c_3\right)\dot{\theta}_2\dot{\theta}_3$$

$$-g\Big(m_2\left(\lambda_2 - \lambda_{c2}\right)c_2 + m_3\left(\lambda_2 c_2 - \lambda_{c3} s_{23}\right)$$

$$+m_4\left(\lambda_2 c_2 - \left(\lambda_3 - \lambda_{c4}\right)s_{23}\right) + m_L\left(\lambda_2 c_2 - \lambda_3 s_{23}\right)\Big). \tag{2.5}$$

The third joint is the elbow joint, which has a rotation point that is not directly in line with the l_3 arm. There is some additional length from the center-line of link 1 to the rotation axis of the elbow, denoted l_2, in the x_1 direction which we can represent by the angle β, as shown in Figure 2.3. The elbow can rotate between a range of $-95°$ to $+75°$. The torque required by the third joint is given by

$$\tau_3 = \frac{d}{dt}\left(\frac{d\mathscr{L}}{d\dot{\theta}_3}\right) - \frac{d\mathscr{L}}{d\theta_3}. \tag{2.6a}$$

$$\frac{d\mathscr{L}}{d\dot{\theta}_3} = \left(m_3\lambda_{c3}^2 + I_{3L} + m_4\left(\lambda_{c4} - \lambda_3\right)^2 + I_{4L} + m_L\lambda_3^2\right)\dot{\theta}_3$$

$$+\Big(m_3\lambda_{c3}^2 - m_3\lambda_{c3}\lambda_2 s_3 + I_{3L} + m_4\left(\lambda_3 - \lambda_{c4} - \lambda_2 s_3\right)\left(\lambda_3 - \lambda_{c4}\right)$$

$$+I_{4L} - m_L\left(\lambda_3^2 - \lambda_2\lambda_3 s_3\right)\Big)\dot{\theta}_2. \tag{2.6b}$$

$$\frac{d}{dt}\left(\frac{d\mathscr{L}}{d\dot{\theta}_3}\right) = \left(m_3\lambda_{c3}^2 + I_{3L} + m_4\left(\lambda_{c4} - \lambda_3\right)^2 + I_{4L} + m_L\lambda_3^2\right)\ddot{\theta}_3$$

$$+\Big(m_3\lambda_{c3}^2 - m_3\lambda_{c3}\lambda_2 s_3 + I_{3L} + m_4\left(\lambda_3 - \lambda_{c4} - \lambda_2 s_3\right)\left(\lambda_3 - \lambda_{c4}\right)$$

$$+I_{4L} - m_L\left(\lambda_3^2 - \lambda_2\lambda_3 s_3\right)\Big)\ddot{\theta}_2$$

$$+\left(m_L\lambda_2\lambda_3 c_3 - m_3\lambda_{c3}\lambda_2 c_3 - m_4\lambda_2\left(\lambda_3 - \lambda_{c4}\right)c_3\right)\dot{\theta}_2\dot{\theta}_3. \tag{2.6c}$$

$$\frac{d\mathscr{L}}{d\theta_3} = \Big(m_3\lambda_{c3}^2 s_{23}c_{23} - m_3\lambda_2\lambda_{c3}c_2 c_{23} + I_{3L}s_{23}c_{23} - I_{3A}s_{23}c_{23}$$

$$+ m_4\left(\lambda_3 - \lambda_{c4}\right)^2 s_{23}c_{23} - m_4\left(\lambda_3 - \lambda_{c4}\right)\lambda_2 c_2 c_{23} + I_{4L}s_{23}c_{23}$$

$$-I_{4A}s_{23}c_{23} + m_L\lambda_3^2 s_{23}c_{23} - m_L\lambda_2\lambda_3 c_2 c_{23}\Big)\dot{\theta}_1^2$$

$$-\Big(m_3\lambda_2\lambda_{c3}c_3 + m_L\lambda_2\lambda_3 c_3\Big)\dot{\theta}_2^2 + \Big(I_{4A}s_{23}\Big)\dot{\theta}_1\dot{\theta}_4$$

$$-\Big(m_3\lambda_{c3}\lambda_2 c_3 + m_4\lambda_2 c_3\left(\lambda_3 - \lambda_{c4}\right) - m_L\left(\lambda_2\lambda_3 c_3\right)\Big)\dot{\theta}_2\dot{\theta}_3$$

$$-m_3 g\lambda_{c3}s_{23} - m_4 g\left(\lambda_3 - \lambda_{c4}\right)s_{23} - m_L g\lambda_3 s_{23}. \tag{2.6d}$$

Plugging in Equations 2.6b, 2.6c, and 2.6d, into 2.6a, one obtains Equation 2.7,

$$\tau_3 = \Big(m_3\lambda_{c3}^2 - m_3\lambda_{c3}\lambda_2 s_3 + I_{3L} + m_4\left(\lambda_3 - \lambda_{c4} - \lambda_2 s_3\right)\left(\lambda_3 - \lambda_{c4}\right)$$

$$+I_{4L} - m_L\left(\lambda_3^2 - \lambda_2\lambda_3 s_3\right)\Big)\ddot{\theta}_2$$

$$+\Big(m_3\lambda_{c3}^2 + I_{3L} + m_4\left(\lambda_{c4} - \lambda_3\right)^2 + I_{4L} + m_L\lambda_3^2\Big)\ddot{\theta}_3$$

$$-\Big(m_3\lambda_{c3}^2 s_{23}c_{23} - m_3\lambda_2\lambda_{c3}c_2 c_{23} + I_{3L}s_{23}c_{23} - I_{3A}s_{23}c_{23}$$

$$+m_4\left(\lambda_3 - \lambda_{c4}\right)^2 s_{23}c_{23} - m_4\left(\lambda_3 - \lambda_{c4}\right)\lambda_2 c_2 c_{23} + I_{4L}s_{23}c_{23}$$

$$-I_{4A}s_{23}c_{23} + m_L\lambda_3^2 s_{23}c_{23} - m_L\lambda_2\lambda_3 c_2 c_{23}\Big)\dot{\theta}_1^2$$

$$+\Big(m_3\lambda_2\lambda_{c3}c_3 + m_L\lambda_2\lambda_3 c_3\Big)\dot{\theta}_2^2 - \Big(I_{4A}s_{23}\Big)\dot{\theta}_1\dot{\theta}_4$$

$$+g\Big(m_3\lambda_{c3}s_{23} + m_4\left(\lambda_3 - \lambda_{c4}\right)s_{23} + m_L\lambda_3 s_{23}\Big). \tag{2.7}$$

These joint torques are mainly used in the simulation model of the Quanser QArm. However, these equations are also used to build a matrix of chosen parameters that are estimated in the loop. This process is explained in Section 3.1.

2.2 Torque to PWM conversion

The Quanser QArm can be manipulated through two distinct control strategies. The first strategy involves issuing commands in either joint or task space, upon which the internal Proportional Integral Derivative (PID) controller endeavors to achieve the specified command. The second strategy involves the transmission of a Pulse Width Modulation (PWM) signal that corresponds to the voltage output for each individual motor, thereby offering direct control over each joint. Thus, the second strategy is used for the experimental validation of this thesis.

PWM is a technique used to control analog devices using a digital signal. It works by pulsating DC current and varying the amount of time that each pulse stays 'on' to control the amount of current that flows to a device. This method can generate an analog-like signal from a digital device, such as the XM540 DC-Motor used in each of the joints of the QArm [3].

In the context of this research, the PWM control mode is utilized for commanding each joint of the Quanser QArm individually; however, it is important to note that, in our theory, the output of the adaptive controller is expressed in terms of torque rather than voltage. Consequently, an effective implementation of the proposed controllers necessitates the derivation of a conversion factor from torque to PWM voltage.

To this end, the DC motor voltage can be defined as follows:

$$V = Ri + L\frac{di}{dt} - K_e\omega, \tag{2.8}$$

where i is the current, R is the resistance, L is the inductance, $\frac{di}{dt}$ is the rate of change of current, K_e is the back electromotive force (EMF) constant, and ω is the angular velocity. The change in current and the back EMF constant term multiplied by the shaft speed can be assumed to be negligible when compared to the magnitude of Ri. The torque output of the motor can also be expressed in terms of the current in the following form:

$$\tau = K_t i, \tag{2.9}$$

where K_t is the motor torque constant.

Then, Equation (2.9) can be solved for the current and plugged into (2.8) to get the following expression:

$$V = \left(\frac{\tau}{K_t}\right)R. \qquad (2.10)$$

From the motor data sheet [3], one can calculate

$$K_t = \frac{10.6Nm}{4.4A}, \qquad (2.11)$$

$$R = \frac{12}{4.4}Ohms. \qquad (2.12)$$

The linear expression was derived for the adaptive controller allows the commanded torque to be translated into a PWM voltage input that the QArm can comprehend. However, the motor datasheet reveals a nonlinear relationship between torque and current, as illustrated in Figure 2.4.

In this research, for a more rigorous transformation, the data derived from the graph are meticulously extracted to construct a second-order polynomial function. This function more accurately delineates the relationship within the confines specified by the graph. Subsequently, a mapping is developed based on empirical motor testing, which provides an alternative conversion from torque to current. For a detailed exposition of these three torque-to-current mappings, refer to Figure 2.5.

After extensive experimentation, it was observed that the combination of linear and polynomial mapping yielded the most accurate results for the implementation of the novel adaptive controllers. It is crucial to underscore that, while the PWM voltage input is conducive to experimentation, it also harbors potential hazards. This is primarily attributable to the fact that the PWM signal lacks inherent constraints on the input, thereby posing a risk of saturation. Such saturation can inflict damage not only on the motors but also on the entire QArm system. To mitigate this risk in this research, two limiters have been implemented within the Simulink environment. The first
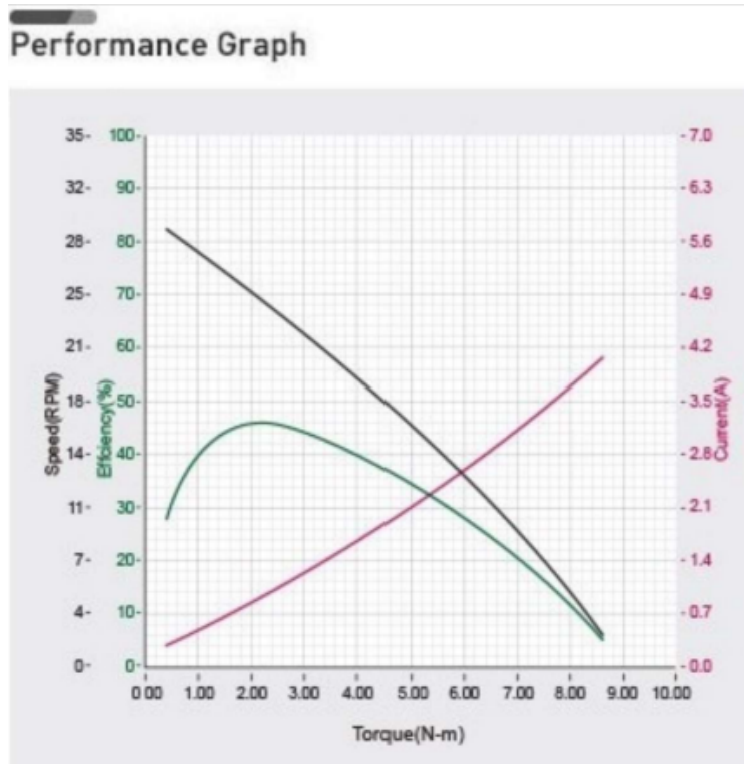
Figure 2.4 XM540 DC-Motor speed-efficiency-current to torque plot [3].

limiter imposes a cap on the PWM saturation, confining the input signal within the upper and lower saturation values. This safeguard ensures that, in the event of controller instability leading to an excessively large output value, this command will never reach the motors. The second limiter is imposed on the PWM rates, effectively constraining the rising and falling rates of the PWM signal.

Undeniably, these two constraints exert an influence on the system's response. Initial experimental results were obtained by testing the system with varying values for each limiter. After extensive experimentation, it was discerned that the optimal balance between system response and precautionary measures is achieved when the PWM saturation limits are set to ± 0.4 and the PWM rate limits are configured to ± 0.5.

In conclusion, the rigorous and meticulous approach is adopted in this study has yielded significant insights into the behavior of the system under varying conditions. The implementation of limiters within the Simulink environment has proven to be an effective strategy in mitigating

16
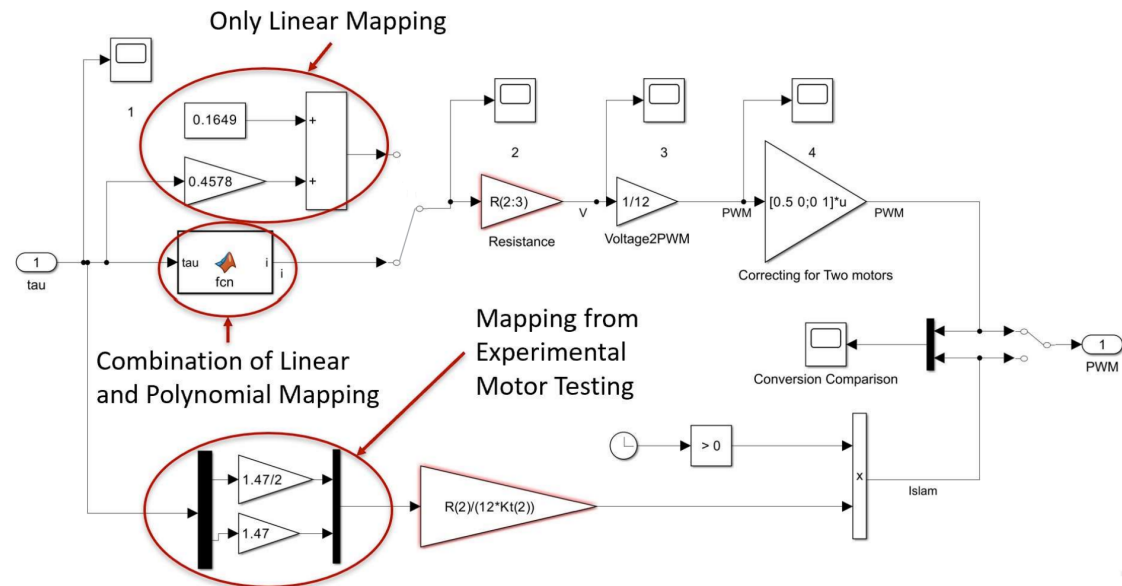
Figure 2.5 Torque to PWM mapping in the Simulink environment.

potential risks associated with the PWM voltage input. Furthermore, the extensive experimentation has led to the identification of optimal values for the PWM saturation and rate limits, striking a balance between system response and precautionary measures. These findings underscore the importance of careful parameter tuning in achieving desired system performance and stability. Future work may explore additional strategies for system optimization and risk mitigation.

17

3 Adaptive Control of Robotic Manipulators

In this section, we delineate two mathematical models pertinent to a robotic manipulator. The initial model is presented devoid of the control effectiveness matrix, thereby providing an insight into the conventional adaptive controller formulation as typically encountered in the literature. Subsequently, we exhibit a series of experimental results derived from this standard adaptive controller formulation, serving to further substantiate and motivate the research conducted in this thesis. Finally, we introduce the model formulation in the context of the unknown control effectiveness matrix, which incorporates the novel adaptive controller update laws as proposed in [5].

3.1 Problem Formulation in the Absence of the Unknown Control Effectiveness Matrix

The following generic dynamic model of an n degree of freedom (DoF) revolute joint, robot manipulator in the absence of the control effectiveness matrix is given as

$$M(q)\ddot{q} + V_m(q,\dot{q})\dot{q} + G(q) + F_d\dot{q} = \tau, \tag{3.1}$$

where $q(t)$, $\dot{q}(t)$, $\ddot{q}(t) \in \mathbb{R}^n$ denote the joint positions, velocities, and accelerations, respectively. $M(q) \in \mathbb{R}^{n \times n}$ is the positive definite and symmetric inertia matrix, $V_m(q,\dot{q}) \in \mathbb{R}^{n \times n}$, denotes the centripetal-Coriolis terms, $G(q) \in \mathbb{R}^n$ denotes the gravitational effects, and $F_d \in \mathbb{R}^{n \times n}$ denotes the constant viscous frictional effects.

In order to quantify the control objectives, one can define the joint level tracking error term, denoted by $e(t) \in \mathbb{R}^n$, and the estimation error term, denoted by $\tilde{\phi}(t) \in \mathbb{R}^p$, as follows:

$$
\begin{aligned}
e &\triangleq q_{\mathrm{d}} - q, \\
\tilde{\phi} &\triangleq \phi - \hat{\phi}
\end{aligned}
\tag{3.2}
$$

with $\hat{\phi}(t) \in \mathbb{R}^p$ being the estimation of an unknown dynamic model parameter vector $\phi \in \mathbb{R}^p$ (details below). In addition, an auxiliary signal, referred to as the filtered tracking error, denoted

by $r(t) \in \mathbb{R}^n$, is also defined in the following form:

$$r \triangleq \dot{e} + \mu e, \tag{3.3}$$

where $\mu \in \mathbb{R}_+^{n \times n} \cap \mathbb{D}_+^{n \times n}$ is a constant, positive definite, diagonal control gain matrix. For the adaptive controller development, the property that the robot dynamics given in (3.1) are linearly parametrizable [Lewis et al. [4]]is used, in the sense that

$$M(q)\ddot{q} + N(q,\dot{q}) = Y(q,\dot{q},\ddot{q})\phi. \tag{3.4}$$

Here, $Y(q,\dot{q},\ddot{q}) \in \mathbb{R}^{n \times p}$ is the regressor matrix, and $\phi \in \mathbb{R}^p$ is the unknown model parameter vector previously introduced in (3.2). Then, the desired form of the above expression, which is obtained by setting $q \rightarrow q_{\mathrm{d}}$, $\dot{q} \rightarrow \dot{q}_{\mathrm{d}}$, $\ddot{q} \rightarrow \ddot{q}_{\mathrm{d}}$, results in

$$Y_d(q_d,\dot{q}_d,\ddot{q}_d)\phi = M(q_d)\ddot{q}_d + \underbrace{V_m(q_d,\dot{q}_d)\dot{q}_d + G(q_d) + F_d\dot{q}_d}_{N(q_d,\dot{q}_d)}, \tag{3.5}$$

where $Y_{\mathrm{d}}(q_{\mathrm{d}},\dot{q}_{\mathrm{d}},\ddot{q}_{\mathrm{d}}) \in \mathbb{R}^{n \times p}$ is the desired version of the regression matrix $Y(q,\dot{q},\ddot{q})$, with $\dot{q}_{\mathrm{d}}$ and $\ddot{q}_{\mathrm{d}}$ being desired joint velocity and acceleration signals, respectively.

For this thesis, the unknown model parameter vector, $\phi \in \mathbb{R}^p$, is defined as:

$$\phi = \begin{bmatrix} m_2 & m_2 \\ I_{2L} & I_{2L} \\ m_3 & m_3 \\ I_{3L} & I_{3L} \\ m_4 & m_4 \\ I_{4L} & I_{4L} \end{bmatrix} , \tag{3.6}$$

$$\underbrace{\quad}_{\theta_2} \underbrace{\quad}_{\theta_3}$$

19

where mass and inertia parameters are selected.

Now the regression matrix $Y(q, \dot{q}, \ddot{q})$ can be built by refactoring Equations (2.5) and (2.7) in terms of our chosen model parameters. This gives

$$
Y = \begin{bmatrix}
\ddot{\theta}_2(\lambda_2 - \lambda_{c2})^2 - g(\lambda_2 - \lambda_{c2})\cos\theta_2 & 0 \\
\ddot{\theta}_2 & 0 \\
a & b \\
\ddot{\theta}_2 + \ddot{\theta}_3 & \ddot{\theta}_2 + \ddot{\theta}_3 \\
c & d \\
\ddot{\theta}_2 + \ddot{\theta}_3 & \ddot{\theta}_2 + \ddot{\theta}_3
\end{bmatrix}^T,
\tag{3.7}
$$

where $\theta \to q$, $\dot{\theta} \to \dot{q}$, $\ddot{\theta} \to \ddot{q}$ and

$$
a = \ddot{\theta}_2(\lambda_2^2 + \lambda_{c3}^2 - 2\lambda_2\lambda_{c3}\sin\theta_3) + \ddot{\theta}_3(\lambda_{c3}^2 - \lambda_{c3}\lambda_2\sin\theta_3)
$$
$$
- 2\dot{\theta}_2\dot{\theta}_3\lambda_2\lambda_{c3}\cos\theta_3 - \dot{\theta}_3{}^2\lambda_{c3}\lambda_2\cos\theta_3 - g(\lambda_2\cos\theta_1 - \lambda_{c3}\sin(\theta_1 + \theta_3)),
\tag{3.8}
$$

$$
b = \ddot{\theta}_2\lambda_{c3}^2 - \ddot{\theta}_2\lambda_2\lambda_{c3}\sin\theta_3 + \ddot{\theta}_3\lambda_{c3}^2 + \dot{\theta}_2{}^2\lambda_{c3}\lambda_2\cos\theta_3 + g\lambda_{c3}\sin(\theta_1 + \theta_3),
\tag{3.9}
$$

$$
c = \ddot{\theta}_2(\lambda_2 + \lambda_3 - \lambda_{c4})^2 + \ddot{\theta}_3(\lambda_3 - \lambda_{c4} - \lambda_2\sin\theta_3)(\lambda_3 - \lambda_{c4})
$$
$$
- \dot{\theta}_3{}^2\lambda_2\cos\theta_3(\lambda_3 - \lambda_{c4}) - g(\lambda_2\cos\theta_1 - (\lambda_3 - \lambda_{c4})\sin(\theta_1 + \theta_3)),
\tag{3.10}
$$

$$
d = \ddot{\theta}_2(-\lambda_2\sin\theta_3 + \lambda_3 - \lambda_{c4})(\lambda_3 - \lambda_{c4}) + \ddot{\theta}_3(-\lambda_3 + \lambda_{c4})^2 + g(\lambda_3 - \lambda_{c4})\sin(\theta_1 + \theta_3).
\tag{3.11}
$$

The dynamics of the tracking error are obtained straightforwardly from (3.3) as "$\dot{e} = r - \mu e$"; however, for obtaining the dynamics of the filtered tracking error, one can first take the time derivative of (3.3), then pre-multiply the resulting expression with the inertia matrix to obtain

$$
M\dot{r} = -V_m r + M(\ddot{q}_d + \mu\dot{e}) + V_m(\dot{q}_d + \mu e) + G + F_d\dot{q} - \tau,
\tag{3.12}
$$

where time derivatives of (3.2) and (3.3) are applied. In an attempt to present the open-loop error system in an advantageous way, the desired dynamics introduced in (3.5) are added and subtracted

to the right hand side of (3.12) to yield,

$$M\dot{r} = -V_m r + \mathscr{X} + Y_d \phi - \tau. \tag{3.13}$$

Here, $\mathscr{X}(t) \in \mathbb{R}^n$ is an auxiliary term defined as follows:

$$\mathscr{X} \triangleq M(\ddot{q}_d + \mu\dot{e}) + V_m(\dot{q}_d + \mu e) + G + F_d\dot{q} - Y_d\phi. \tag{3.14}$$

Note that, using properties of robot dynamics, an upper bound for $\mathscr{X}$ can be obtained as follows [4]:

$$\|\mathscr{X}\| \leq \rho_1\|e\| + \rho_2\|r\| \leq \rho\|z\|, \tag{3.15}$$

where $z(t) = [e^{\mathrm{T}}(t), r^{\mathrm{T}}(t)]^{\mathrm{T}} \in \mathbb{R}^{2n}$ denotes the combined error vector, and $\rho(\|e\|)$, $\rho_1(\|e\|)$, $\rho_2(\|e\|) \in \mathbb{R}_+$ are positive bounding functions that are defined as:

$$\begin{aligned}
\rho_1 &= \zeta_1 + \zeta_2\|e\|, \quad \rho_2 = \zeta_3 + \zeta_4\|e\|, \\
\rho &= \max\{\zeta_1, \zeta_3\} + \max\{\zeta_2, \zeta_4\}\|e\|
\end{aligned} \tag{3.16}$$

with ζ_1, ζ_2, ζ_3, $\zeta_4 \in \mathbb{R}_+$ being known constant positive bounds that depend on the desired joint trajectory and physical properties of the robot manipulator. It is emphasized that the upper bound of Equation (3.15) is standard in relevant literature; see, for example, [40–42].

Observing Equation (3.1), it is evident that the control input, or joint torque, is isolated on the right-hand side. This isolation implies an assumption that any control input commanded by a controller is flawlessly received and executed by the robotic manipulator. However, this assumption does not account for potential sources of uncertainty. These uncertainties could stem from a variety of factors such as a deficient motor that only delivers a fraction of the commanded voltage, or unmodeled physical disturbances like an external object impeding the manipulator's motion. These uncertainties are currently addressed indirectly through various control structures, as summarized in Section 1.2.1.

Nevertheless, there is potential for improvement in this approach. If these actuator deficiencies could be accurately estimated, and this estimated information is incorporated into the adaptive controller, it would result in a more precise tracking response of the joint torques. This approach would allow for a more robust and effective control of the robotic manipulator, even in the presence of substantial actuator deficiencies. The following sections delve into this proposition in greater detail, exploring its potential benefits.

3.1.1 Standard Adaptive Controller (SAC) Experimentation

To further motivate the need for the estimation of the unknown parts of the control effectiveness matrix, an experiment is performed on the Quanser QArm, with a forced actuator deficiency. This experiment is motivated by the structure of the open-loop error dynamics of Equation (3.13) which will be fully derived in Section 3.2. For the motivational experimental results, the following standard adaptive controller input signal is used

$$\tau = Y_d\hat{\phi} + K_r r + k_n \rho^2 r + e \tag{3.17}$$

with $K_r \in \mathbb{R}_+^{n \times n} \cap \mathbb{D}_+^{n \times n}$ and $k_n \in \mathbb{R}_+$ being the control gain matrix and damping gain, respectively. In (3.17), $\hat{\phi}(t) \in \mathbb{R}^p$, the estimation of the unknown dynamic model parameter vector, is updated via the below dynamic law

$$\dot{\hat{\phi}} = \Gamma Y_d^T r \tag{3.18}$$

with $\Gamma \in \mathbb{R}_+^{p \times p} \cap \mathbb{D}_+^{p \times p}$ being the constant, diagonal learning rate matrix.

An actuator deficiency of 80% is enforced by multiplying the commanded τ from the adaptive controller by $0.2I_2$. For comparison, a low actuator deficiency of 20% is also used. For both cases, the adaptation learning rates are set to $\Gamma = 1I_6$. The control gains are set to be $K_r = diag(40, 60)$, $k_n = 1$, and $\mu = 3$. The desired trajectory is the shoulder joint oscillating 10 degrees and the elbow joint oscillating 15 degrees with a period of about 6.25 seconds.

At low actuator deficiencies (i.e., 20% in this case), the large control gains appear to be enough to produce the desired tracking. In Figure 3.1, the desired joint angles are tracking quite well,
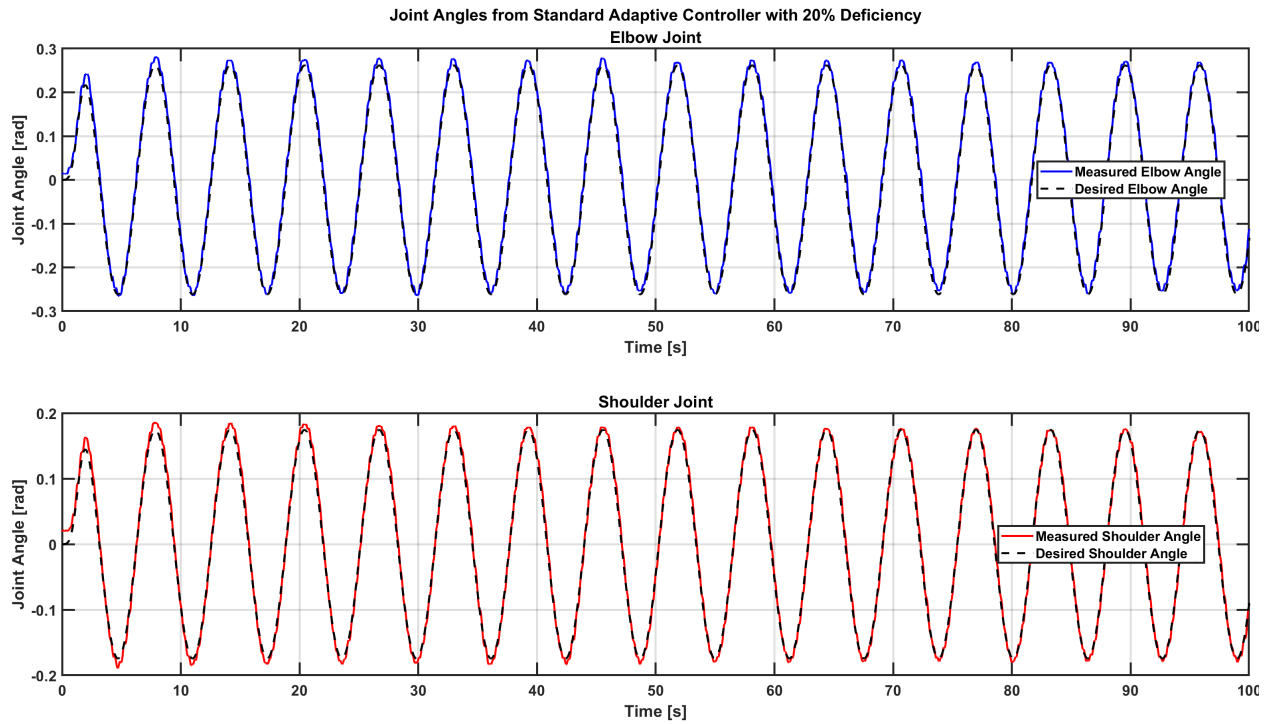
Figure 3.1 Joint angles via a SAC with actuator deficiency (20%).

which leads to the conclusion that a standard adaptive controller is sufficient to compensate for low actuator deficiencies.

At high actuator deficiencies (i.e., 80% in this case), the standard adaptive controller requires modification. In Figure 3.2, the tracking performance of both the shoulder and elbow joints in the robotic arm manipulator is not at a desired level of accuracy. This is evident from the fact that despite the system's inherent stability, the error reduction process is slow and gradual.

In Figure 3.2, the black dashed lines, which represent the desired and measured elbow angles respectively, one can observe a significant initial error at both the peak and trough of the sinusoidal pattern. This error is particularly pronounced at the start of the experiment. However, as the experiment progresses, on the elbow joint only, there is a noticeable improvement in tracking at the peak of the sinusoid. Unfortunately, this improvement is not mirrored at the trough, where a discrepancy of 0.05 rad or 2.86 degrees persists.

The shoulder joint exhibits a similar pattern. It starts with a substantial error that gradually diminishes as it approaches the desired joint angle. This slow but steady reduction is attributed to
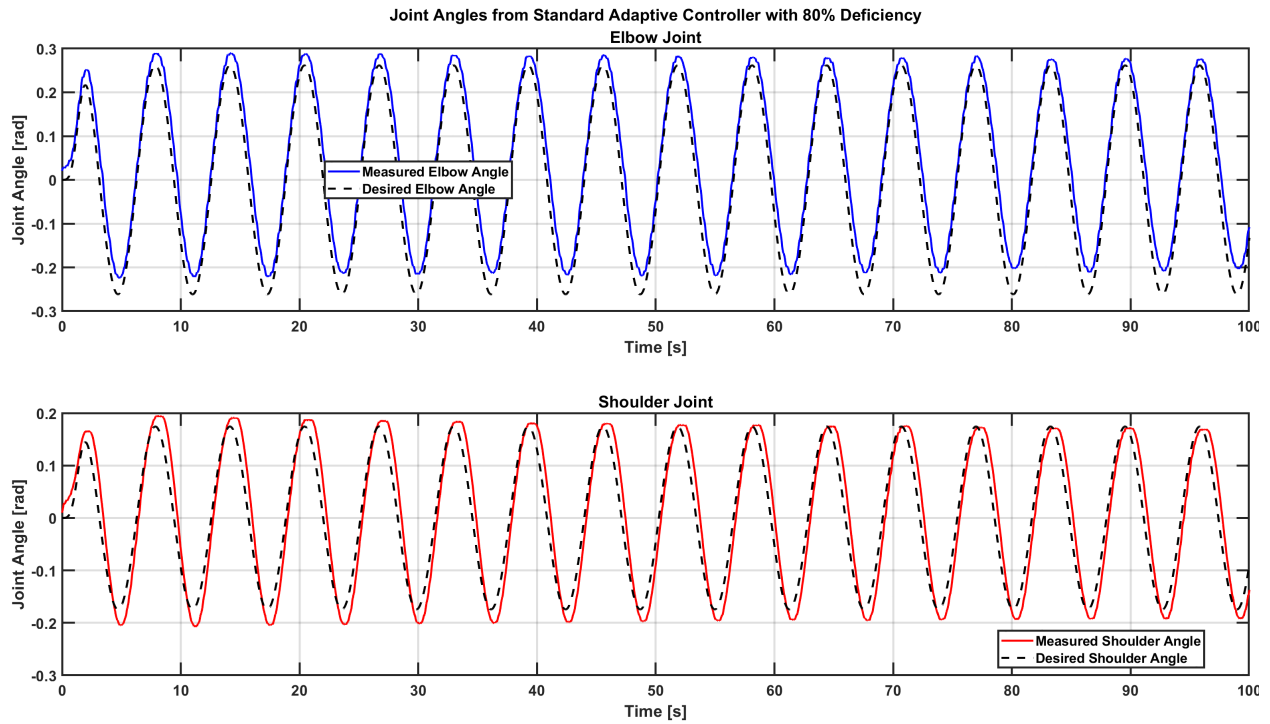
23

Figure 3.2 Joint angles via SAC with actuator deficiency (80%).

the adaptive control system's ability to learn and adjust its parameters over time; however, the error convergence could be much improved if the controller had an estimate of the actuator deficiency. In addition, Figures 3.3, 3.4, and 3.5 respectively show joint angular velocities, angle tracking errors, and control torques.

Upon initial observation, Figure 3.4 appears to indicate an escalating error for the elbow joint over the course of the experiment, while the error for the shoulder joint remains relatively constant. However, a more detailed analysis reveals additional nuances. The error term for both the peak and trough of the oscillation begins below zero. As the experiment progresses, the error at the trough of the oscillation remains nearly constant. In contrast, the error at the peak of the oscillation shows a trend toward zero, indicating an improvement in tracking performance over time.

The shoulder joint exhibits a more subtle change. While there is no significant shift in the overall error, a closer examination reveals a slight trend towards zero during the transition between the peak and trough of the oscillation towards the end of the experiment. This suggests that, while the error may not decrease significantly, the system is spending more time near the desired position.
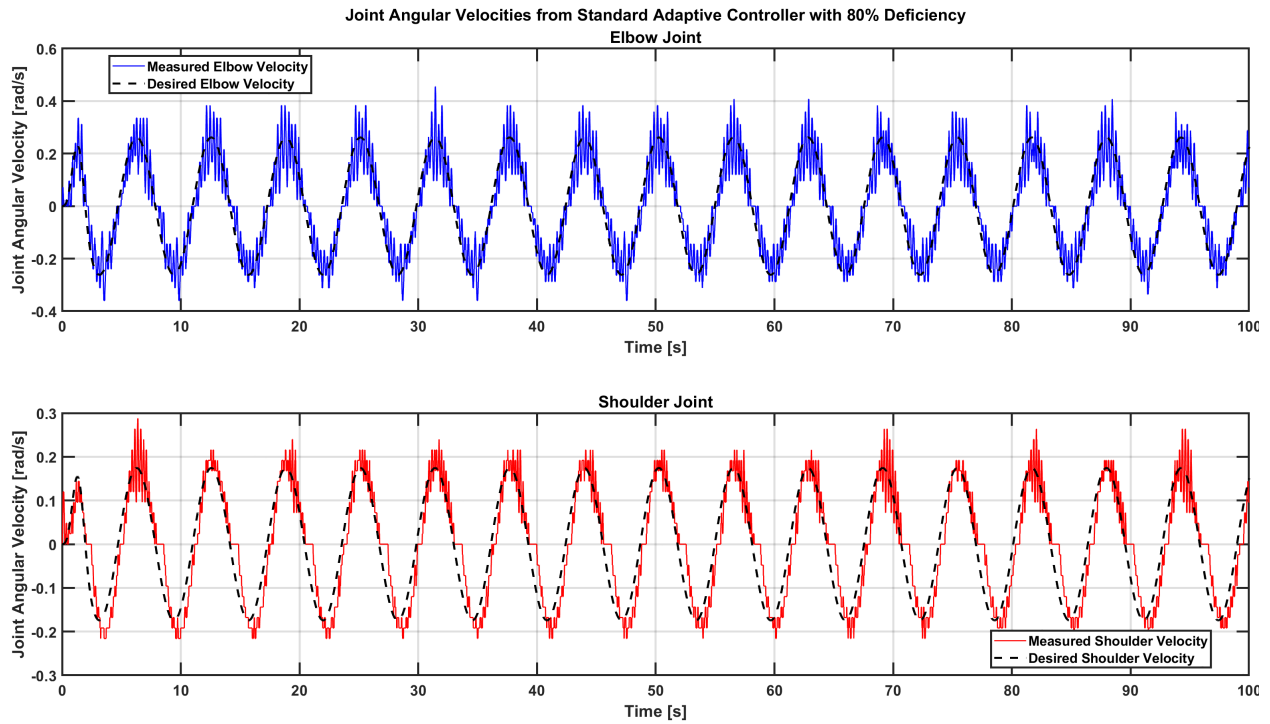
24

Figure 3.3 Angular velocities via SAC with actuator deficiency (80%).
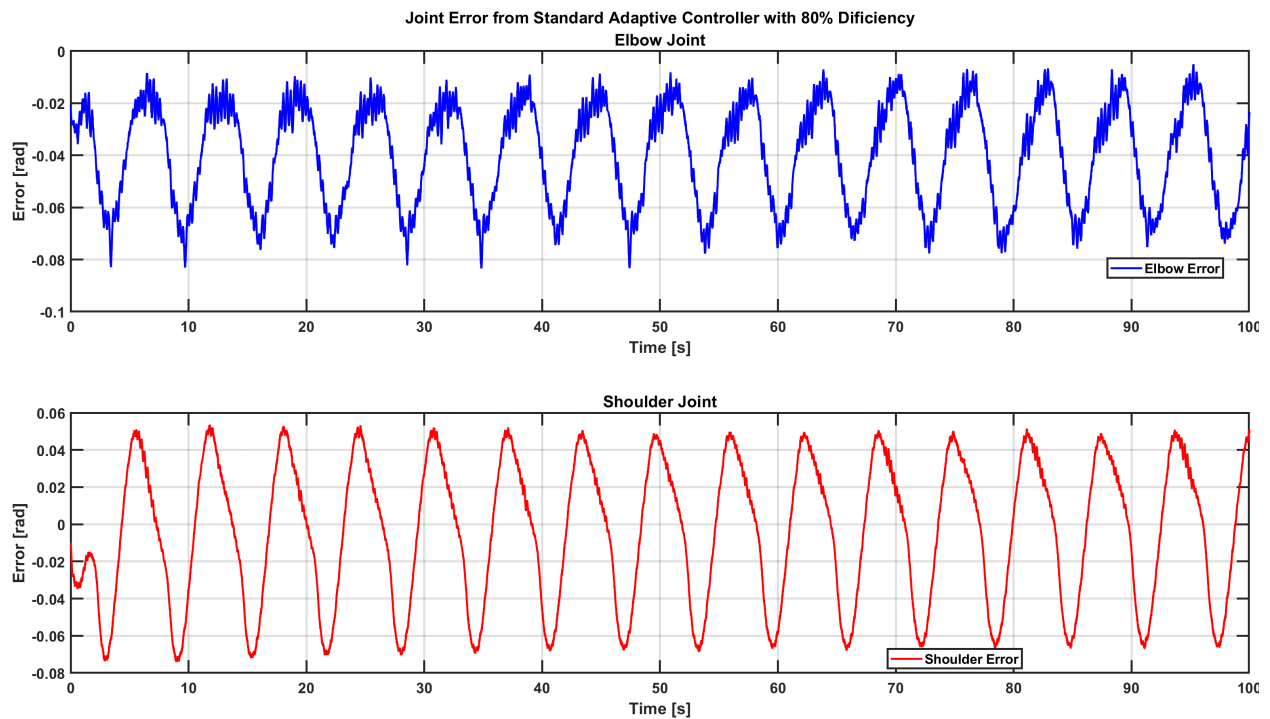

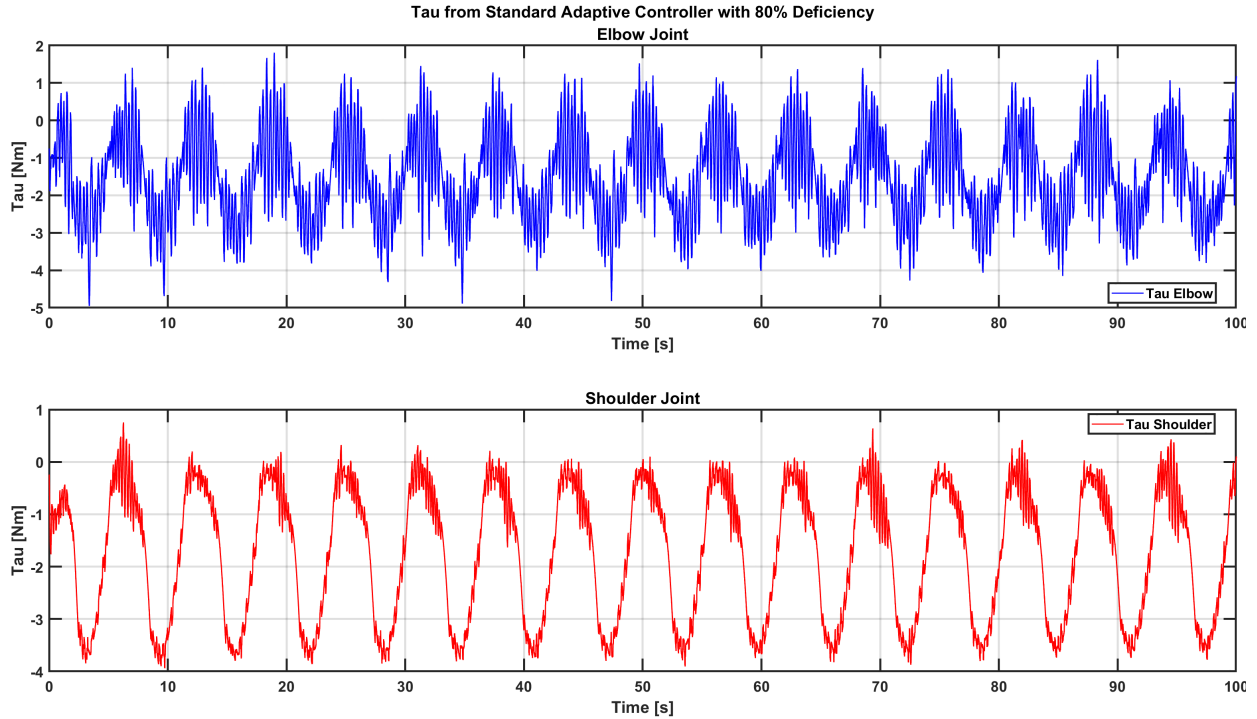*Figure 3.4* Joint error via SAC with actuator deficiency (80%).

Figure 3.5 Toques via SAC with actuator deficiency (80%).

These observations provide valuable insights into the performance of the standard adaptive control system in validating robotic arm manipulator movements. The results clearly highlight the need for improvement.

3.2 Problem Formulation in the Presents of the Unknown Control Effectiveness Matrix

This thesis, which is dependent on theoretical work presented in [5], includes the addition of an experimental comparison study with various cases such as 20%, 40%, 60%, and 80% actuator deficiencies. This section summarizes the theoretical results in [5] and how they differ from the standard mathematical model. In addition, a comprehensive context for a thorough understanding and appreciation of the experimental results presented in this thesis are given. The problem formulation includes the utilization of a control effectiveness matrix Λ that premultiplies the control input τ in order to model actuator deficiency. This allows two novel adaptive controllers to be designed that differ in how the estimated uncertainty terms are updated in the loop.

The updated dynamic model of an *n* DoF, revolute joint, robot manipulator is now given in

26

the following form in the presence of not only uncertain dynamics but also an unknown control effectiveness matrix:

$$M(q)\ddot{q} + N(q,\dot{q}) = \Lambda\tau, \tag{3.19}$$

where, again, $q(t)$, $\dot{q}(t)$, $\ddot{q}(t) \in \mathbb{R}^n$ denote the joint positions, velocities, and accelerations, respectively. $M(q) \in \mathbb{R}^{n \times n}$ is the positive definite and symmetric inertia matrix, and $N(q,\dot{q})$ represents all the nonlinear terms:

$$N(q,\dot{q}) \triangleq V_m(q,\dot{q})\dot{q} + G(q) + F_d\dot{q} \tag{3.20}$$

with $V_m(q,\dot{q}) \in \mathbb{R}^{n \times n}$ denoting the Centripetal-Coriolis terms, $G(q) \in \mathbb{R}^n$ denoting the gravitational effects, and $F_d \in \mathbb{R}^{n \times n}$ denoting the constant viscous frictional effects. In (3.19), the control input vector is denoted by $\tau(t) \in \mathbb{R}^n$ and the control effectiveness matrix is denoted by $\Lambda \in \mathbb{R}^{n \times n}$. In accordance with the relevant adaptive control literature, in this work, $\Lambda \triangleq I_n + \delta_\Lambda$ where $\delta_\Lambda \in \mathbb{R}^{n \times n} \cap \mathbb{D}^{n \times n}$ denotes the unknown part of the control effectiveness matrix subject to the assumption $\delta_\Lambda > -I_n$ (Gruenwald et al. [34], Dogan et al. [36, 43]).

In order to further quantify the control objectives, we define a second estimation error term denoted by $\tilde{\delta}_\Lambda(t) \in \mathbb{R}^{n \times n}$ as follows:

$$\tilde{\delta}_\Lambda \triangleq \delta_\Lambda - \hat{\delta}_\Lambda, \tag{3.21}$$

where $\hat{\delta}_\Lambda(t) \in \mathbb{R}^{n \times n} \cap \mathbb{D}^{n \times n}$ is the estimate of the unknown part of the control effectiveness matrix δ_Λ.

Several equations are unchanged by the addition of the control effectiveness matrix and have already been defined in Section 3.1, but are repeated here for clarity. There exist the joint level

tracking error term $e(t) \in \mathbb{R}^n$ and the estimation error term $\tilde{\phi}(t) \in \mathbb{R}^p$ from Equation (3.2)

$$
\begin{aligned}
e &\triangleq q_{\mathrm{d}} - q, \\
\tilde{\phi} &\triangleq \phi - \hat{\phi}.
\end{aligned}
\tag{3.22}
$$

The filtered tracking error $r(t) \in \mathbb{R}^n$ from Equation (3.3)

$$
r \triangleq \dot{e} + \mu e.
\tag{3.23}
$$

The robot dynamics are given in (3.19) and the definition of the regressor matrix for this linearly parametrizable [4] system is given by Equation (3.4)

$$
M(q)\ddot{q} + N(q, \dot{q}) = Y(q, \dot{q}, \ddot{q})\phi.
\tag{3.24}
$$

The desired version of the regression matrix $Y(q, \dot{q}, \ddot{q})$, where $\dot{q}_{\mathrm{d}}$ and $\ddot{q}_{\mathrm{d}}$ are desired joint velocity and acceleration signals, respectively, is given by Equation (3.5):

$$
Y_d(q_d, \dot{q}_d, \ddot{q}_d)\phi = M(q_d)\ddot{q}_d + \underbrace{V_m(q_d, \dot{q}_d)\dot{q}_d + G(q_d) + F_d\dot{q}_d}_{N(q_d, \dot{q}_d)}.
\tag{3.25}
$$

The dynamics of the tracking error are obtained straightforwardly from Equation (3.23) as "$\dot{e} = r - \mu e$"; however for obtaining the dynamics of the filtered tracking error, one can take the time derivative of Equation (3.23), then pre-multiply the resulting expression with the inertia matrix to obtain

$$
M\dot{r} = -V_m r + M(\ddot{q}_{\mathrm{d}} + \mu \dot{e}) + V_m(\dot{q}_{\mathrm{d}} + \mu e) + G + F_d\dot{q} - \Lambda\tau,
\tag{3.26}
$$

where time derivatives of Equation (3.22) and Equation (3.23) are applied. In an attempt to present the open–loop error system in an advantageous way, the desired dynamics introduced in Equation

(3.25) are added and subtracted to the right hand side of Equation (3.26) to yield

$$M\dot{r} = -V_m r + \mathscr{X} + Y_d \phi - \Lambda \tau. \tag{3.27}$$

Here, $\mathscr{X}(t) \in \mathbb{R}^n$ is identical to the auxiliary term defined in Equation (3.14):

$$\mathscr{X} \triangleq M(\ddot{q}_d + \mu \dot{e}) + V_m(\dot{q}_d + \mu e) + G + F_d \dot{q} - Y_d \phi. \tag{3.28}$$

where the bounds $\mathscr{X}$ are from Equation (3.15):

$$\|\mathscr{X}\| \le \rho_1 \|e\| + \rho_2 \|r\| \le \rho \|z\|, \tag{3.29}$$

and the positive bounding functions are given in Equation (3.16):

$$
\begin{aligned}
\rho_1 &= \zeta_1 + \zeta_2 \|e\|, \quad \rho_2 = \zeta_3 + \zeta_4 \|e\|, \\
\rho &= \max\{\zeta_1, \zeta_3\} + \max\{\zeta_2, \zeta_4\} \|e\|
\end{aligned} \tag{3.30}
$$

where ζ_1, ζ_2, ζ_3, $\zeta_4 \in \mathbb{R}_+$ are known constant positive bounds that depend on the desired joint trajectory and physical properties of the robot manipulator.

At this stage, motivated by the structure of the open-loop error dynamics of Equation (3.27) and the subsequent stability analysis, the following adaptive controller is proposed:

$$\tau = (I + \hat{\delta}_\Lambda)^{-1}(Y_d \hat{\phi} + K_r r + k_n \rho^2 r + e), \tag{3.31}$$

where $K_r \in \mathbb{R}_+^{n \times n} \cap \mathbb{D}_+^{n \times n}$ and $k_n \in \mathbb{R}_+$ are a control gain matrix and damping gain, respectively. In Equation (3.31), $\hat{\phi}(t) \in \mathbb{R}^p$, the estimation of the unknown dynamic model parameter vector, is updated via the below dynamic law:

$$\dot{\hat{\phi}} = \Gamma Y_d^T r, \tag{3.32}$$

where $\Gamma \in \mathbb{R}_+^{p \times p} \cap \mathbb{D}_+^{p \times p}$ is a constant, diagonal learning rate matrix. Moreover, in Equation (3.31), $\hat{\delta}_\Lambda(t) \in \mathbb{R}^{n \times n} \cap \mathbb{D}^{n \times n}$ can be written as $\hat{\delta}_\Lambda(t) = \mathrm{diag}([\hat{\delta}_{\lambda_1}(t), \hat{\delta}_{\lambda_2}(t), ..., \hat{\delta}_{\lambda_n}(t)])$. In this work, two novel adaptive update rules are used from [5] to compensate for the uncertainties in the control effectiveness matrix. The main issue in designing update laws as estimations for the uncertainties of the control effectiveness matrix is the need to upper and lower bound the estimated values with known maximum and minimum bounds of $\delta_{\lambda_{\max_i}}$ and $\delta_{\lambda_{\min_i}}$, respectively, for each actuated joint $i = 1, ..., n$. To guarantee the inversion of $I + \hat{\delta}_\Lambda(t)$, we consider $-1 < \hat{\delta}_{\lambda i, min} \leq \hat{\delta}_{\lambda i}(t) \leq \hat{\delta}_{\lambda i, max}$.

In order to meet these strict design criteria, as the first design, the below-given novel adaptive update law is proposed:

$$\dot{\hat{\delta}}_{\lambda_i} = -\gamma_i(\hat{\delta}_{\lambda_i} - \delta_{\lambda_{\max_i}})(\hat{\delta}_{\lambda_i} - \delta_{\lambda_{\min_i}}) r_i \tau_i. \tag{3.33}$$

Here, for each actuated joint $i = 1, ..., n$, $\gamma_i \in \mathbb{R}_+$ is the learning rate with $r_i(t)$ and $\tau_i(t)$ denoting the ith entry of $r(t)$ and $\tau(t)$, respectively.

Secondly, inspired by the recent results in the literature [43], a projection operator-based design of the form

$$\dot{\hat{\delta}}_{\lambda_i} = -\gamma_i \mathrm{Proj}[\hat{\delta}_{\lambda_i}, \tau_i r^{\mathrm{T}} \mathbf{b}_i] \tag{3.34}$$

is proposed. Here, the projection operator from, for example, [44] or [Exercise 11.3, [45]] is utilized. Specifically, let $\Omega = \{\theta \in \mathbb{R}^n : (\theta_i^{\min} \leq \theta_i \leq \theta_i^{\max})_{i=1,...,n}\} \subset \mathbb{R}^n$ be a convex hypercube with $\theta_i^{\min}$ and $\theta_i^{\max}$, respectively, denoting the minimum and maximum bounds for the ith component of the parameter vector $\theta \in \mathbb{R}^n$. In addition, for a sufficiently small constant $\varepsilon_0 \in \mathbb{R}_+$, let $\Omega_{\varepsilon_0} = \{\theta \in \mathbb{R}^n : (\theta_i^{\min} + \varepsilon_0 \leq \theta_i \leq \theta_i^{\max} - \varepsilon_0)_{i=1,2,...,n}\}$ be another convex hypercube (i.e., $\Omega_{\varepsilon_0} \subset \Omega$).

Then, the component-wise projection operator $\mathrm{Proj} : \mathbb{R}^n \times \mathbb{R}^n \to \mathbb{R}^n$ is defined as $\mathrm{Proj}(\theta_i, y_i) = (\theta_i^{\max} - \theta_i)y_i/\varepsilon_0$ when $\theta_i > \theta_i^{\max} - \varepsilon_0$ and $y_i > 0$, $\mathrm{Proj}(\theta_i, y_i) = (\theta_i - \theta_i^{\min})y_i/\varepsilon_0$ when $\theta_i < \theta_i^{\min} + \varepsilon_0$ and $y_i < 0$, and $\mathrm{Proj}(\theta_i, y_i) = y_i$ otherwise, where $y \in \mathbb{R}^n$. Finally, the projection operator satisfies the below property (e.g., see [45]):

$$(\theta - \theta^*)^{\mathrm{T}}(\mathrm{Proj}(\theta, y) - y) \leq 0, \quad \theta^* \in \Omega_{\varepsilon_0}. \tag{3.35}$$

Substituting the adaptive control input design in Equation (3.31) into Equation (3.27) leads to

$$M\dot{r} = -V_m r + \mathscr{X} + Y_d\tilde{\phi} - K_r r - k_n \rho^2 r - e - \tilde{\delta}_\Lambda \tau, \tag{3.36}$$

where $\Lambda\tau = (I + \hat{\delta}_\Lambda(t) + \tilde{\delta}_\Lambda(t))\tau$ is utilized.

3.2.1 Stability Analysis

The first theorem is introduced for investigating the stability of the controlled system under the bound-based update law design of Equation (3.33).

Theorem 1 [5]

Consider the n DoF robot manipulator model given by Equation (3.19). Then, the adaptive control architecture given by Equation (3.31), Equation (3.32), and Equation (3.33) ensures asymptotic stability of the closed–loop system and tracking error such that $\|e(t)\| \to 0$ as $t \to +\infty$ provided that the control gains are chosen to meet the below condition:

$$\min(\lambda_{\min}(K_r), \lambda_{\min}(\mu)) > \frac{1}{4k_n}. \tag{3.37}$$

Proof. To investigate the stability of the equilibrium point of the trajectories of $\{r(t), e(t), \tilde{\phi}(t), \tilde{\delta}_\Lambda(t)\}$, the below novel Lyapunov–like function is introduced as:

$$\begin{aligned}
V_1(r, e, \tilde{\phi}, \tilde{\delta}_\Lambda) &\triangleq \frac{1}{2}r^\mathrm{T}Mr + \frac{1}{2}e^\mathrm{T}e + \frac{1}{2}\tilde{\phi}^\mathrm{T}\Gamma^{-1}\tilde{\phi} \\
&+ \sum_{i=1}^{n} \frac{\sigma_i}{\gamma_i}\ln\left(\frac{\delta_{\lambda_{\max_i}} - \hat{\delta}_{\lambda_i}}{\Delta_i}\right) - \frac{\sigma_i + 1}{\gamma_i}\ln\left(\frac{\hat{\delta}_{\lambda_i} - \delta_{\lambda_{\min_i}}}{\Delta_i}\right),
\end{aligned}$$

$$\tag{3.38}$$

where, for $i = 1, \ldots, n$, $\Delta_i \in \mathbb{R}$ and $\sigma_i \in \mathbb{R}$ are constants defined as:

$$\Delta_i \triangleq \delta_{\lambda_{\max_i}} - \delta_{\lambda_{\min_i}}, \quad \sigma_i \triangleq \frac{\delta_{\lambda_i} - \delta_{\lambda_{\max_i}}}{\Delta_i}. \tag{3.39}$$

After taking the time derivative of V_1 of Equation (3.38) and substituting with Equation (3.23),

Equation (3.32) and Equation (3.36), one can obtain:

$$\dot{V}_1(\cdot) = r^{\mathrm{T}} \underbrace{\left(-V_m(q,\dot{q})r + \mathcal{X} + Y_d\tilde{\phi} - K_r r - k_n \rho^2 r - e - \tilde{\delta}_\Lambda \tau\right)}_{M\dot{r}}$$

$$+\frac{1}{2}r^{\mathrm{T}}\dot{M}r + e^{\mathrm{T}}\underbrace{(r-\mu e)}_{\dot{e}} - \tilde{\phi}^{\mathrm{T}}\Gamma^{-1}\underbrace{\Gamma Y_d^{\mathrm{T}} r}_{\dot{\hat{\phi}}} + \sum_{i=1}^{n}\frac{\sigma_i}{\gamma_i}\frac{-\dot{\hat{\delta}}_{\lambda_i}}{\delta_{\lambda_{\max_i}} - \hat{\delta}_{\lambda_i}} - \frac{\sigma_i+1}{\gamma_i}\frac{\dot{\hat{\delta}}_{\lambda_i}}{\hat{\delta}_{\lambda_i} - \delta_{\lambda_{\min_i}}}. \quad (3.40)$$

After substituting Equation (3.39) for σ_i in Equation (3.40) and putting the last two terms into a common denominator, Equation (3.40) simplifies to:

$$\begin{aligned}\dot{V}_1(\cdot) &= r^{\mathrm{T}}\left(-V_m(q,\dot{q})r + \mathcal{X} + Y_d\tilde{\phi} - K_r r - k_n \rho^2 r - e - \tilde{\delta}_\Lambda \tau\right)\\ &+\frac{1}{2}r^{\mathrm{T}}\dot{M}r + e^{\mathrm{T}}(r-\mu e) - \tilde{\phi}^{\mathrm{T}}Y_d^{\mathrm{T}} r + \sum_{i=1}^{n}\frac{\tilde{\delta}_{\lambda_i}}{\gamma_i}\frac{1}{(\hat{\delta}_{\lambda_i} - \delta_{\lambda_{\max_i}})(\hat{\delta}_{\lambda_i} - \delta_{\lambda_{\min_i}})}\dot{\hat{\delta}}_{\lambda_i}.\end{aligned}$$

$$(3.41)$$

Then utilizing the *skew–symmetric* property of robot dynamics, that is $a^{\mathrm{T}}(\dot{M}(q) - 2V_m(q,\dot{q}))a = 0, \forall a \in \mathbb{R}^n$ with Equation (3.33), and performing cancellations, Equation (3.41) can be rewritten as follows:

$$\begin{aligned}\dot{V}_1(\cdot) &= r^{\mathrm{T}}\left(\mathcal{X} - K_r r - k_n \rho^2 r - \tilde{\delta}_\Lambda \tau\right) - e^{\mathrm{T}}\mu e\\ &+\sum_{i=1}^{n}\frac{\tilde{\delta}_{\lambda_i}}{\gamma_i}\frac{1}{(\hat{\delta}_{\lambda_i} - \delta_{\lambda_{\max_i}})(\hat{\delta}_{\lambda_i} - \delta_{\lambda_{\min_i}})} \times \underbrace{[-\gamma_i(\hat{\delta}_{\lambda_i} - \delta_{\lambda_{\max_i}})(\hat{\delta}_{\lambda_i} - \delta_{\lambda_{\min_i}})r_i\tau_i]}_{\dot{\hat{\delta}}_{\lambda_i}}\\ &= r^{\mathrm{T}}\mathcal{X} - r^{\mathrm{T}}K_r r - k_n \rho^2 \|r\|^2 - e^{\mathrm{T}}\mu e.\end{aligned} \quad (3.42)$$

Using the upper bound for the auxiliary variable given by Equation (3.29) in Equation (3.42) yields

$$\dot{V}_1(\cdot) \leq \rho\|z\|\|r\| - \lambda_{\min}(K_r)\|r\|^2 - k_n\rho^2\|r\|^2 - \lambda_{\min}(\mu)\|e\|^2. \quad (3.43)$$

After applying Young's inequality, $\rho\|r\|\|z\| \leq \varepsilon\rho^2\|r\|^2 + \frac{1}{4\varepsilon}\|z\|^2$ with $\varepsilon = k_n$, an upper bound for

Equation (3.43) can be written as:

$$\dot{V}_1(\cdot) \leq -\kappa \|z\|^2, \tag{3.44}$$

where $\kappa \triangleq \min(\lambda_{\min}(K_r), \lambda_{\min}(\mu)) - \frac{1}{4k_n} \in \mathbb{R}_+$ is a positive constant. Therefore, $\dot{V}_1 \leq 0$ and all signals are globally bounded if the control gains satisfies the condition in Equation (3.37). Standard signal-chasing algorithms for gain tuning can be used to ensure global boundedness of all the signals under closed-loop operation. Barbalat's Lemma can then be utilized to prove global asymptotic convergence of the tracking error to the origin [4].

Next, the stability of the closed–loop system under the projection operator-based design of Equation (3.33) is investigated via the following theorem.

Theorem 2 [5]

Under the adaptive control architecture given by Equation (3.31), Equation (3.32) and Equation (3.34), the n DoF robot manipulator dynamic model given by Equation (3.19) is proven to remain stable and asymptotic stability of the tracking error is ensured in the sense that $\|e(t)\| \to 0$ as $t \to +\infty$ provided that the control gains are chosen to meet the inequality condition of Equation (3.37).

Proof. The following Lyapunov–like function is utilized when investigating the stability of the closed–loop system dynamics:

$$V_2(r, e, \tilde{\phi}, \tilde{\delta}_\Lambda) \triangleq \frac{1}{2} r^{\mathrm{T}} M r + \frac{1}{2} e^{\mathrm{T}} e + \frac{1}{2} \tilde{\phi}^{\mathrm{T}} \Gamma^{-1} \tilde{\phi} + \sum_{i=1}^{n} \frac{1}{\gamma_i} \tilde{\delta}_{\lambda_i}^2. \tag{3.45}$$

Taking the time derivative of V_2 of Equation (3.45) and substituting for Equation (3.23), Equation (3.32), Equation (3.34) and Equation (3.36) results in:

$$
\begin{aligned}
\dot{V}_2(\cdot) \;=\;& r^{\mathrm{T}} \underbrace{\left(-V_m(q,\dot{q})r + \mathscr{X} + Y_{\mathrm{d}}\tilde{\phi} - K_{\mathrm{r}}r - k_{\mathrm{n}}\rho^2 r - e - \tilde{\delta}_\Lambda \tau\right)}_{M\dot{r}} \\
&+ \frac{1}{2}r^{\mathrm{T}}\dot{M}r + e^{\mathrm{T}}\underbrace{(r - \mu e)}_{\dot{e}} - \tilde{\phi}^{\mathrm{T}}\Gamma^{-1}\underbrace{\Gamma Y_{\mathrm{d}}^{\mathrm{T}}r}_{\dot{\hat{\phi}}} + \gamma_i^{-1}\sum_{i=1}^{n}\tilde{\delta}_{\lambda_i}\underbrace{\gamma_i \mathrm{Proj}[\hat{\delta}_{\lambda_i},\,\tau_i r^{\mathrm{T}}\mathbf{b}_i]}_{-\dot{\hat{\delta}}_{\lambda_i}} \\
=\;& \frac{1}{2}r^{\mathrm{T}}\dot{M}r + r^{\mathrm{T}}\left(-V_m(q,\dot{q})r + \mathscr{X} + Y_{\mathrm{d}}\tilde{\phi} - K_{\mathrm{r}}r - k_{\mathrm{n}}\rho^2 r - e - \underbrace{\sum_{i=1}^{n}\mathbf{b}_i\tilde{\delta}_{\lambda_i}\tau_i}_{\tilde{\delta}_\Lambda \tau}\right) + e^{\mathrm{T}}(r - \mu e) \\
&- \tilde{\phi}^{\mathrm{T}}\Gamma^{-1}\Gamma Y_{\mathrm{d}}^{\mathrm{T}}r + \gamma_i^{-1}\sum_{i=1}^{n}\tilde{\delta}_{\lambda_i}\gamma_i \mathrm{Proj}[\hat{\delta}_{\lambda_i},\,\tau_i r^{\mathrm{T}}\mathbf{b}_i].
\end{aligned}
\tag{3.46}
$$

Then, utilizing the skew–symmetric property of the robot dynamics, the property of the projection operator given by Equation (3.35), and cancelling out common terms, the right hand side of Equation (3.46) can be further simplified as:

$$
\dot{V}_2(\cdot) \le r^{\mathrm{T}}\mathscr{X} - r^{\mathrm{T}}K_{\mathrm{r}}r - k_{\mathrm{n}}\rho^2\|r\|^2 - e^{\mathrm{T}}\mu e.
\tag{3.47}
$$

After making use of the upper bound of the auxiliary variable given by Equation (3.29), the right hand side of Equation (3.47) is further upper bounded as:

$$
\dot{V}_2(\cdot) \;\le\; \rho\|z\|\|r\| - \lambda_{\min}(K_{\mathrm{r}})\|r\|^2 - k_{\mathrm{n}}\rho^2\|r\|^2 - \lambda_{\min}(\mu)\|e\|^2.
\tag{3.48}
$$

Following similar steps as in the proof of Theorem 1, both global boundedness of all the signals of the closed–loop system under the proposed adaptive control architecture and global asymptotic convergence of the tracking error to the origin can be proven.

4 Simulation Results

To illustrate the performance of the proposed adaptive control architecture with the two controller designs given by Equations (3.31), (3.32), (3.33) and Equations (3.31), (3.32), (3.34), numerical simulations with a model of a two–link planar robot manipulator are conducted. Specifically, the dynamic model in Equation (3.19) is considered with the following modeling functions [46]:

$$M = \begin{bmatrix} p_1 + 2p_3 c_{q_2} & p_2 + p_3 c_{q_2} \\ p_2 + p_3 c_{q_2} & p_2 \end{bmatrix}$$

$$V_m = \begin{bmatrix} -p_3 s_{q_2} \dot{q}_2 & -p_3 s_{q_2} (\dot{q}_1 + \dot{q}_2) \\ p_3 s_{q_2} \dot{q}_1 & 0 \end{bmatrix}, F_d = \begin{bmatrix} f_{d_1} & 0 \\ 0 & f_{d_2} \end{bmatrix},$$

in which $s_{q_2} = \sin(q_2)$, $c_{q_2} = \cos(q_2)$, $p_1 = 3.473[\text{kg-m}^2]$, $p_2 = 0.193[\text{kg-m}^2]$, $p_3 = 0.242[\text{kg-m}^2]$, $f_{d_1} = 5.3[\text{Nm-sec}]$, and $f_{d_2} = 1.1[\text{Nm-sec}]$. The robot manipulator is considered to be initially at rest at the joint configuration of $q(0) = [0.5, 0.5]^T$ rad. The desired joint trajectory is selected as:

$$q_d = \begin{bmatrix} 0.7 \sin(t)(1 - \exp(-0.3t^3)) \\ 1.2 \sin(t)(1 - \exp(-0.3t^3)) \end{bmatrix}. \tag{4.1}$$

The control gains are set as $K_r = [0.55, 0; 0, 0.6]$, $\mu = 1.5I_2$, $\rho = 0.35$ and $k_n = 0.5$, while the adaptation gains are set as $\Gamma = 0.55I_5$ and $\gamma = 25I_2$. Actuator deficiency is selected as $\delta_{\lambda_i} = -0.75$ for both joints while the upper and lower bounds are selected as $\delta_{\lambda_{\max_i}} = -0.5$ and $\delta_{\lambda_{\min_i}} = -0.77$, and the projection bounds are selected as $\delta_{\lambda_{\max_i}} = -0.5$ and $\delta_{\lambda_{\min_i}} = -0.77$. These choices were made to satisfy the condition in Equation (3.37) and to provide a response that indicated the problems with the standard adaptive controller.

The results of the numerical simulations are presented in Figures 4.1–4.6. Specifically, Figures 4.1 and 4.2 show the tracking and controller performance of the adaptive controller without any compensation for the uncertainties in the control effectiveness matrix, where the standard adaptive control (SAC) architecture $\tau = Y_d \hat{\phi} + K_r r + k_n \rho^2 r + e$ from Equation (3.17) is applied. Actual and

35

desired joint positions for the bound-based adaptive control (BAC) architecture and projection-based adaptive control (PAC) architecture are shown in Figures 4.3, 4.4 and 4.5, 4.6, respectively. Finally, the square of the integral of the norm of the tracking errors and control input torques are in Table 4.1. With the utilized parameters given in this section, one can see that the projection operator-based design for the actuator effectiveness yields a better response with less tracking error when compared with the bound-based design, where both of them outperformed the standard adaptive controller in terms of tracking accuracy and control effort.

Table 4.1 Performance measurements comparing the adaptive controllers (75% deficiency).

	Standard	Bound–based	Projection–based
$\int_0^{t_{\text{final}}} \lvert e_1(t) \rvert^2 dt$	0.7807	0.4767	0.2136
$\int_0^{t_{\text{final}}} \lvert e_2(t) \rvert^2 dt$	0.2342	0.1292	0.0536
$\int_0^{t_{\text{final}}} \lvert \tau_1(t) \rvert^2 dt$	24.3091	17.997	14.2198
$\int_0^{t_{\text{final}}} \lvert \tau_2(t) \rvert^2 dt$	4.5343	4.1474	3.9878
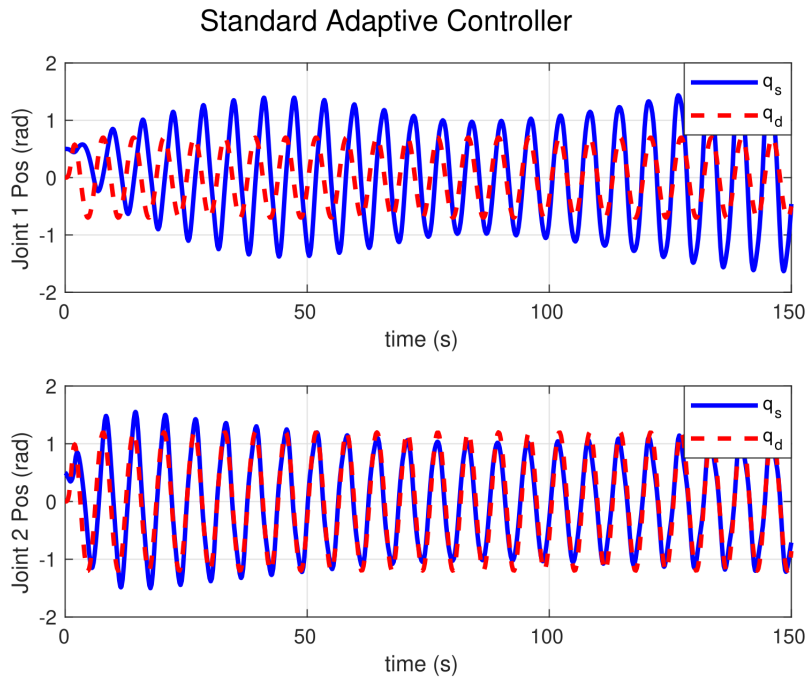
Figure 4.1 Joint angle via SAC for 75% actuator deficiency.
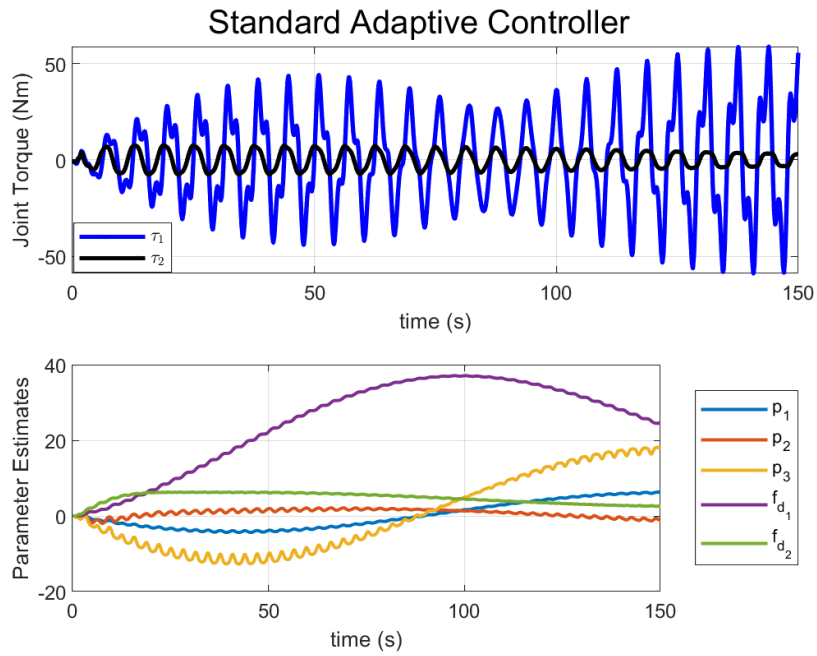
Figure 4.2 Torque and estimated parameters via SAC for 75% actuator deficiency.
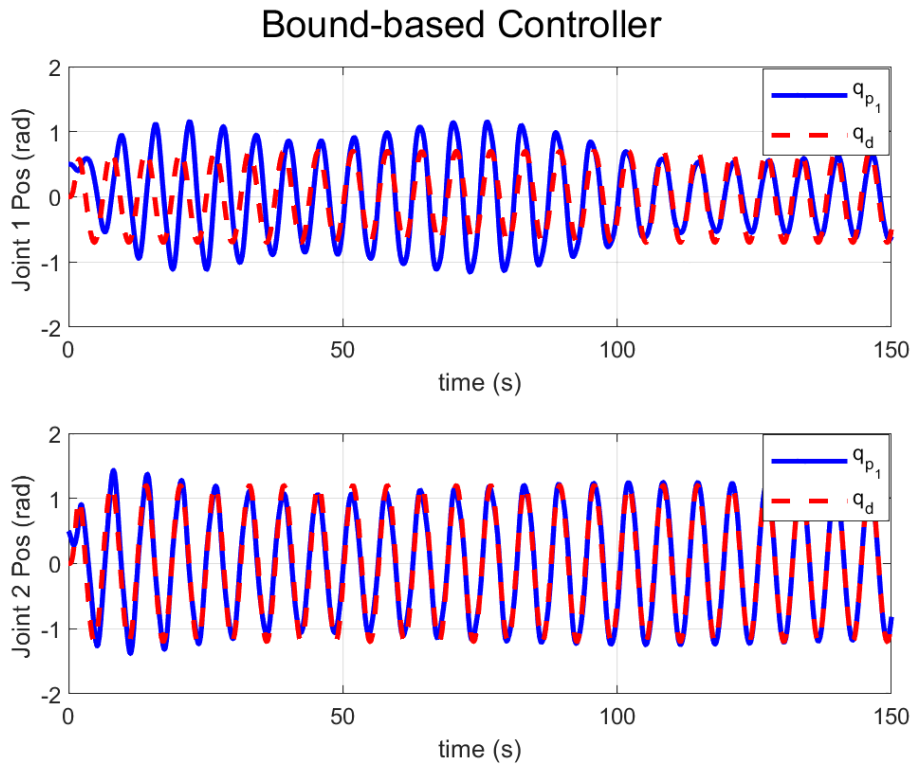
Figure 4.3 Tracking via BAC for 75% actuator deficiency.
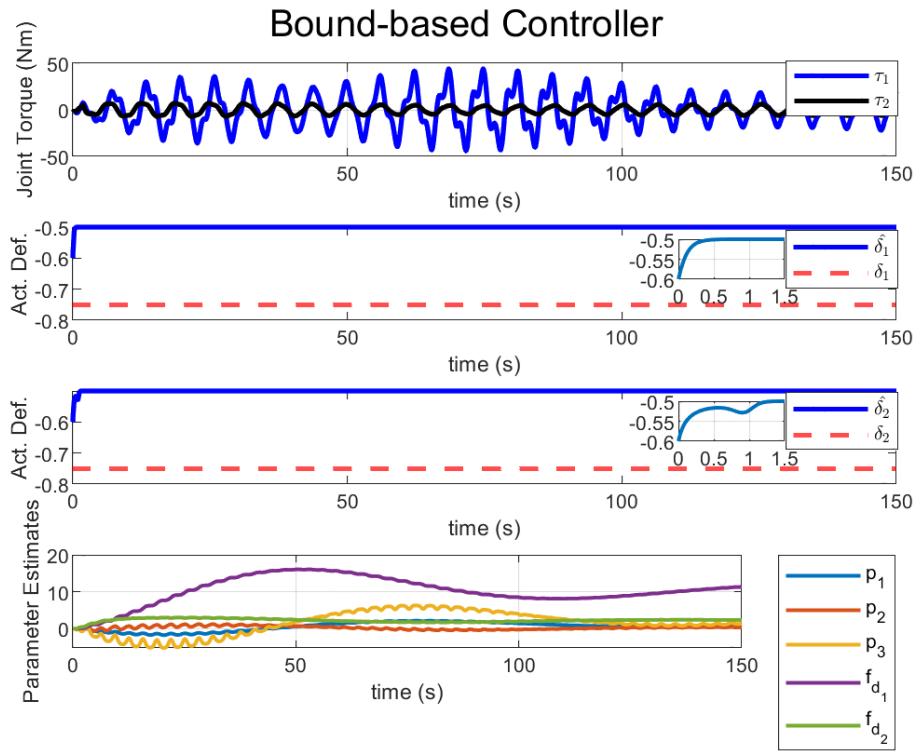
Figure 4.4 Torque and estimated parameters via BAC for 75% actuator deficiency.
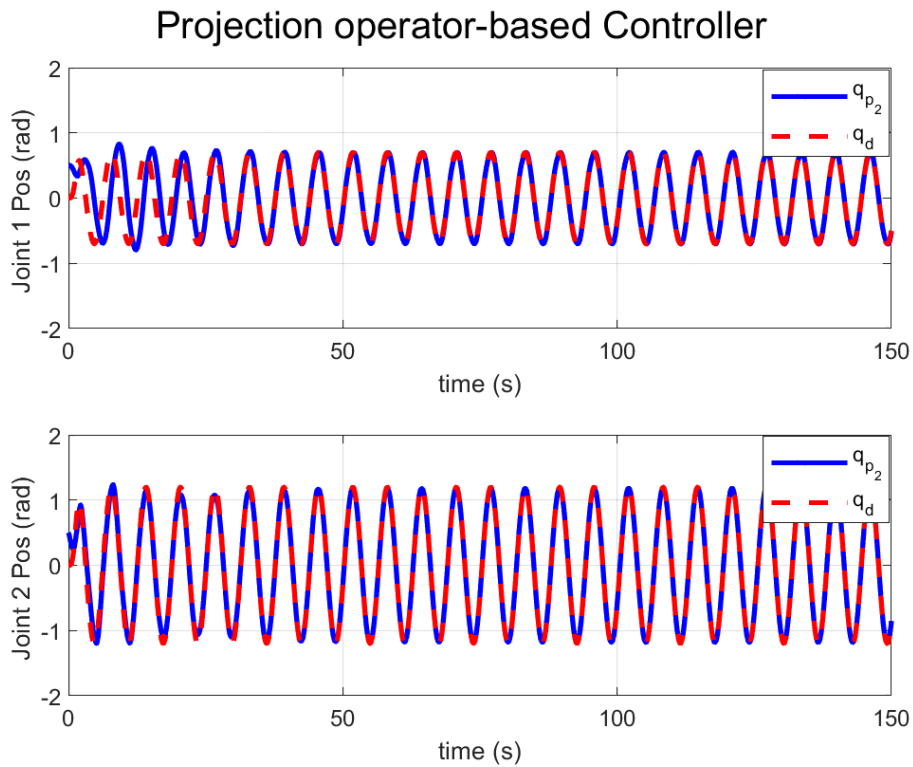
Figure 4.5 Tracking via PAC for 75% actuator deficiency.
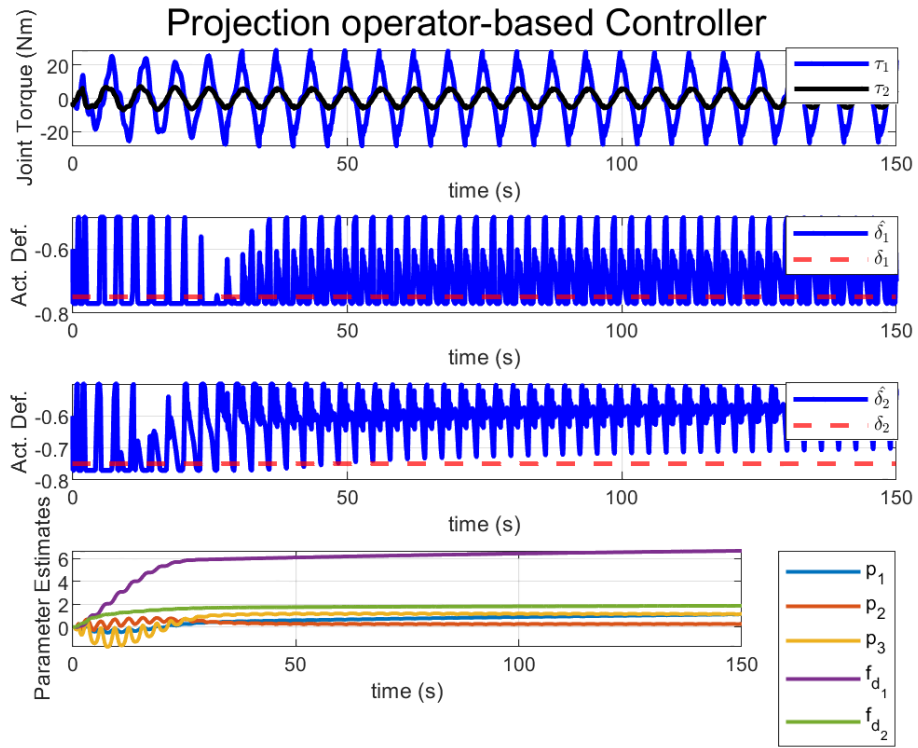
Figure 4.6 Torque and estimated parameters via PAC for 75% actuator deficiency.

5 Experimental Results and Discussion

In this chapter, the comprehensive results of the conducted experimental validation are presented. These results provide a detailed examination of the performance of the novel adaptive controllers under various conditions. They highlight the resilience and effectiveness of the controllers in maintaining control of the robotic arm manipulator subject to of substantial actuator deficiencies and uncertain dynamical parameters. The results also demonstrate the ability of the controllers to track desired trajectories satisfactorily and reduce error over time.

5.1 Results

In the forthcoming section, a comprehensive set of data is presented and organized to ensure maximum clarity. The data are categorized into distinct sections based on the type of information presented, such as joint angles, estimated terms, joint torques, and more. These sections are further divided based on the number of actuator deficiencies, facilitating comparative analysis of plots for the different update laws.

The actuator deficiency is enforced by multiplying the commanded τ from the adaptive controller by $I_2 + \delta_\Lambda$, where 20%, 40%, 60%, and 80% deficiencies and 40% overdriven cases are considered. For example, a 60% deficiency corresponds to a δ_Λ of -0.6 and 40% overdrive corresponds to a δ_Λ of 0.4. The adaptation gains for all cases are set to $\Gamma = 1I_6$ and $\gamma = 0.5I_2$ for the projection-based controller and $\Gamma = 3I_6$ and $\gamma = 0.5I_2$ for the bound-based controller. These gains were chosen because the $\hat{\phi}$ for the bound-based controller needed to be larger for the $\hat{\phi}$ to converge by the final time. The only exception is for the 40% overdriven case where $\Gamma = 3I_6$ and $\gamma = 5I_2$ for both controllers. The ε for the projection operator was set to 0.1 for all cases.

The upper and lower bounds and the projection bounds are selected differently for most cases; see the caption for exact bounds. Moreover, the control gains for all cases were set to $K_r = diag(40, 60)$, $k_n = 1$, and $\mu = 3I_2$. Note that these do meet the stability conditions from Equation (3.37) set by the stability analysis Section 3.2.1. The desired trajectory was the shoulder joint oscillating 10 degrees and the elbow joint oscillating 15 degrees with a period of about 6.25 seconds.

5.1.1 Joint Angle Tracking

This section provides a comprehensive presentation of the experimental results related to joint angle tracking across all cases, utilizing the two distinct controllers that were proposed in Section 3.2, namely the bound-based controller and the projection operator-based controller. The figures are systematically organized in ascending order of deficiency level, ensuring a logical progression in the data presentation. The results derived from this section are subsequently analyzed in Section 5.2.2, where pivotal initial conclusions are drawn.

The analysis commences with the 40% overdrive case. Figures 5.1 and 5.2 offer the tracking results of the bound-based and projection operator-based controllers respectively. Transitioning to deficiency cases, the 20% deficiency case is considered first. Figures 5.3 and 5.4 respectively represent the tracking performance of the bound-based and projection operator-based controllers. The exploration proceeds to the 40% deficiency case. Figures 5.5 and 5.6 respectively illustrate the tracking results for the bound-based and projection operator-based controllers. The 60% deficiency case follows, where Figures 5.7 and 5.8 respectively depict the outcomes of the tracking performance for the bound-based and projection operator-based controllers. The final scenario presented, and the most challenging, the 80% deficiency case. Figures 5.9 and 5.10 respectively showcase the tracking results for the bound-based and projection operator-based controllers, providing valuable insights into their performance under extreme conditions.

The control gains were set to $K_r = diag(40, 60)$, $k_n = 1$, and $\mu = 3I_2$ and the desired trajectory was the shoulder joint oscillating 10 degrees and the elbow joint oscillating 15 degrees with a period of about 6.25 seconds. The bounds are the same for both controllers and were set as follows: For the 40% overdrive case, the upper and lower bounds are $\hat{\delta}_{\lambda_{max}} = 0.6$, $\hat{\delta}_{\lambda_{min}} = 0.2$, respectively. For the deficiency cases, the lower bound was always set to $\hat{\delta}_{\lambda_{min}} = -0.9$; however the lower bound changes as the deficiency increases. Specifically, at 20% deficiency $\hat{\delta}_{\lambda_{min}} = -0.1$, at 40% deficiency $\hat{\delta}_{\lambda_{min}} = -0.2$, and at 60% and 80% deficiencies $\hat{\delta}_{\lambda_{min}} = -0.4$. Finally, the initial conditions were set to be inside the bounds; therefore $\hat{\delta}_{\lambda_0} = 0.5$ for the 40% overdrive case and $\hat{\delta}_{\lambda_0} = -0.5$ for all deficiency cases.
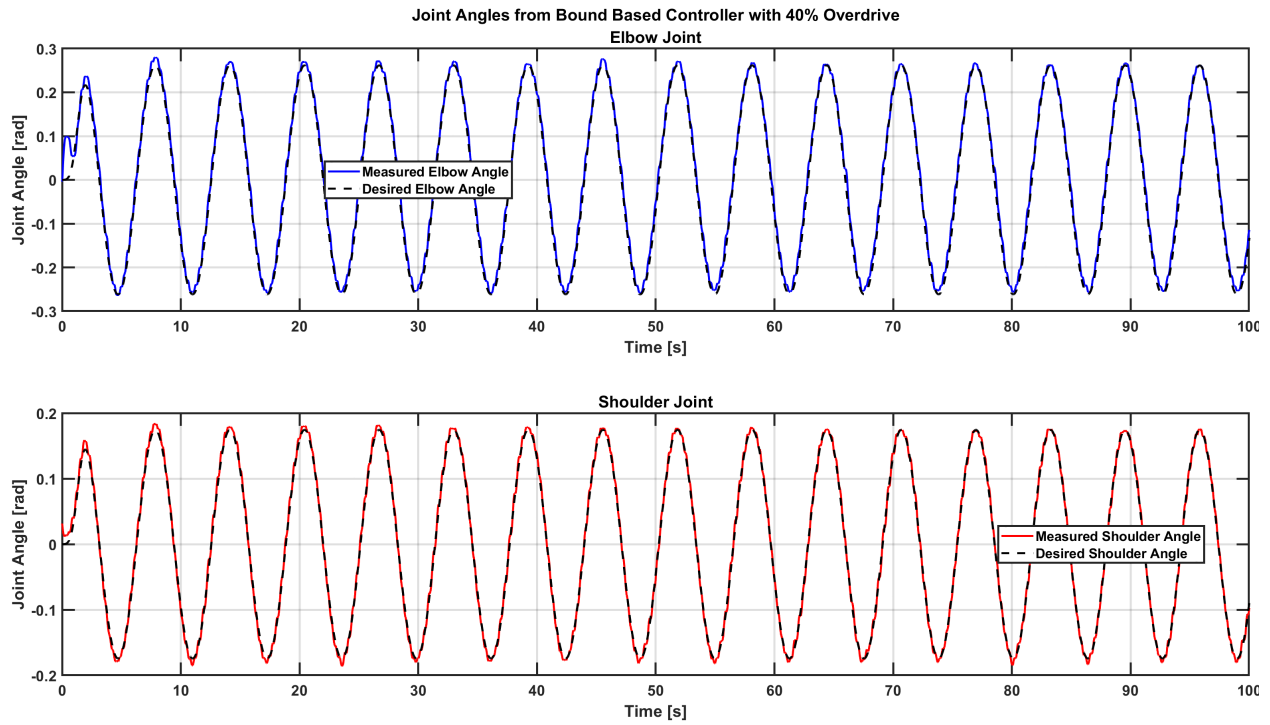
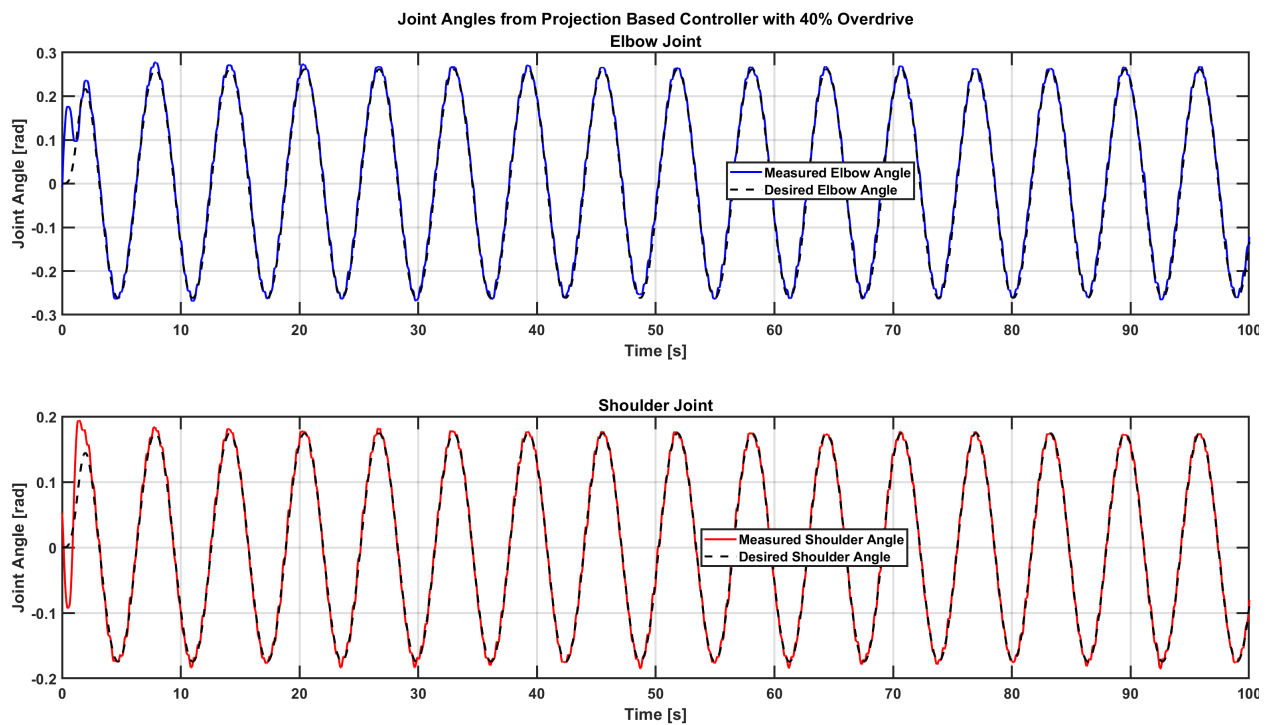*Figure 5.1* Joint angles via BAC with over actuation (40%).

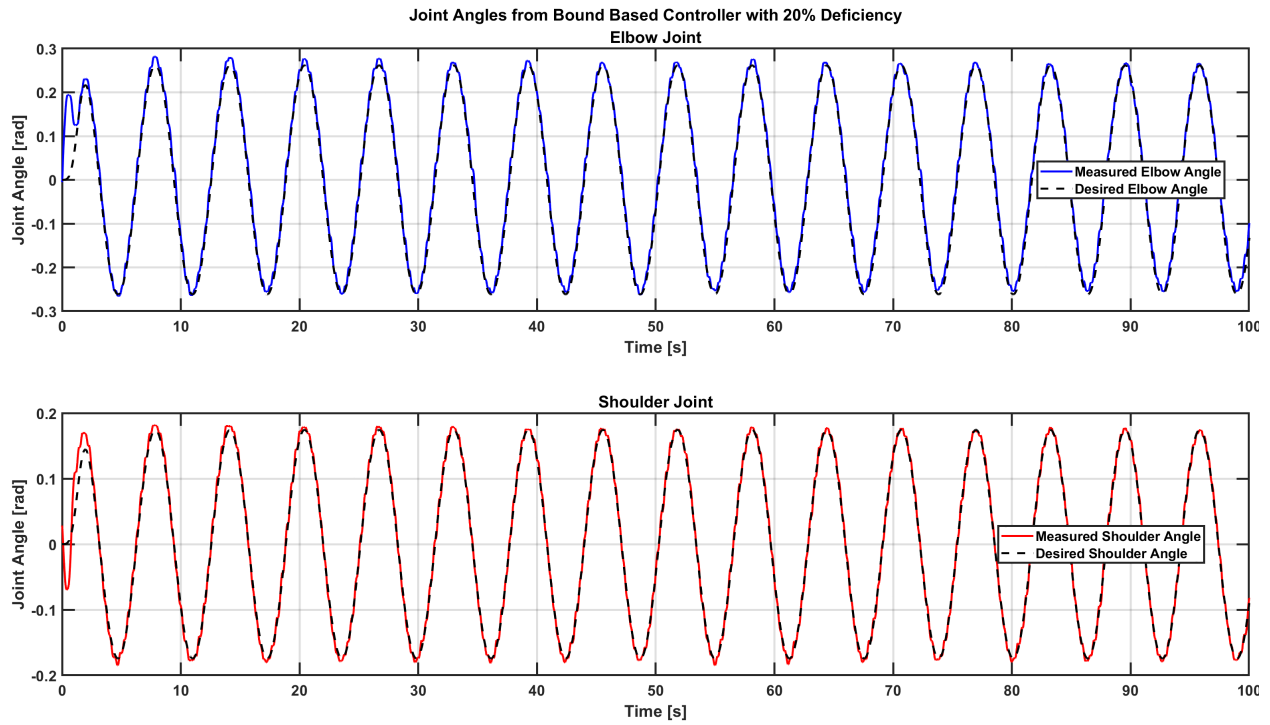*Figure 5.2* Joint angles via PAC with over actuation (40%).

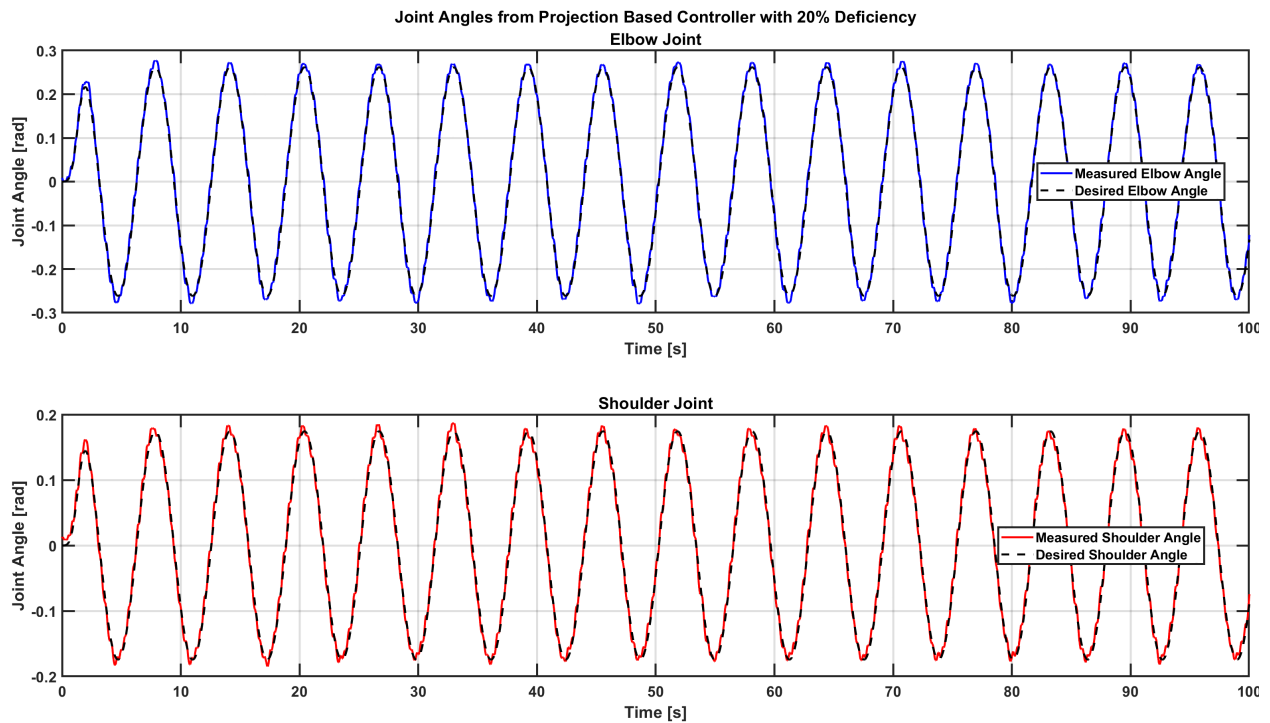*Figure 5.3* Joint angles via BAC with actuator deficiency (20%).

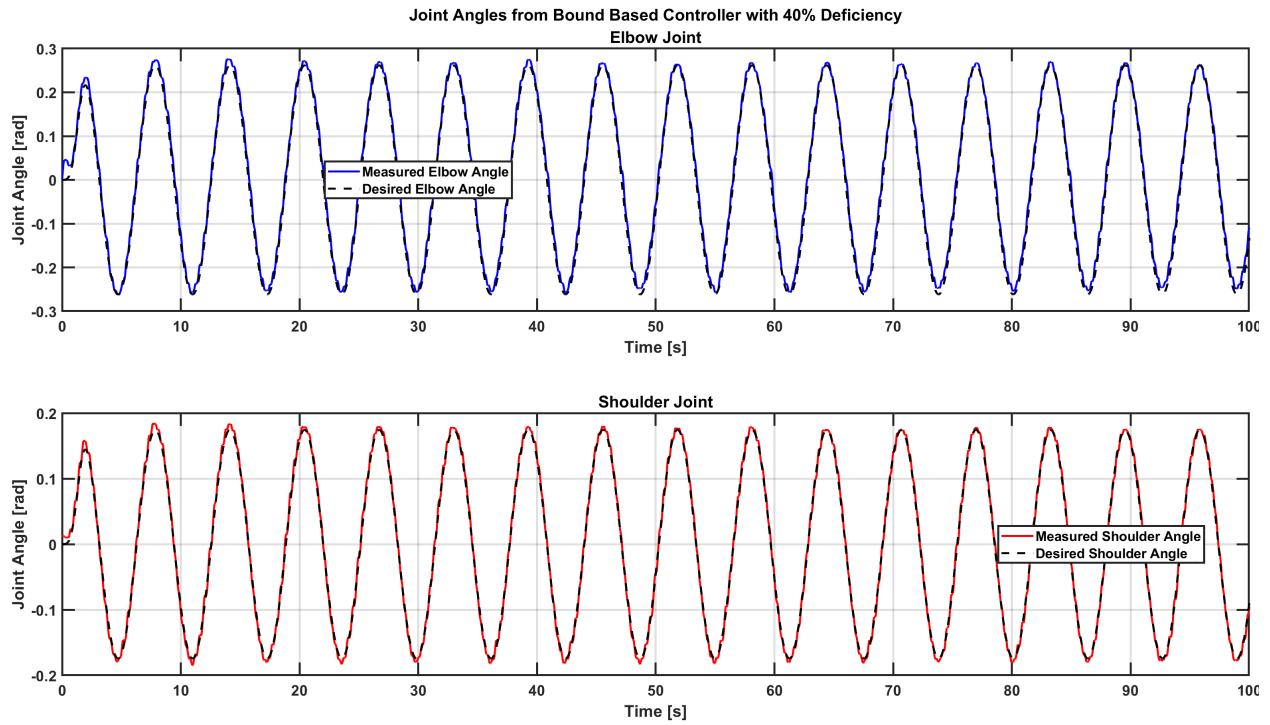*Figure 5.4* Joint angles via PAC with actuator deficiency (20%).

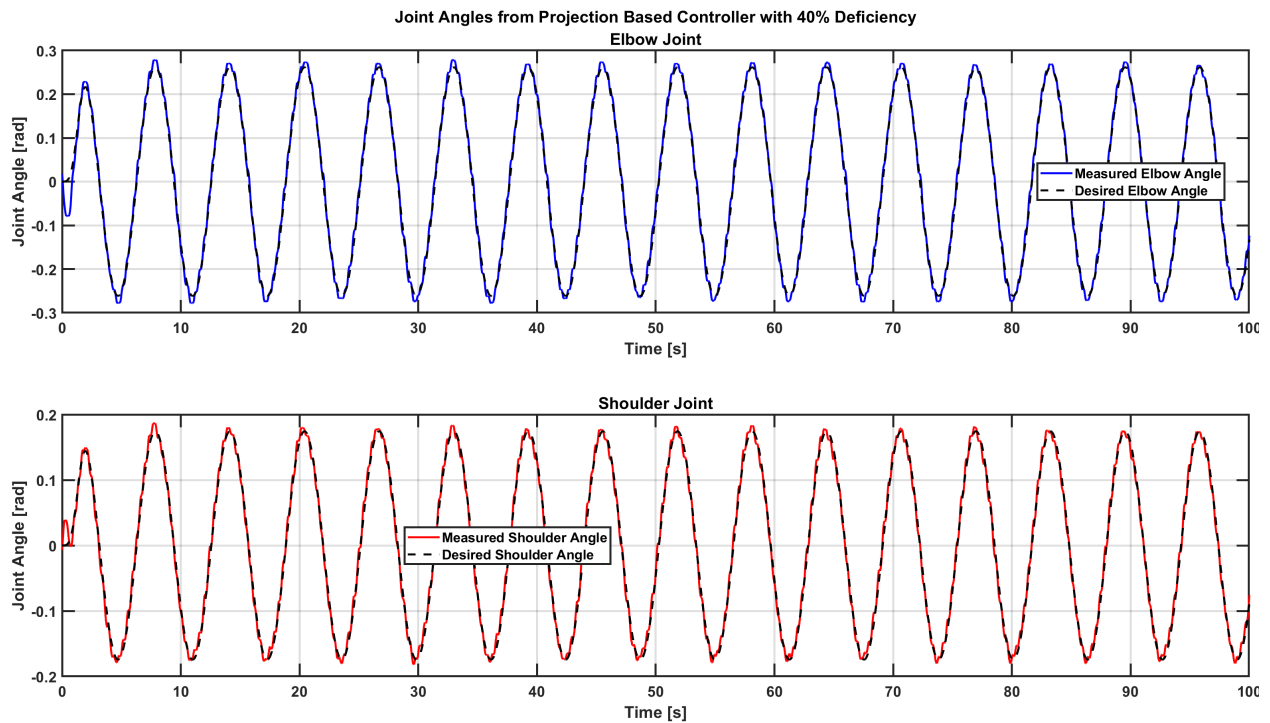*Figure 5.5* Joint angles via BAC with actuator deficiency (40%).

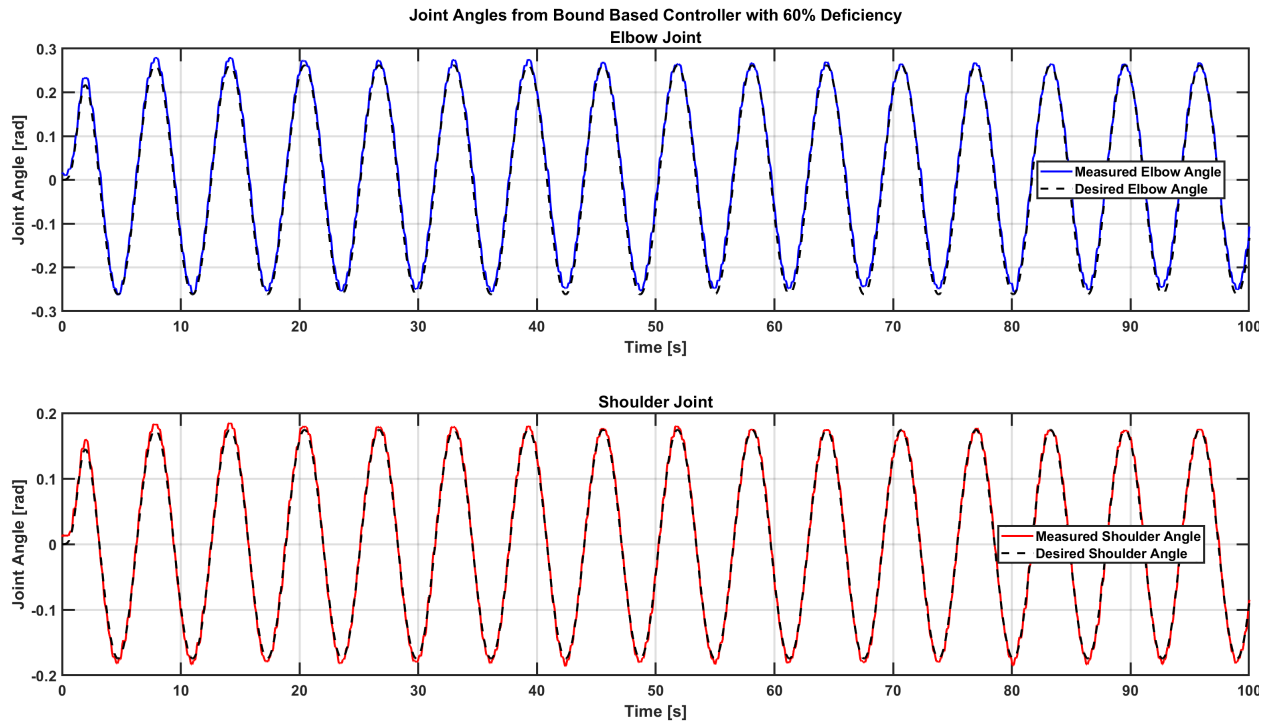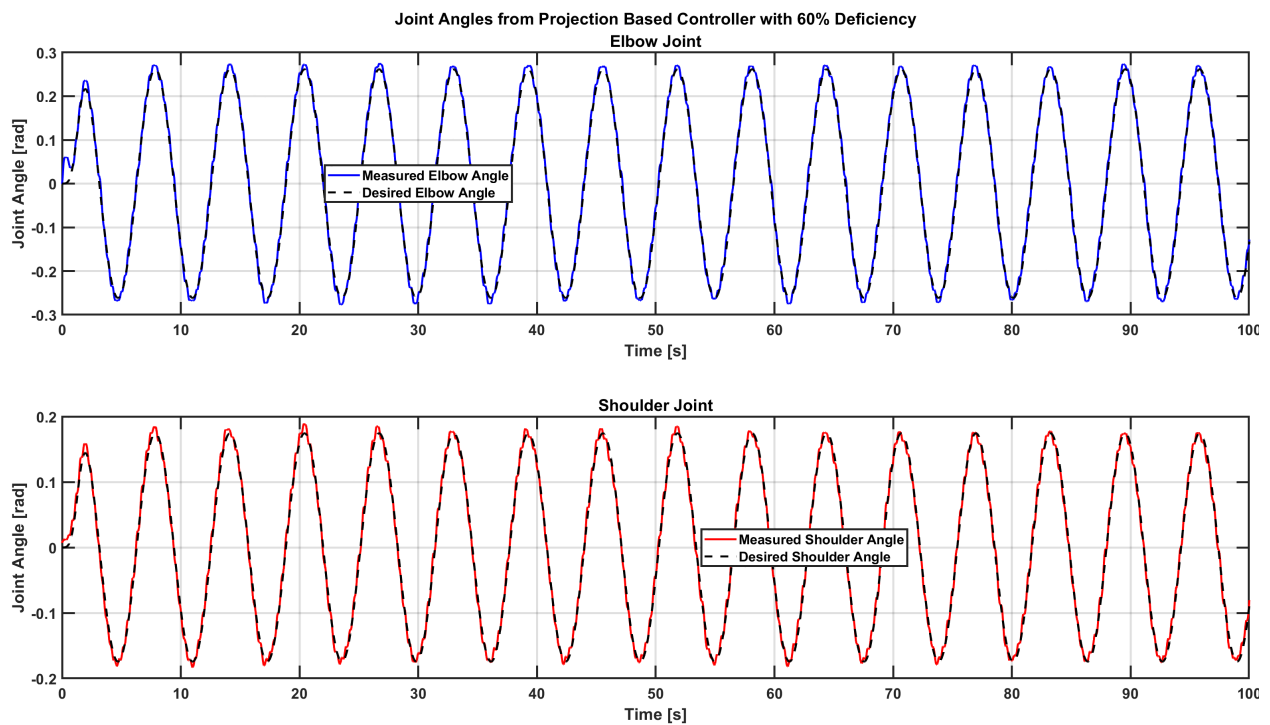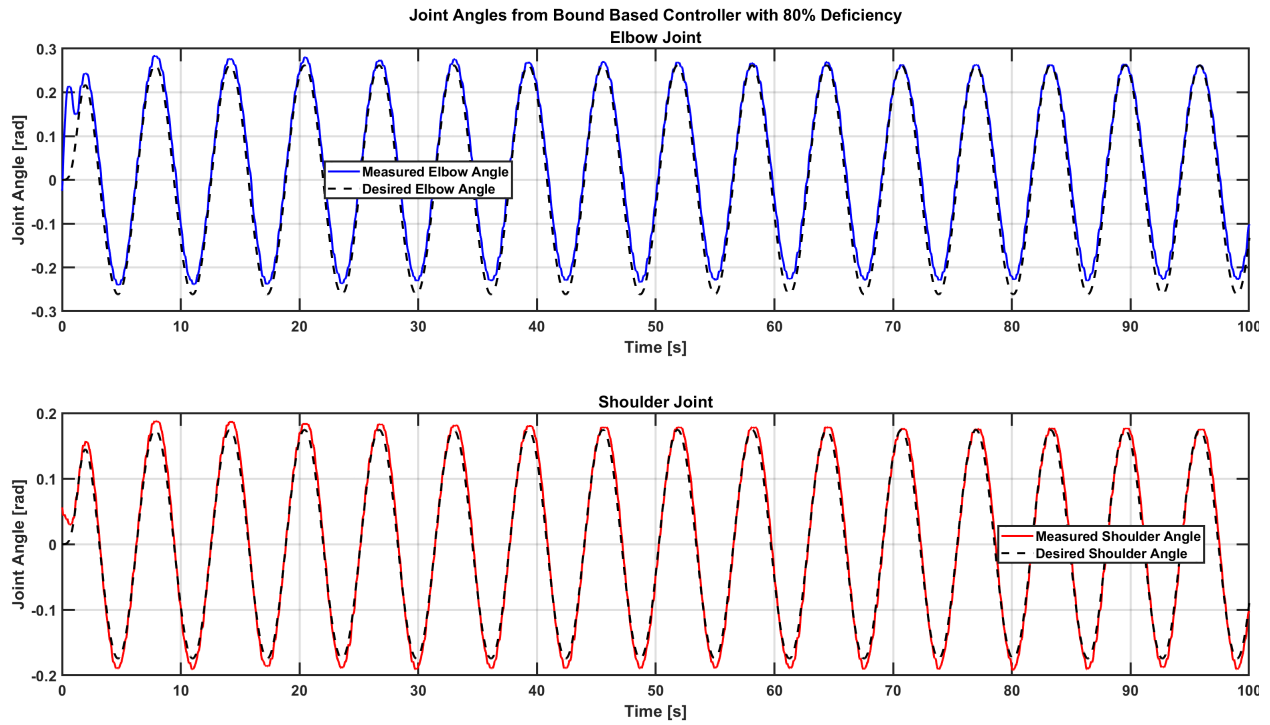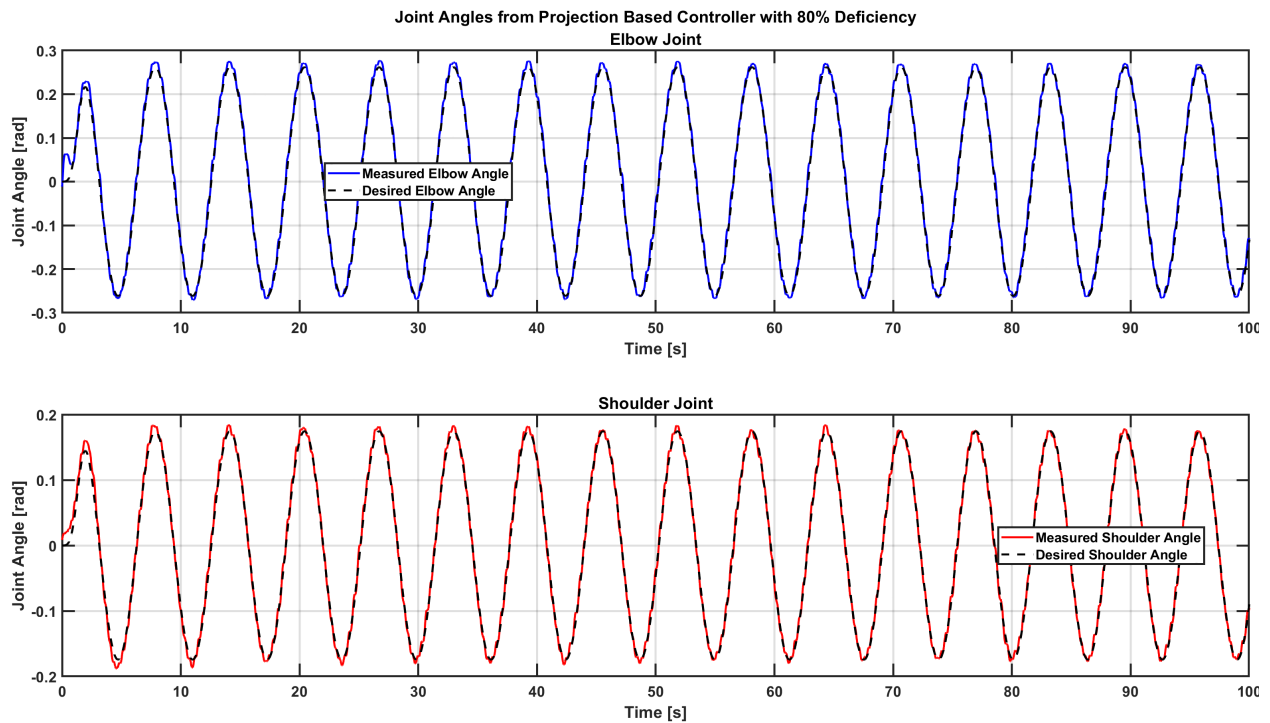*Figure 5.6* Joint angles via PAC with actuator deficiency (40%).

44

Figure 5.7 Joint angles via BAC with actuator deficiency (60%).

Figure 5.8 Joint angles via PAC with actuator deficiency (60%).

Figure 5.9 Joint angles via BAC with actuator deficiency (80%).

Figure 5.10 Joint angles via PAC with actuator deficiency (80%).

5.1.2 Joint Angular Velocities

In this section, a detailed exposition of the experimental outcomes for joint angular velocity tracking across all test scenarios is provided for the bound-based controller and the projection operator-based controller. The associated figures are sequenced in the same ascending order of deficiency level. The results of this section are analyzed in Section 5.2.3.

Firstly, the 40% overdrive scenario, where Figures 5.11 and 5.12 offer a comparison of the joint angular velocity results of the bound-based and projection operator-based controllers. Then, the 20% deficiency case joint angular velocity performance of the bound-based and projection operator-based controllers are represented in Figures 5.13 and 5.14 respectively. Subsequently, the 40% deficiency case is explored, with Figures 5.15 and 5.16 showcasing the joint angular velocity results for the bound-based and projection operator-based controllers. Next, the 60% deficiency case, where Figures 5.17 and 5.18 capture the joint angular velocity performance outcomes of the bound-based and projection operator-based controllers. The section concludes with an examination of the most challenging scenario, the 80% deficiency case where Figures 5.19 and 5.20 provide the performance joint angular velocity results for the bound-based and projection operator-based controllers.

The control gains were set to $K_r = diag(40, 60)$, $k_n = 1$, and $\mu = 3I_2$ and the desired trajectory was the shoulder joint oscillating 10 degrees and the elbow joint oscillating 15 degrees with a period of about 6.25 seconds. The bounds are the same for both controllers but were set differently for different actuator deficiencies. For the 40% overdrive case, the upper and lower bounds are $\hat{\delta}_{\lambda_{max}} = 0.6$, $\hat{\delta}_{\lambda_{min}} = 0.2$, respectively. For the deficiency cases, the lower bound was always set to $\hat{\delta}_{\lambda_{min}} = -0.9$; however the lower bound changes as the deficiency increases. Specifically, at 20% deficiency $\hat{\delta}_{\lambda_{min}} = -0.1$, at 40% deficiency $\hat{\delta}_{\lambda_{min}} = -0.2$, and at 60% and 80% deficiencies $\hat{\delta}_{\lambda_{min}} = -0.4$. Finally, the initial conditions were set to be inside the bounds; therefore $\hat{\delta}_{\lambda_0} = 0.5$ for the 40% overdrive case and $\hat{\delta}_{\lambda_0} = -0.5$ for all deficiency cases.
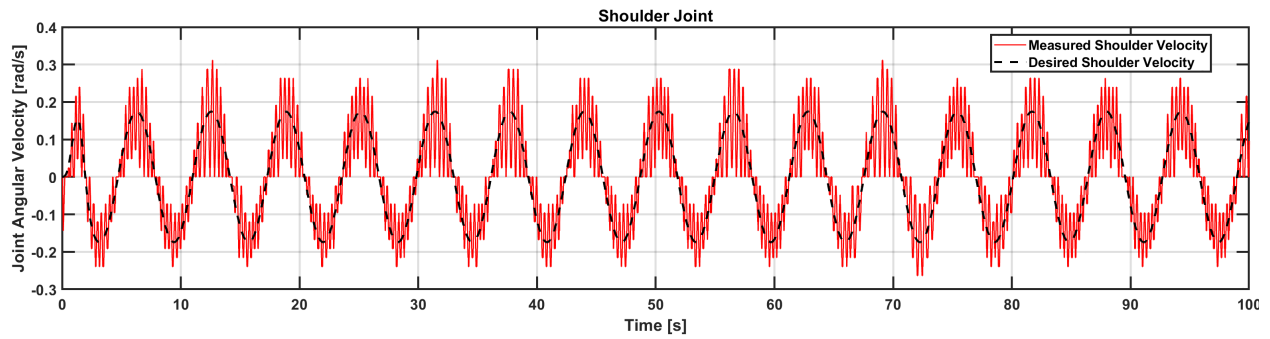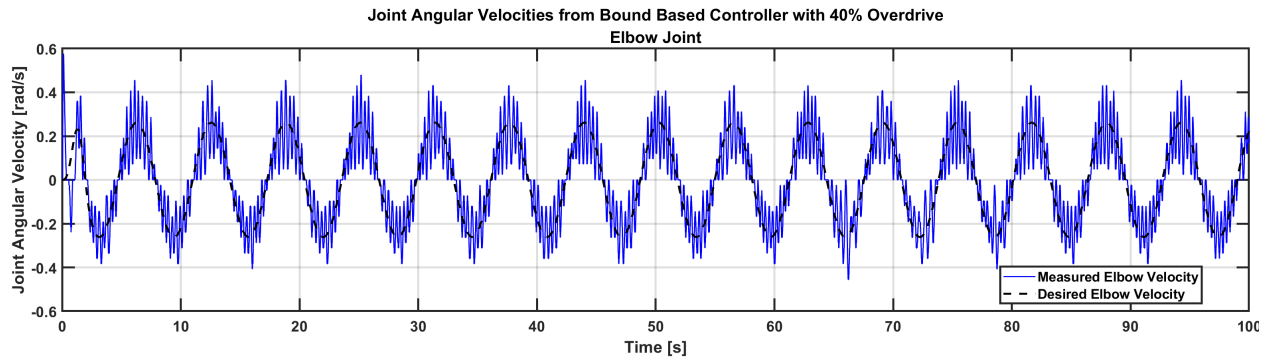
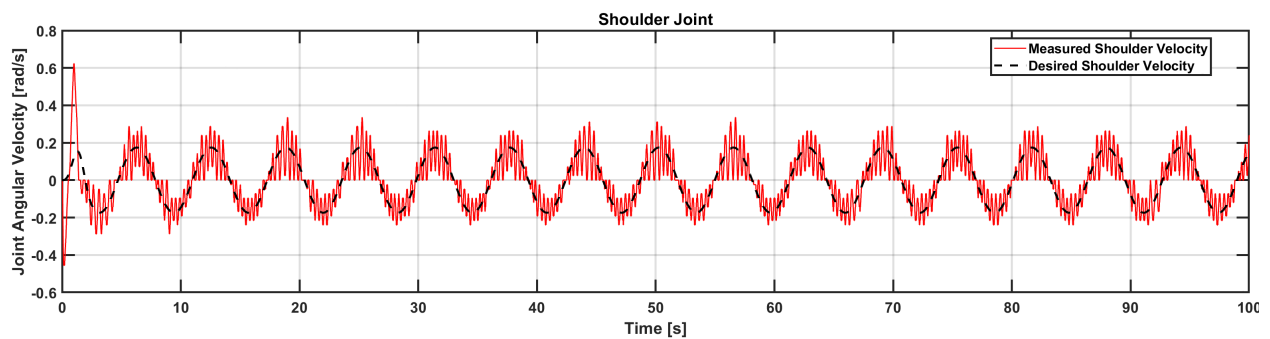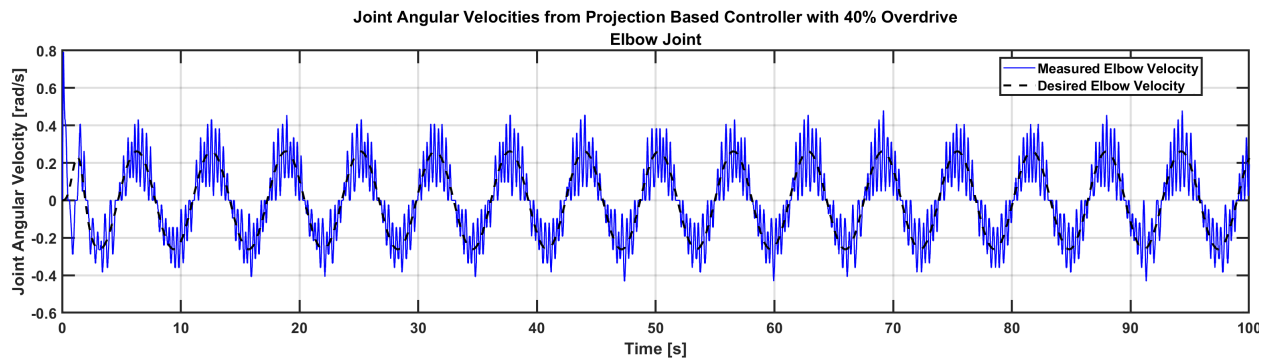*Figure 5.11* Angular velocities via BAC with over actuation (40%).

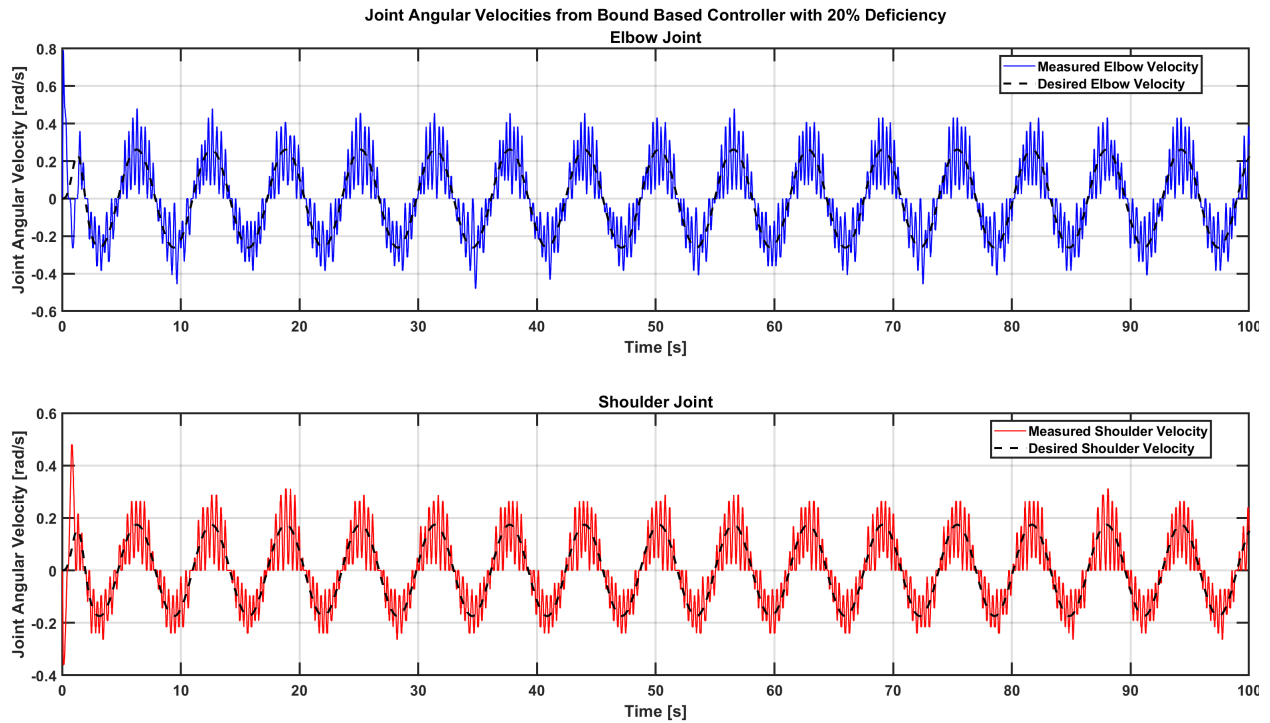*Figure 5.12* Angular velocities via PAC over actuation (40%).

Figure 5.13 Angular velocities via BAC with actuator deficiency (20%).
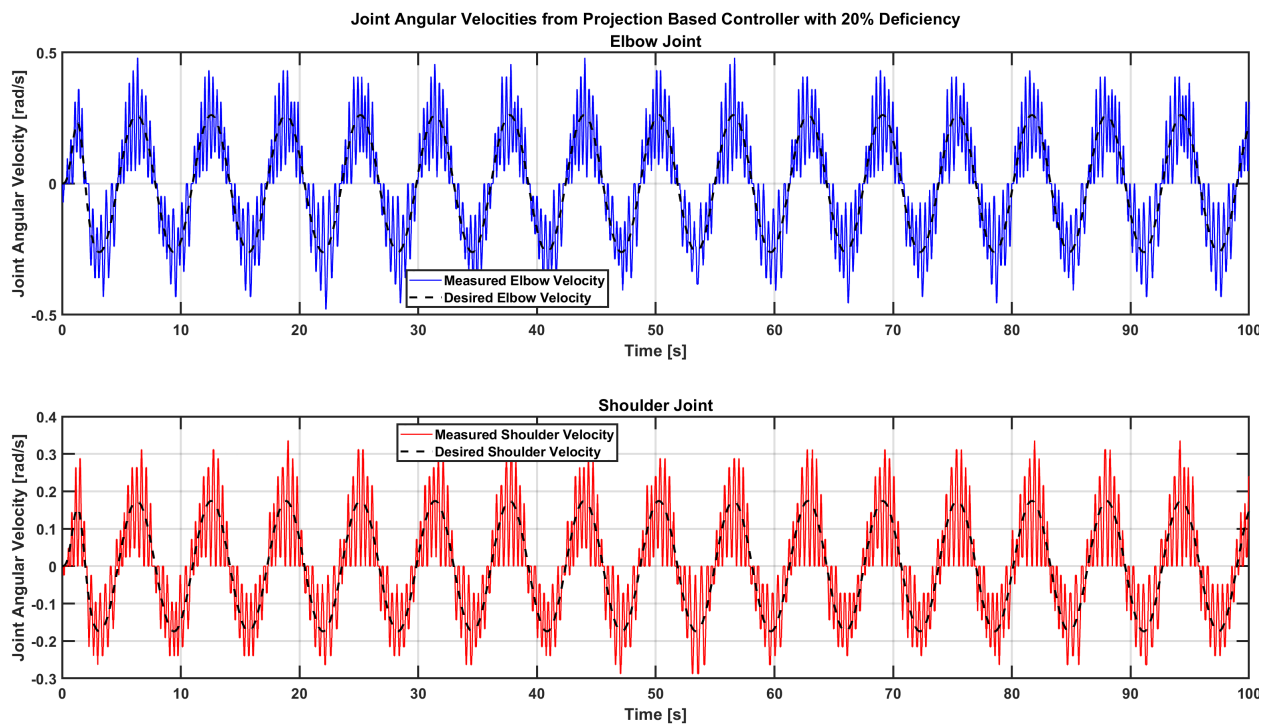

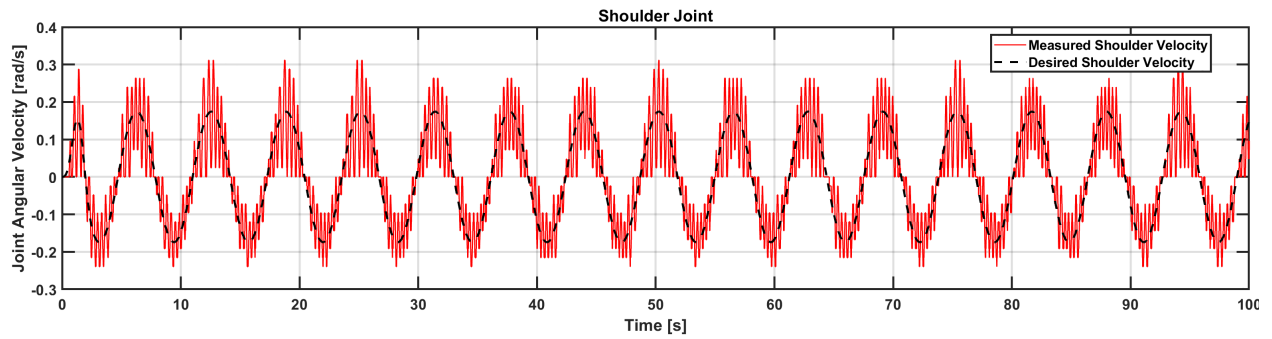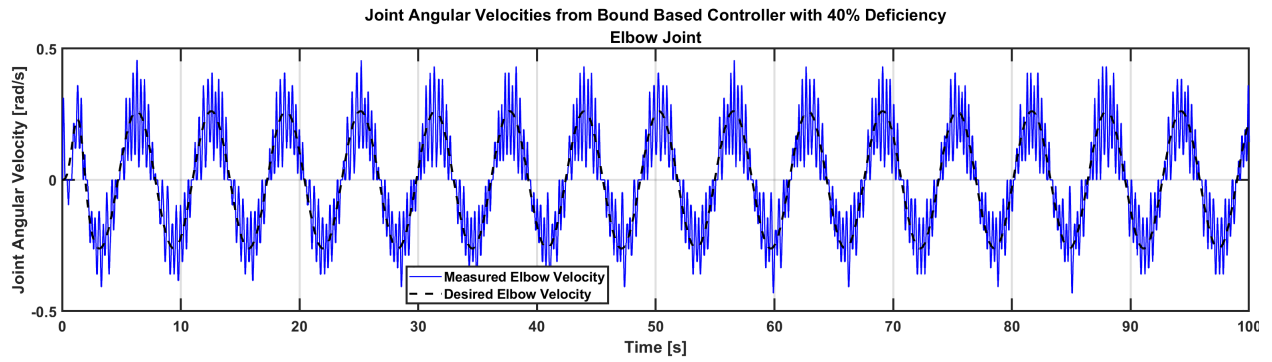*Figure 5.14* Angular velocities via PAC with actuator deficiency (20%).

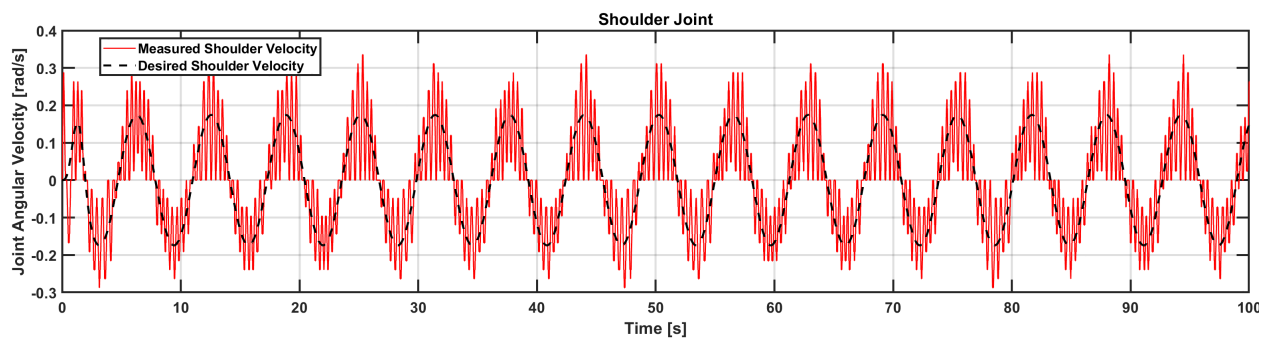*Figure 5.15* Angular velocities via BAC with actuator deficiency (40%).
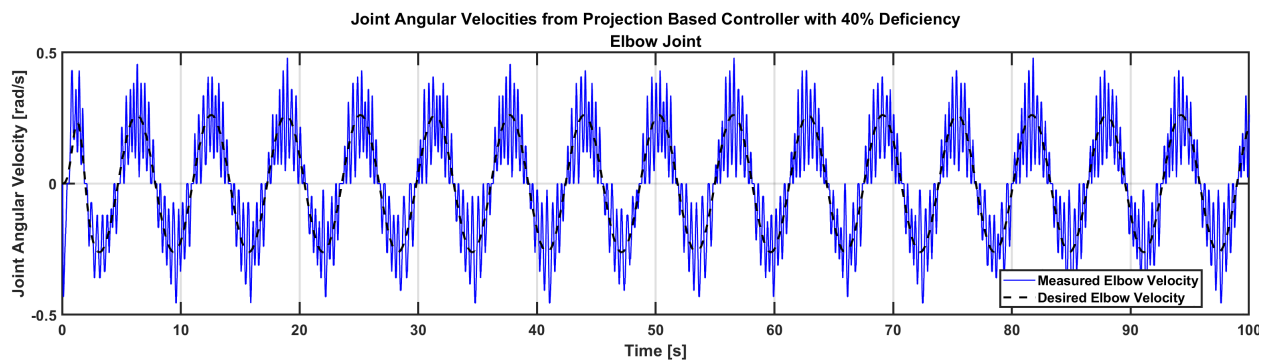

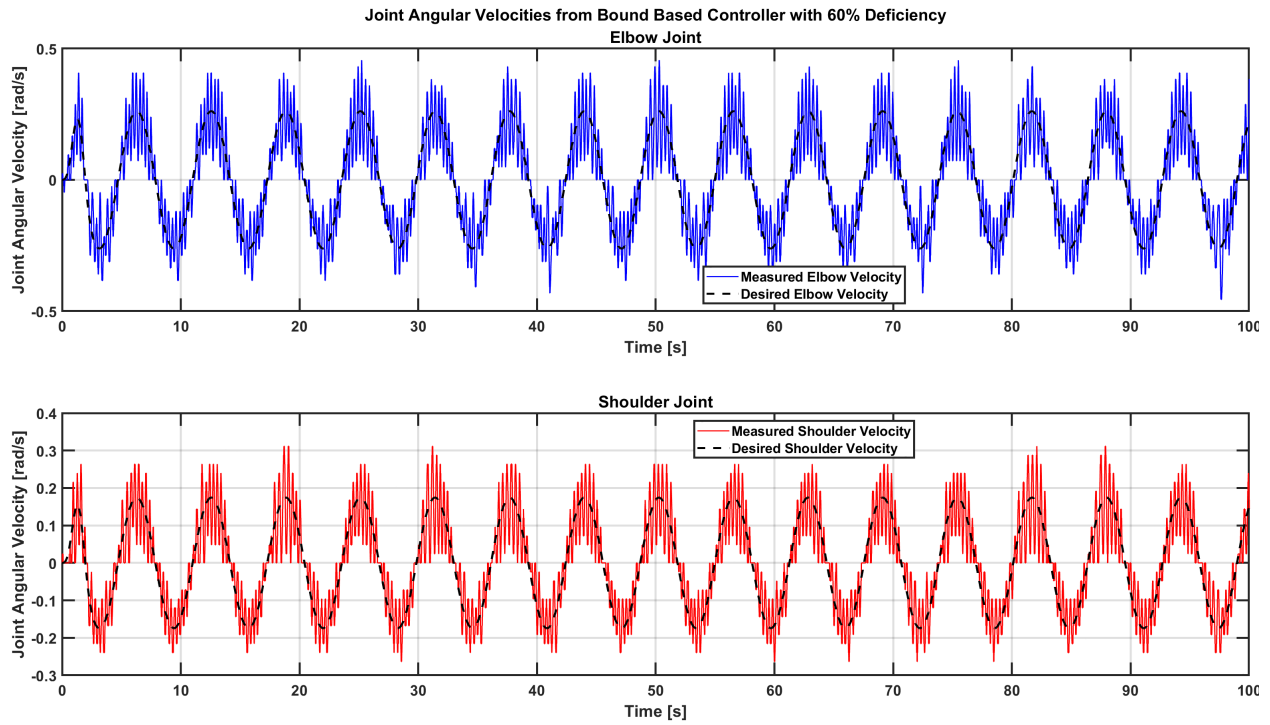*Figure 5.16* Angular velocities via PAC with actuator deficiency (40%).

50

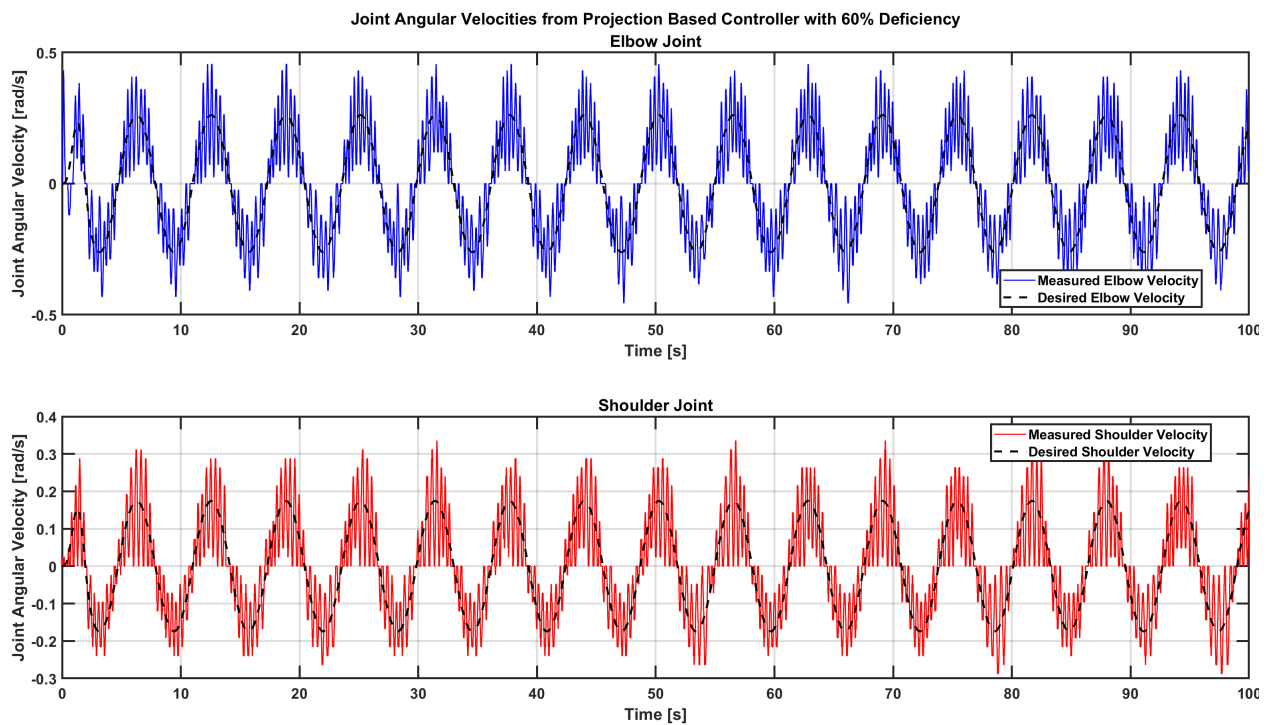*Figure 5.17* Angular velocities via BAC with actuator deficiency (60%).

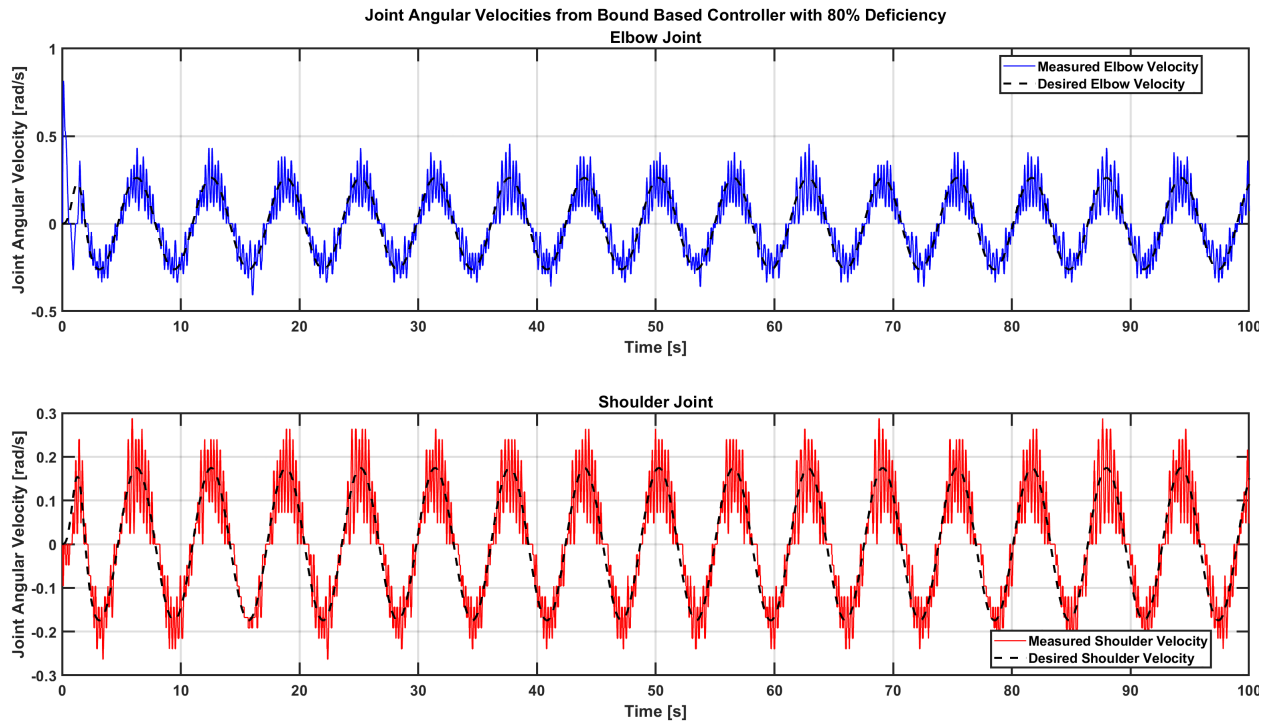*Figure 5.18* Angular velocities via PAC with actuator deficiency (60%).

51

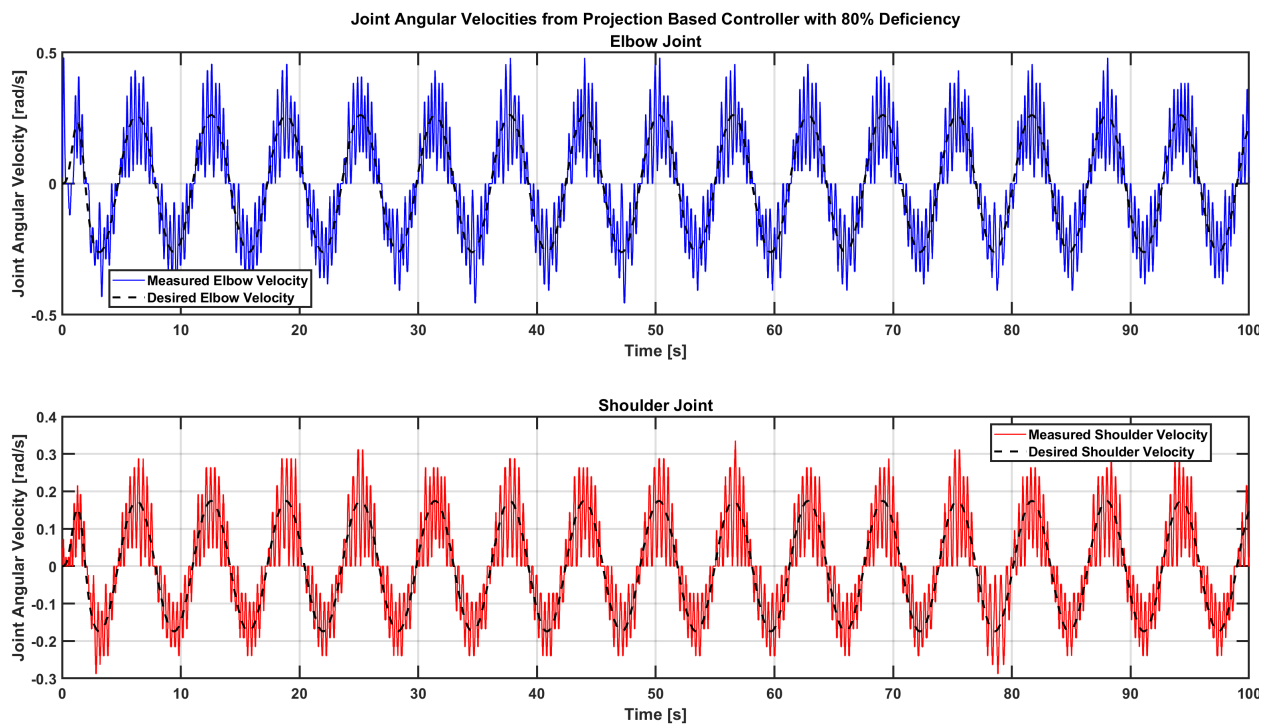*Figure 5.19* Angular velocities via BAC with actuator deficiency (80%).

Figure 5.20 Angular velocities via PAC with actuator deficiency (80%).

5.1.3 Joint Errors

In this section, a detailed exposition of the experimental outcomes for joint error tracking across all test scenarios is provided for the bound-based controller and the projection operator-based controller. The associated figures are sequenced in the same ascending order of deficiency level. The results of this section are analyzed in Section 5.2.4 where the difference of the two controllers are more easily seen.

Firstly, the 40% overdrive scenario is examined, where Figures 5.21 and 5.22 offer a comparison of the joint error tracking results of the bound-based and projection operator-based controllers. Then, the performance of the joint error tracking for the bound-based and projection operator-based controllers for the 20% deficiency case is represented in Figures 5.23 and 5.24 respectively. Subsequently, the 40% deficiency case is explored, with Figures 5.25 and 5.26 showcasing the joint error tracking results for the bound-based and projection operator-based controllers. Next, the 60% deficiency case is discussed, where Figures 5.27 and 5.28 capture the joint error tracking performance outcomes of the bound-based and projection operator-based controllers. Finally, Figures 5.29 and 5.30 provide the joint error tracking results for the bound-based and projection operator-based controllers at an 80% actuator deficiency.

The control gains were set to $K_r = diag(40, 60)$, $k_n = 1$, and $\mu = 3I_2$ and the desired trajectory was the shoulder joint oscillating 10 degrees and the elbow joint oscillating 15 degrees with a period of about 6.25 seconds. The bounds are the same for both controllers but were set differently for different actuator deficiencies. For the 40% overdrive case, the upper and lower bounds are $\hat{\delta}_{\lambda_{max}} = 0.6$, $\hat{\delta}_{\lambda_{min}} = 0.2$, respectively. For the deficiency cases, the lower bound was always set to $\hat{\delta}_{\lambda_{min}} = -0.9$; however the lower bound changes as the deficiency increases. Specifically, at 20% deficiency $\hat{\delta}_{\lambda_{min}} = -0.1$, at 40% deficiency $\hat{\delta}_{\lambda_{min}} = -0.2$, and at 60% and 80% deficiencies $\hat{\delta}_{\lambda_{min}} = -0.4$. Finally, the initial conditions were set to be inside the bounds; therefore $\hat{\delta}_{\lambda_0} = 0.5$ for the 40% overdrive case and $\hat{\delta}_{\lambda_0} = -0.5$ for all deficiency cases.
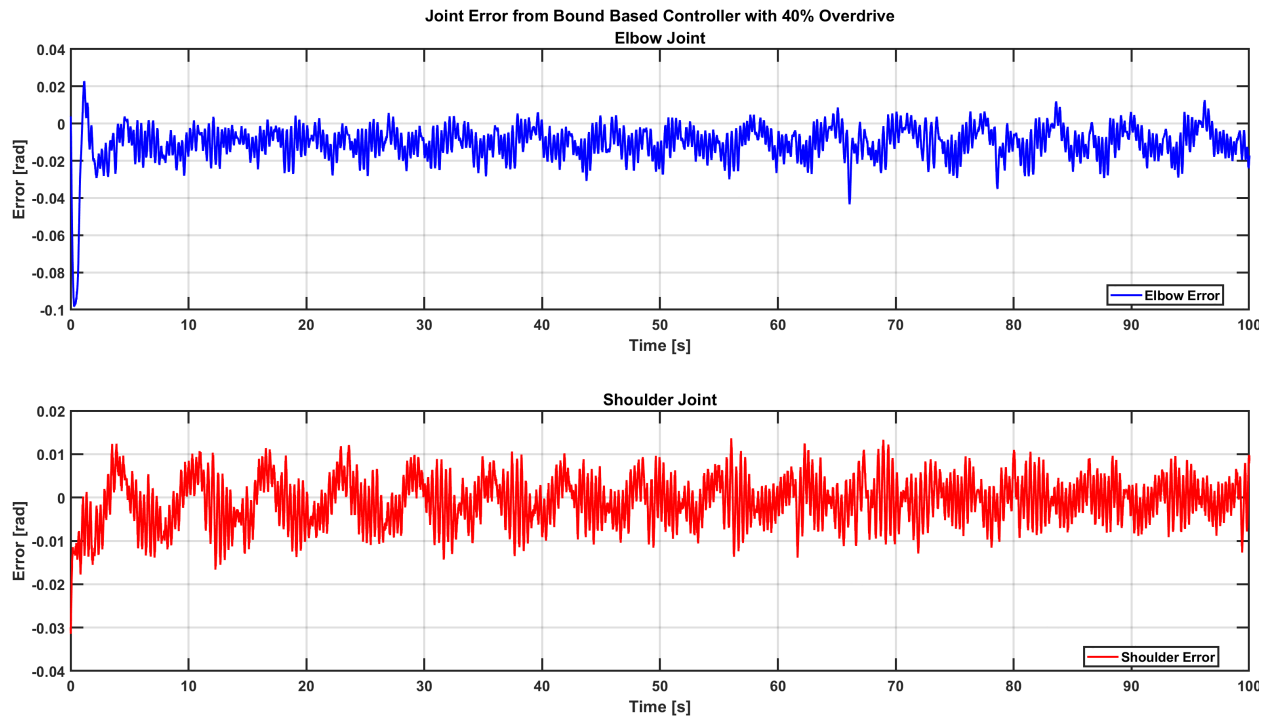
Figure 5.21 Error via BAC with over actuation (40%).

Figure 5.22 Error via PAC with over actuation (40%).
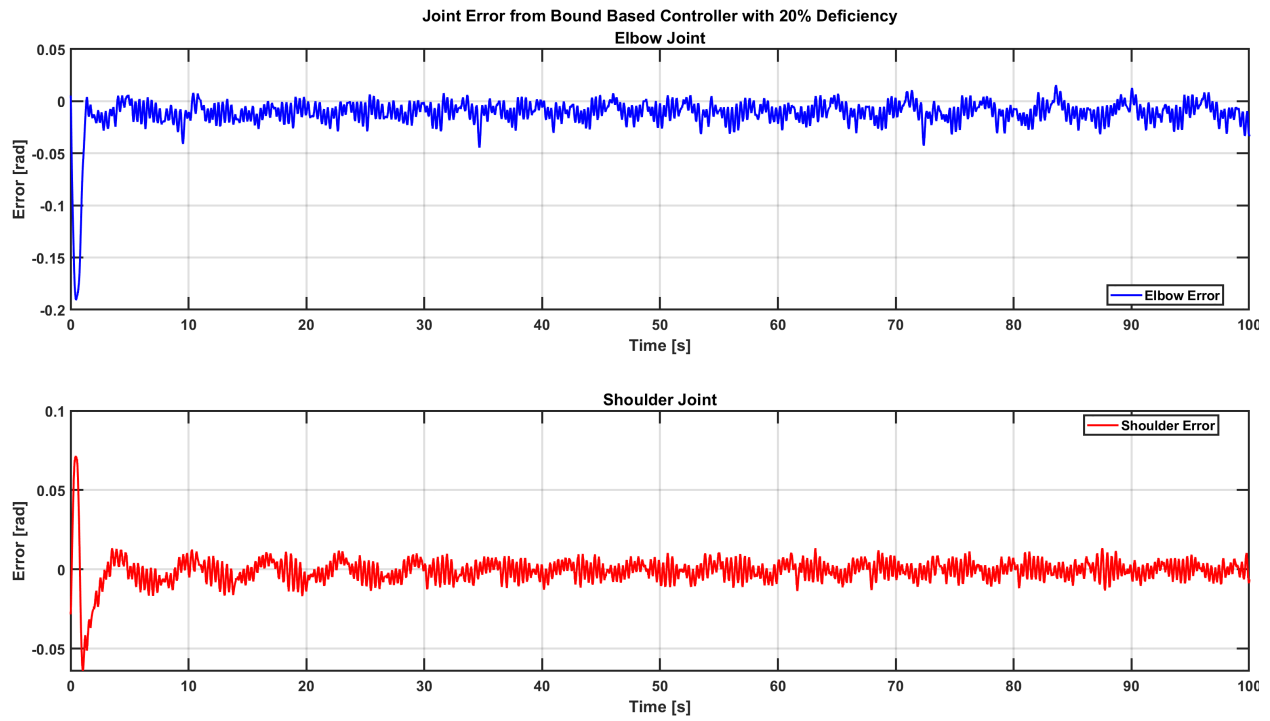
Figure 5.23 Error via BAC with actuator deficiency (20%).
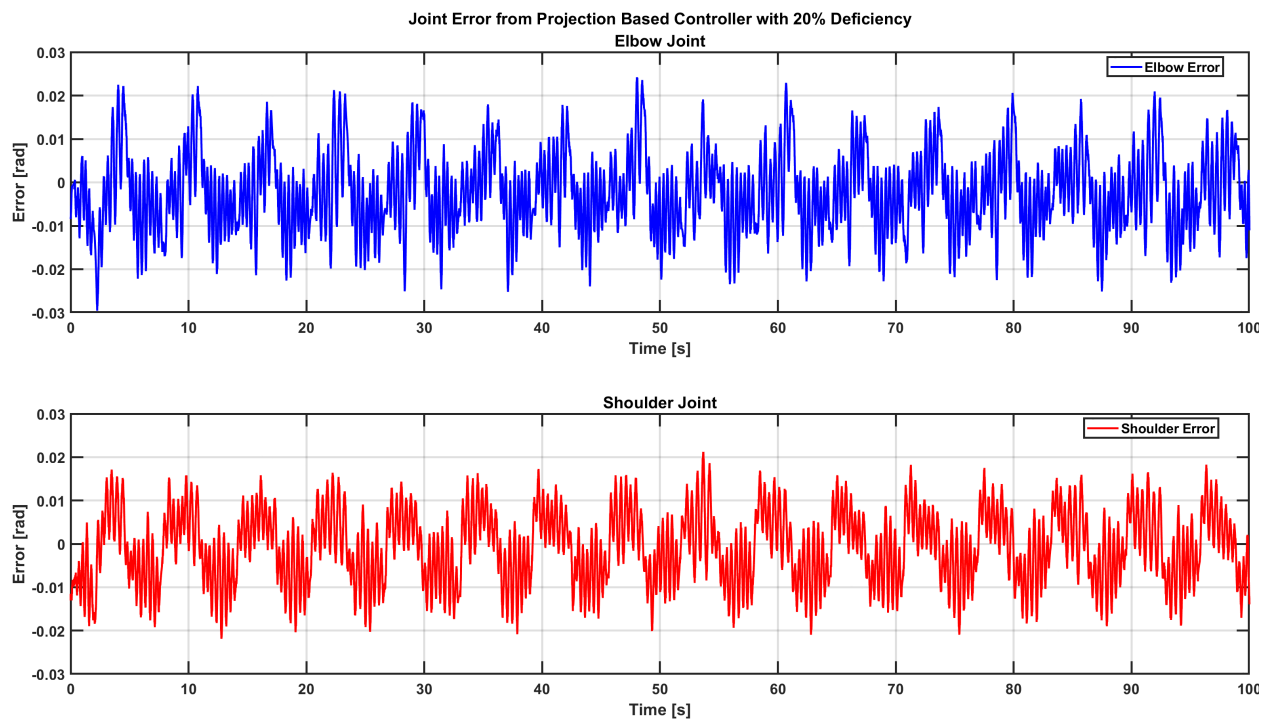
Figure 5.24 Error via PAC with actuator deficiency (20%).
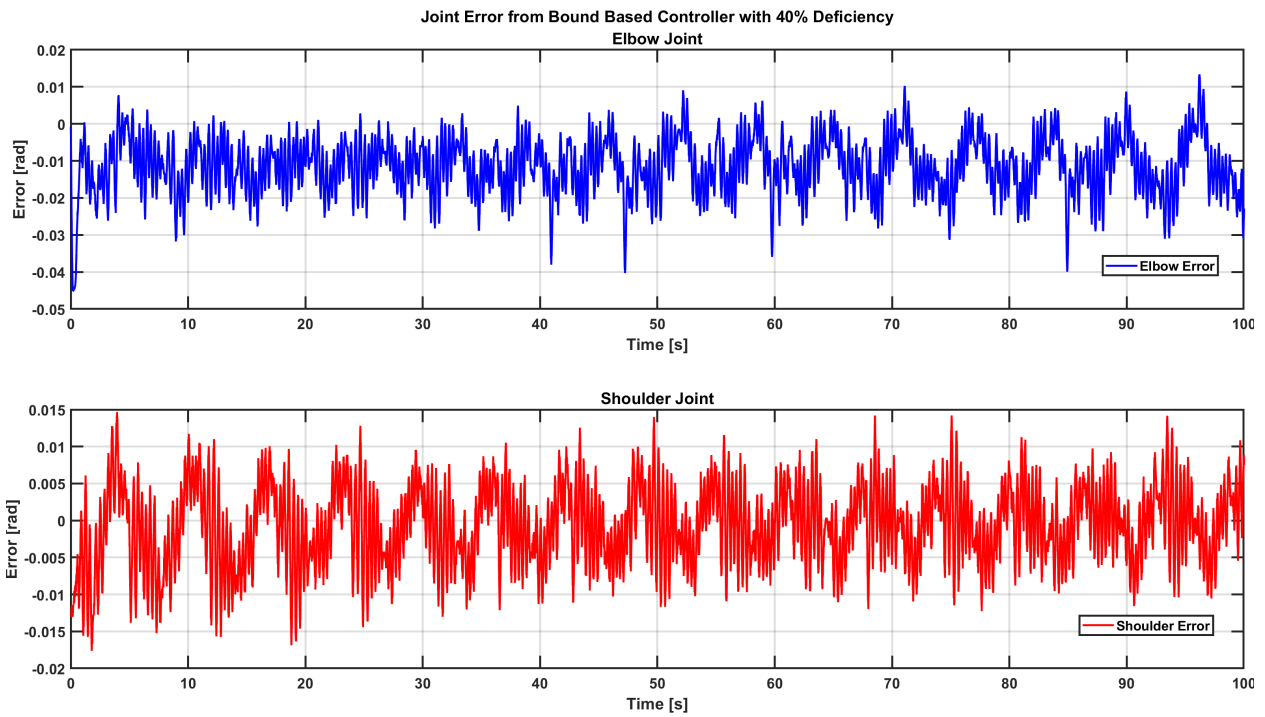
Figure 5.25 Error via BAC with actuator deficiency (40%).
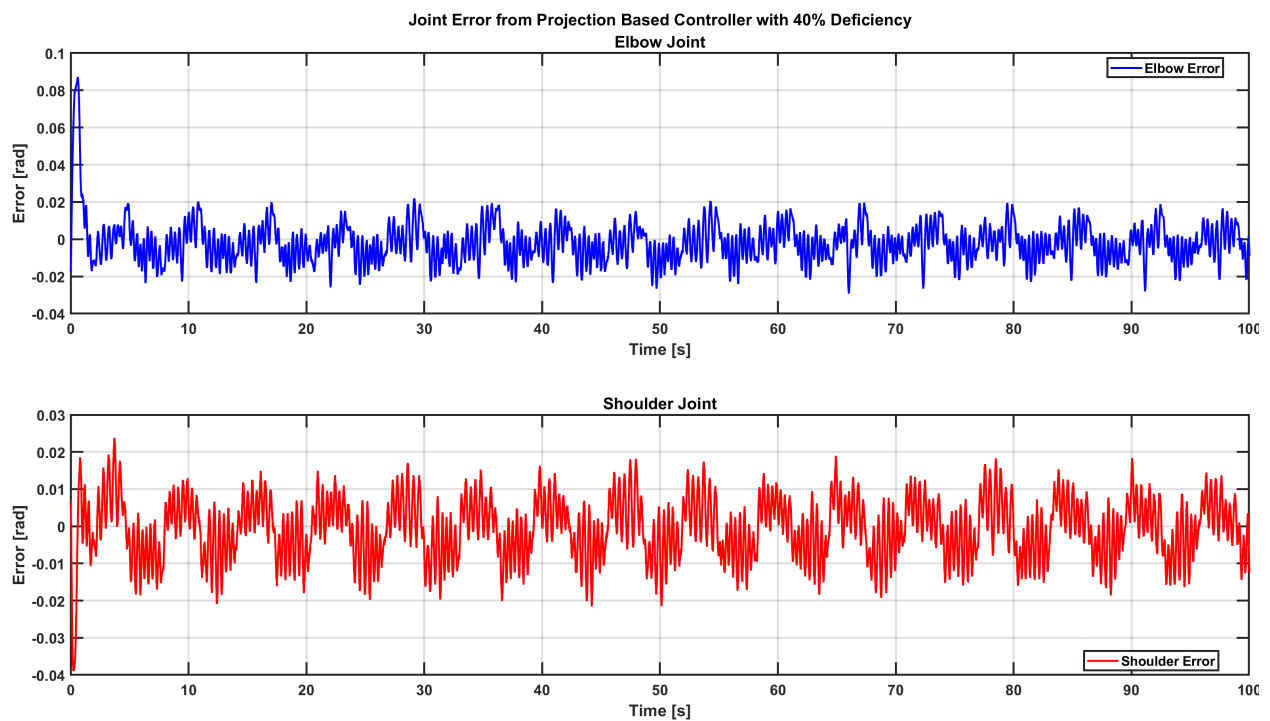
Figure 5.26 Error via PAC with actuator deficiency (40%).
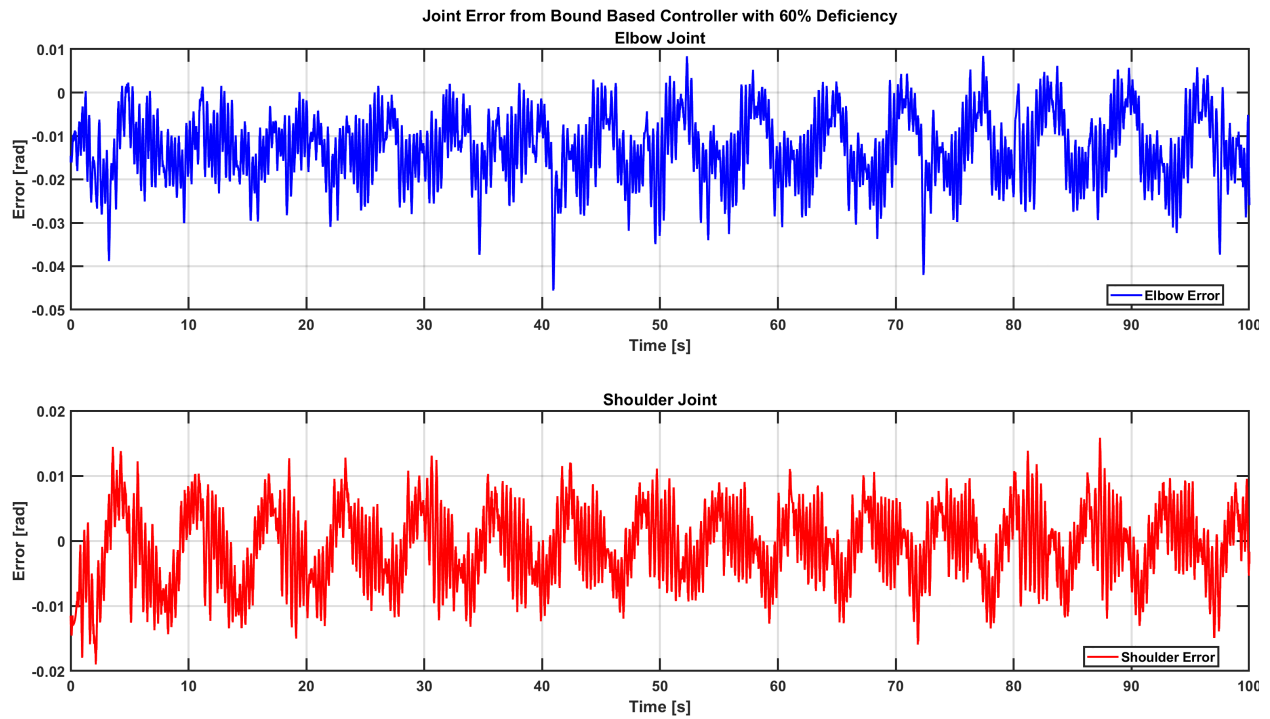
Figure 5.27 Error via BAC with actuator deficiency (60%).
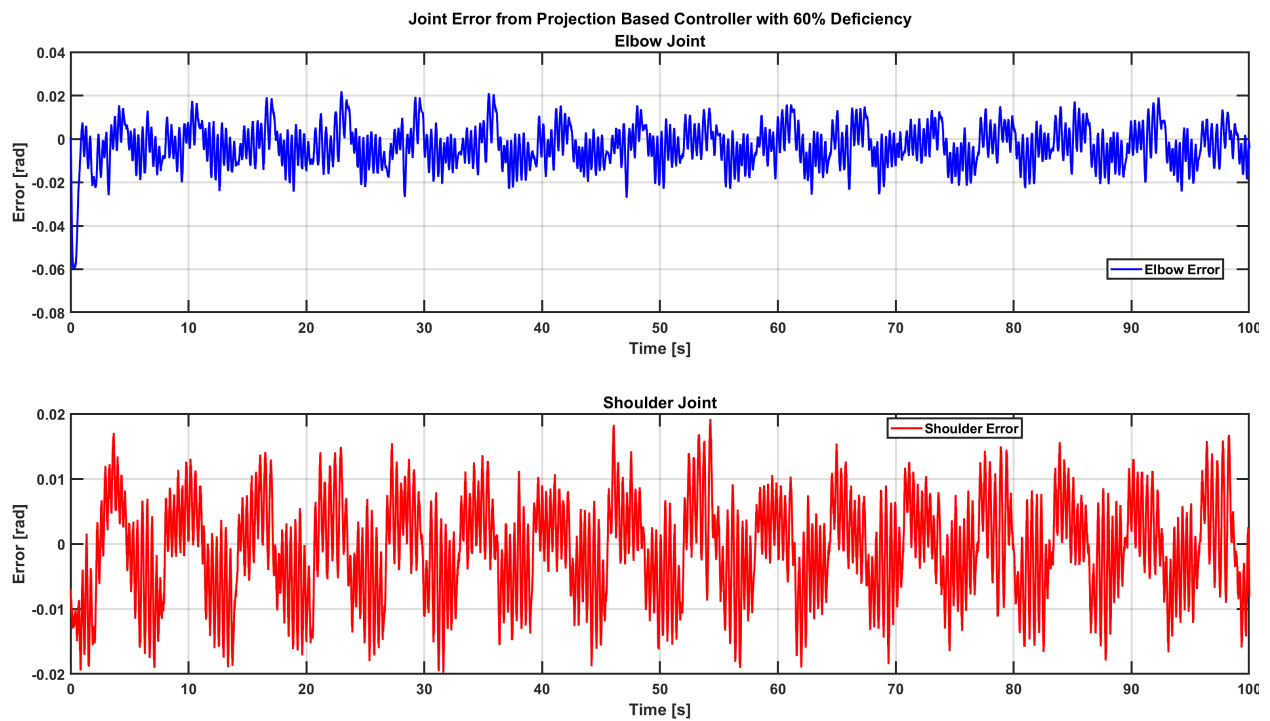
Figure 5.28 Error via PAC with actuator deficiency (60%).

57
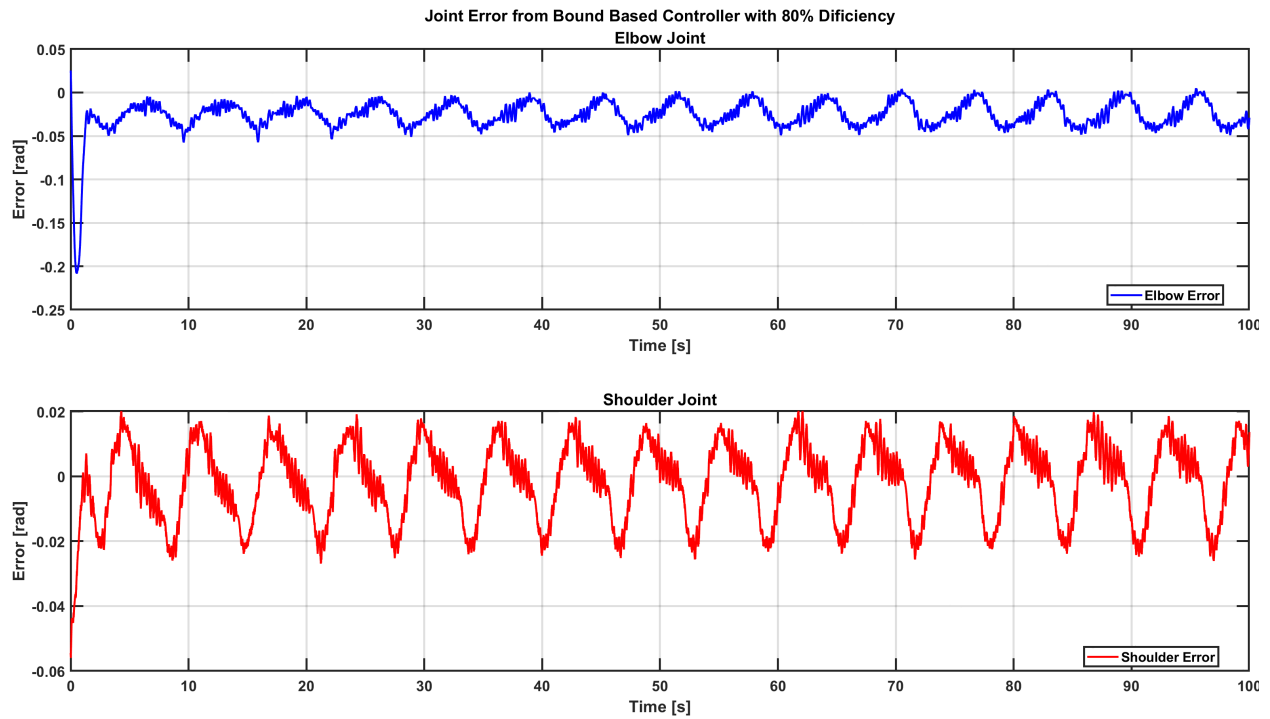
Figure 5.29 Error via BAC with actuator deficiency (80%).
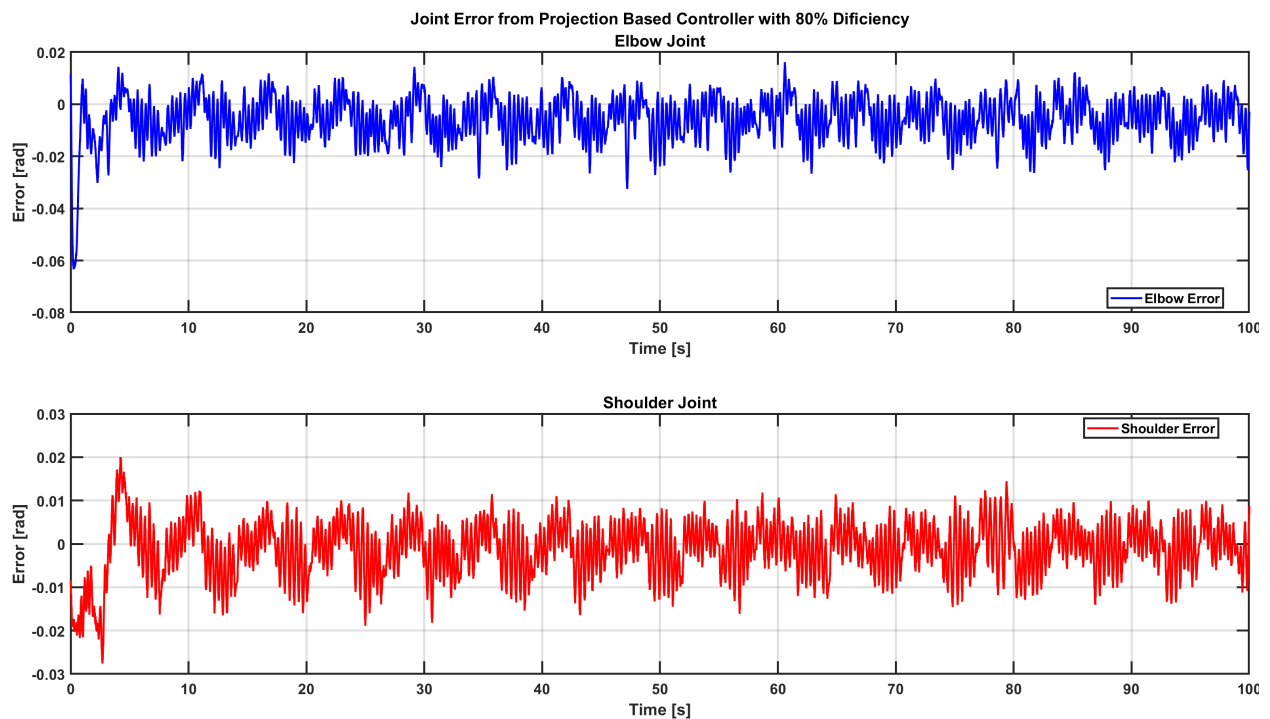
Figure 5.30 Error via PAC with actuator deficiency (60%).

58

5.1.4 Joint Torques

In this section, the analysis of the experimental outcomes for control input, denoted as commanded torque, across all test scenarios is presented. This includes data from both the bound-based and projection operator-based controllers. The related figures are organized in an ascending sequence based on deficiency level. The data from this section is further scrutinized in Section 5.2.5, where the distinctions between the two controllers become more evident.

Beginning with the 40% overdrive scenario. Figures 5.31 and 5.32 offer a comparison of the joint torques of the bound-based and projection operator-based controllers. This is followed by the 20% deficiency case, where the joint torques of both controllers are depicted in Figures 5.33 and 5.34. Next, the 40% deficiency case, with Figures 5.35 and 5.36 showcasing the joint torques for both controller types is explored. The results then move to the 60% deficiency case, where Figures 5.37 and 5.38 capture the joint torques results of the bound-based and projection operator-based controllers. Finally, Figures 5.39 and 5.40 provide the performance outcomes at an 80% actuator deficiency of the joint torques for both the bound-based and projection operator-based controllers.

The control gains were set to $K_r = diag(40, 60)$, $k_n = 1$, and $\mu = 3I_2$ and the desired trajectory was the shoulder joint oscillating 10 degrees and the elbow joint oscillating 15 degrees with a period of about 6.25 seconds. The bounds are the same for both controllers but were set differently for different actuator deficiencies. For the 40% overdrive case, the upper and lower bounds are $\hat{\delta}_{\lambda_{max}} = 0.6$, $\hat{\delta}_{\lambda_{min}} = 0.2$, respectively. For the deficiency cases, the lower bound was always set to $\hat{\delta}_{\lambda_{min}} = -0.9$; however the lower bound changes as the deficiency increases. Specifically, at 20% deficiency $\hat{\delta}_{\lambda_{min}} = -0.1$, at 40% deficiency $\hat{\delta}_{\lambda_{min}} = -0.2$, and at 60% and 80% deficiencies $\hat{\delta}_{\lambda_{min}} = -0.4$. Finally, the initial conditions were set to be inside the bounds; therefore $\hat{\delta}_{\lambda_0} = 0.5$ for the 40% overdrive case and $\hat{\delta}_{\lambda_0} = -0.5$ for all deficiency cases.

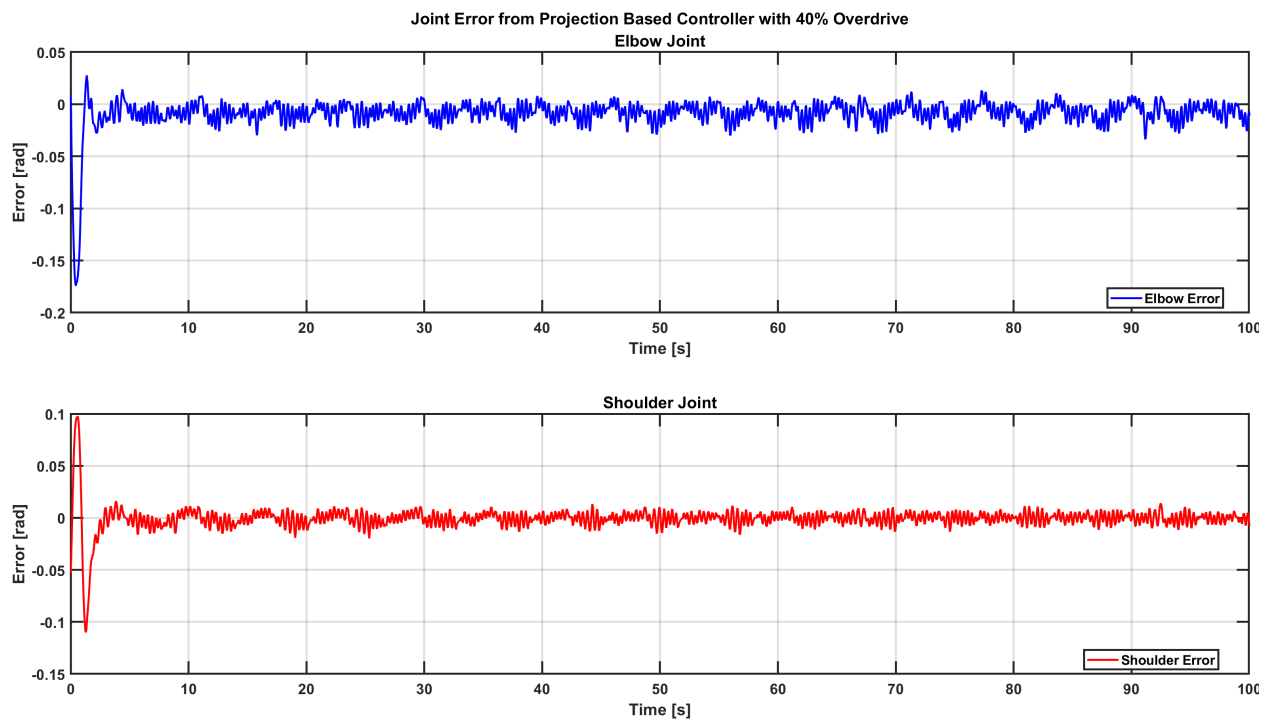*Figure 5.31* Toques via BAC with over actuation (40%).

Figure 5.32 Toques via PAC with over actuation (40%).
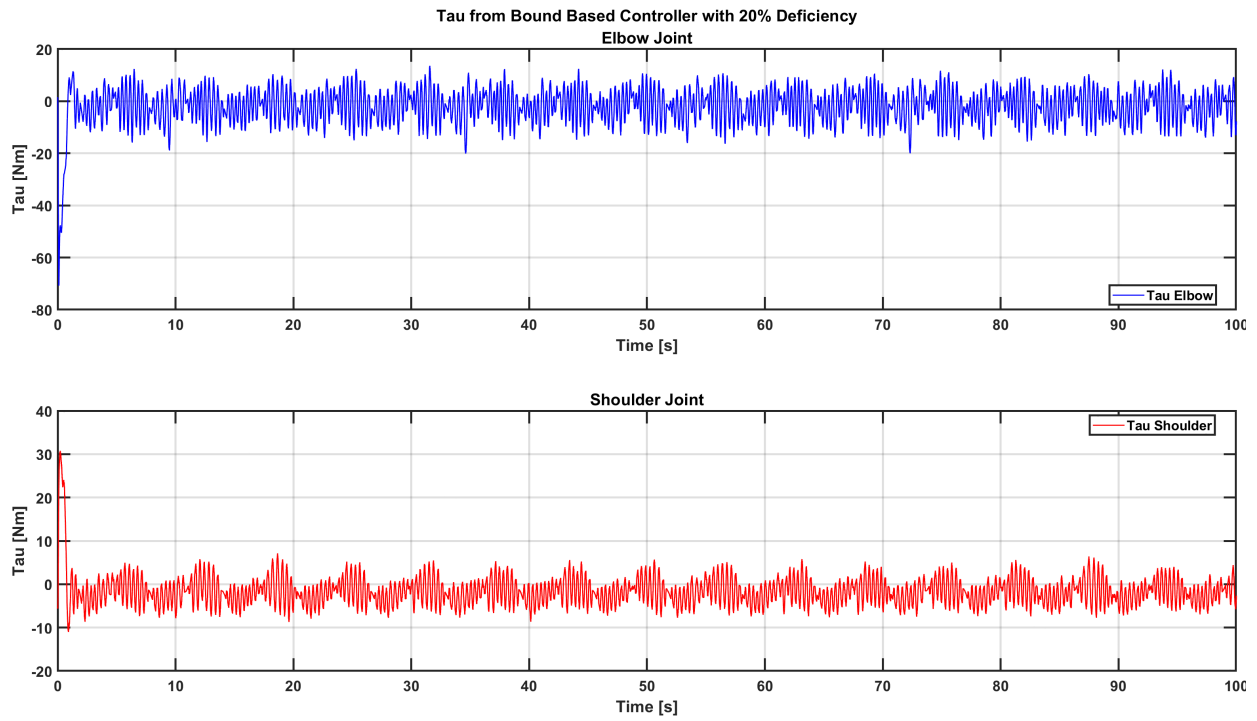
Figure 5.33 Toques via BAC with actuator deficiency (20%).
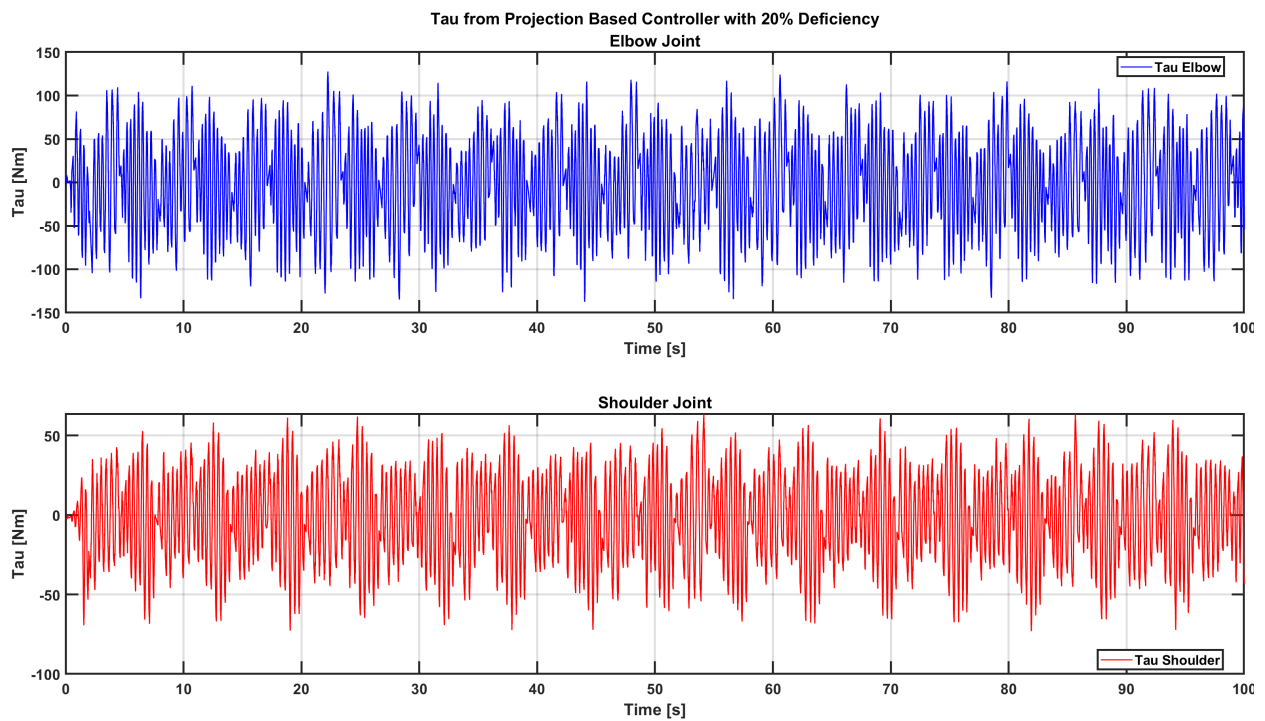
Figure 5.34 Toques via PAC with actuator deficiency (20%).
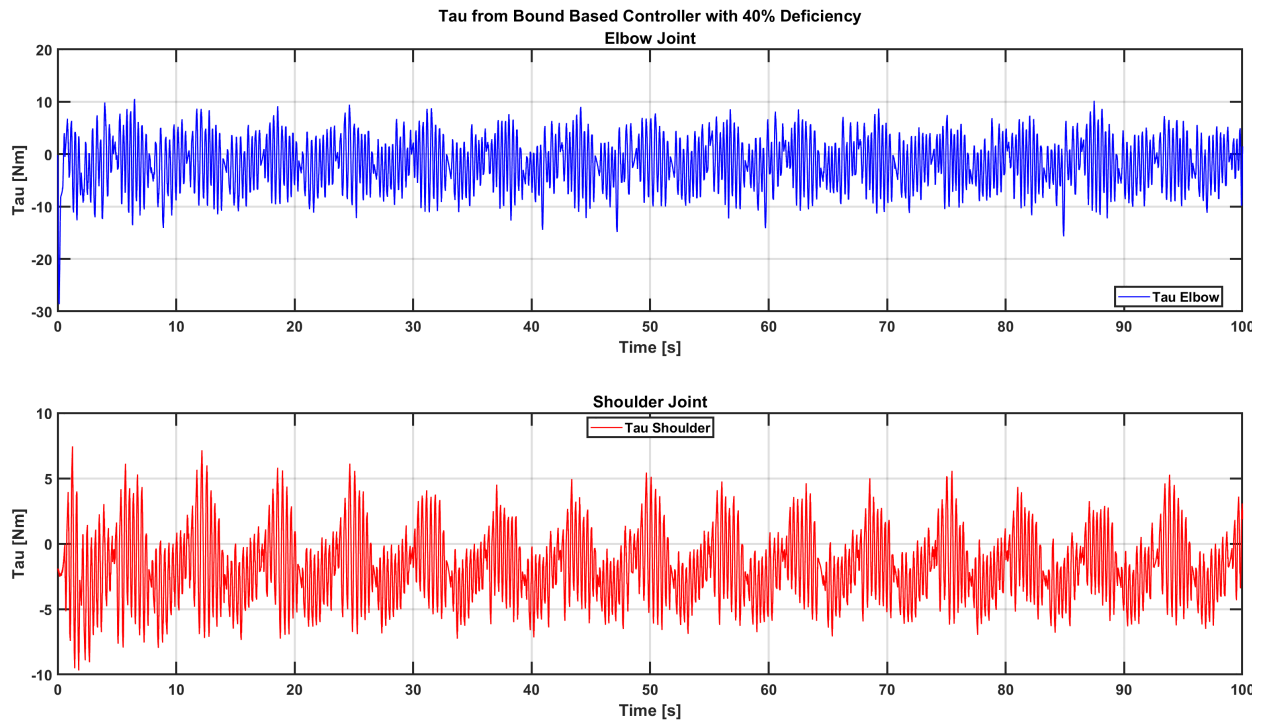
Figure 5.35 Toques via BAC with actuator deficiency (40%).
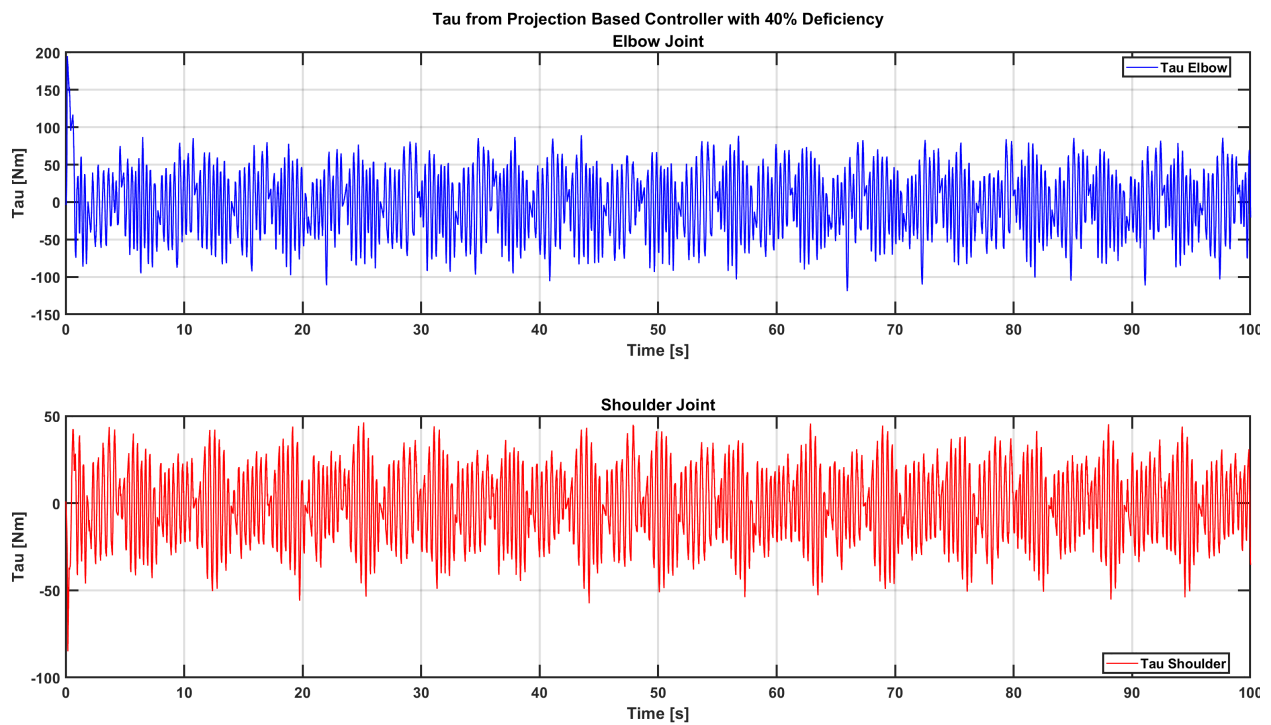
Figure 5.36 Toques via PAC with actuator deficiency (40%).
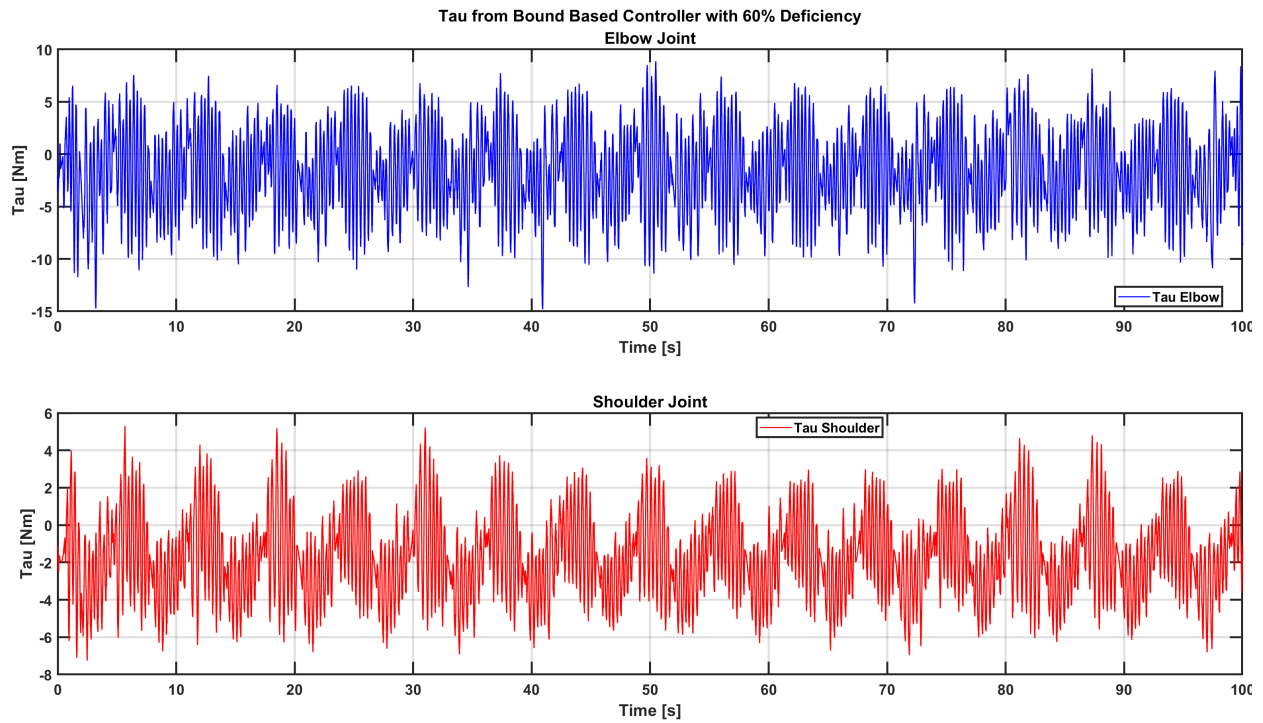
Figure 5.37 Toques via BAC with actuator deficiency (60%).
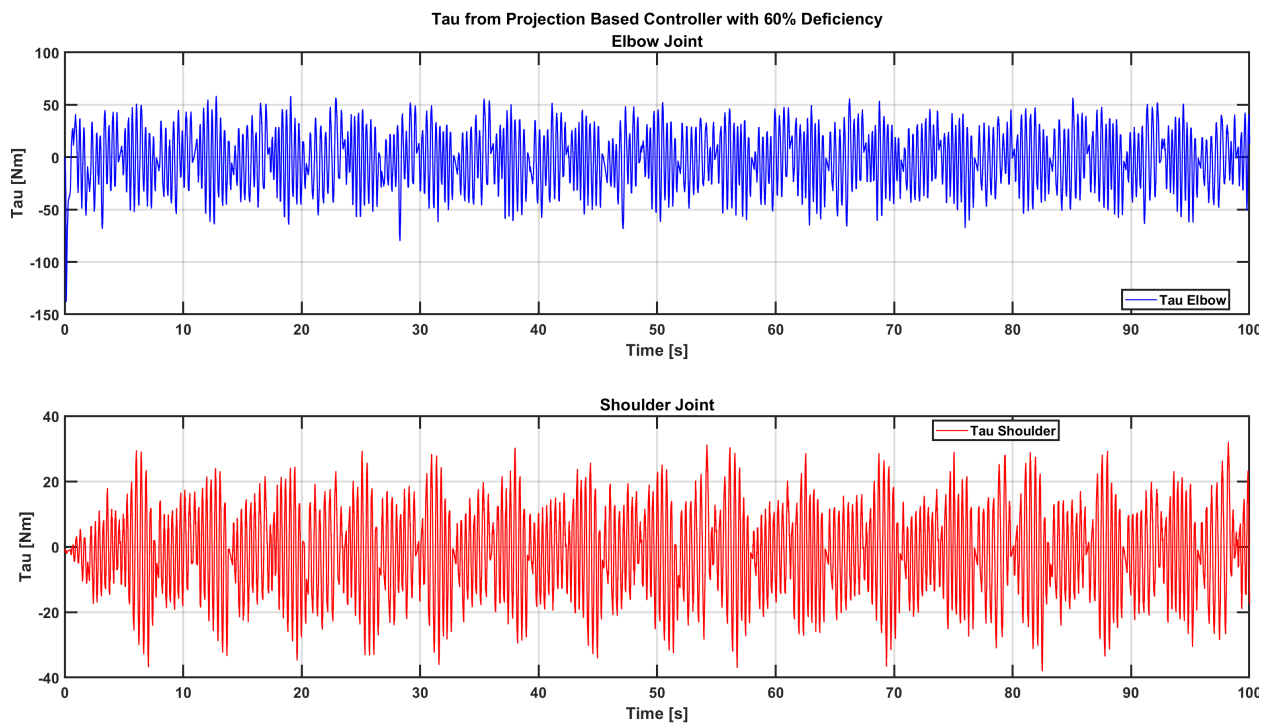
Figure 5.38 Toques via PAC with actuator deficiency (60%).

63
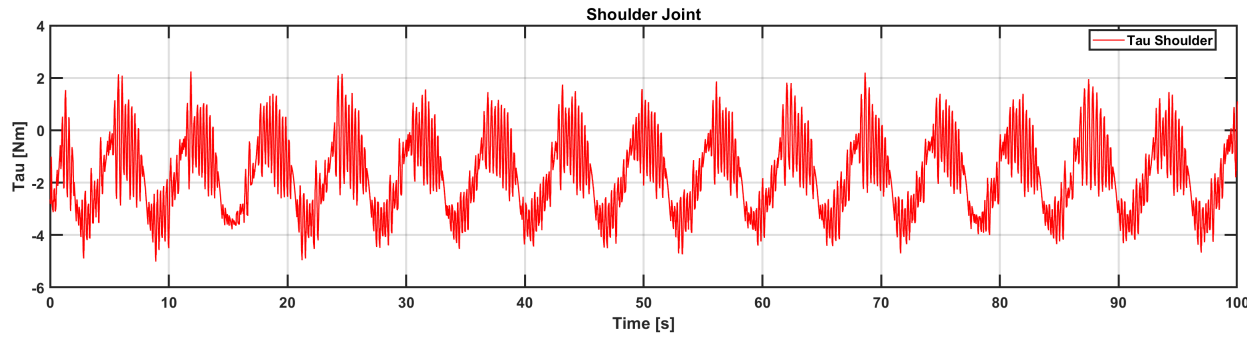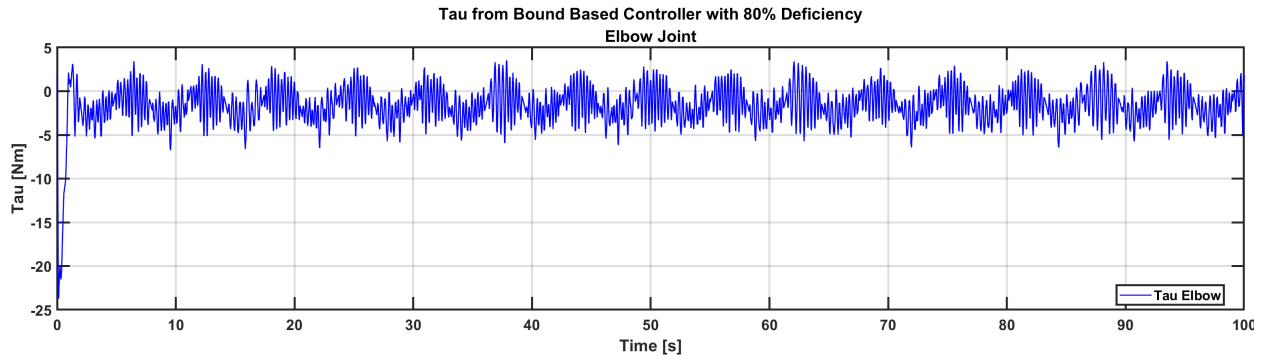
Figure 5.39 Toques via BAC with actuator deficiency (80%).
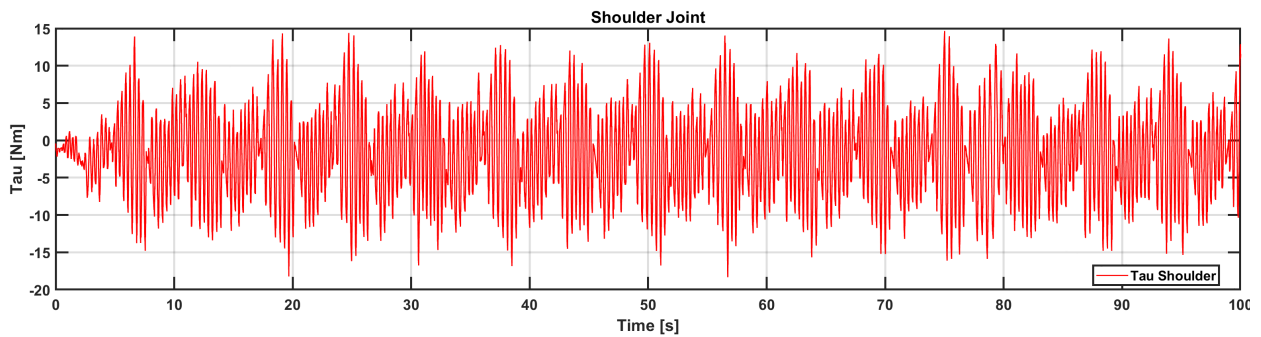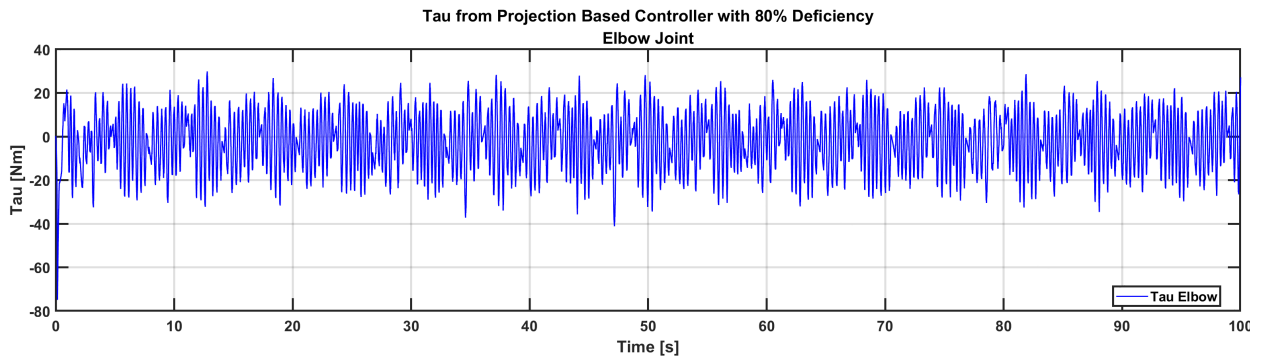
Figure 5.40 Toques via PAC with actuator deficiency (80%).

5.1.5 Estimated Actuator Deficiencies

This section delivers an in-depth analysis of the experimental outcomes for the estimated actuator deficiencies, represented as $\hat{\delta}$, across all scenarios. The data encompasses results from both the bound-based and projection operator-based controllers. The related figures are sequenced in ascending order of deficiency level. These results are further dissected in Section 5.2.6.

The analysis commences with the 40% overdrive scenario. Figures 5.41 and 5.42 provide a comparative study of the estimated actuator deficiencies of the bound-based and projection operator-based controllers. This is succeeded by the 20% deficiency case, where the estimated actuator deficiencies of both controllers are illustrated in Figures 5.43 and 5.44. The exploration continues with the 40% deficiency case, where Figures 5.45 and 5.46 display the estimated actuator deficiencies results for both controller types. The 60% deficiency case is then discussed, with Figures 5.47 and 5.48 capturing the estimated actuator deficiencies outcomes of the bound-based and projection operator-based controllers. Lastly, for the 80% deficiency case, Figures 5.49 and 5.50 estimated actuator deficiencies results for both the bound-based and projection operator-based controllers respectively.

The control gains were set to $K_r = diag(40,60)$, $k_n = 1$, and $\mu = 3I_2$ and the desired trajectory was the shoulder joint oscillating 10 degrees and the elbow joint oscillating 15 degrees with a period of about 6.25 seconds. The bounds are the same for both controllers but were set differently for different actuator deficiencies. For the 40% overdrive case, the upper and lower bounds are $\hat{\delta}_{\lambda_{max}} = 0.6$, $\hat{\delta}_{\lambda_{min}} = 0.2$, respectively. For the deficiency cases, the lower bound was always set to $\hat{\delta}_{\lambda_{min}} = -0.9$; however the lower bound changes as the deficiency increases. Specifically, at 20% deficiency $\hat{\delta}_{\lambda_{min}} = -0.1$, at 40% deficiency $\hat{\delta}_{\lambda_{min}} = -0.2$, and at 60% and 80% deficiencies $\hat{\delta}_{\lambda_{min}} = -0.4$. Finally, the initial conditions were set to be inside the bounds; therefore $\hat{\delta}_{\lambda_0} = 0.5$ for the 40% overdrive case and $\hat{\delta}_{\lambda_0} = -0.5$ for all deficiency cases.
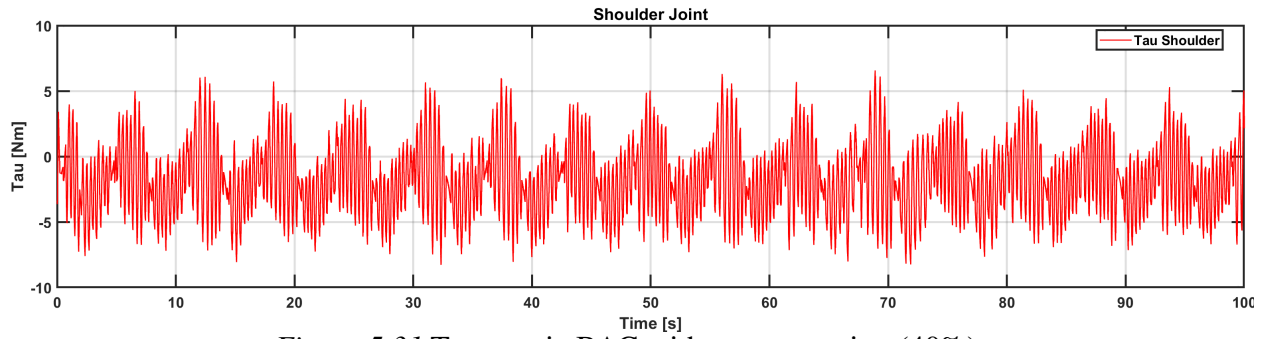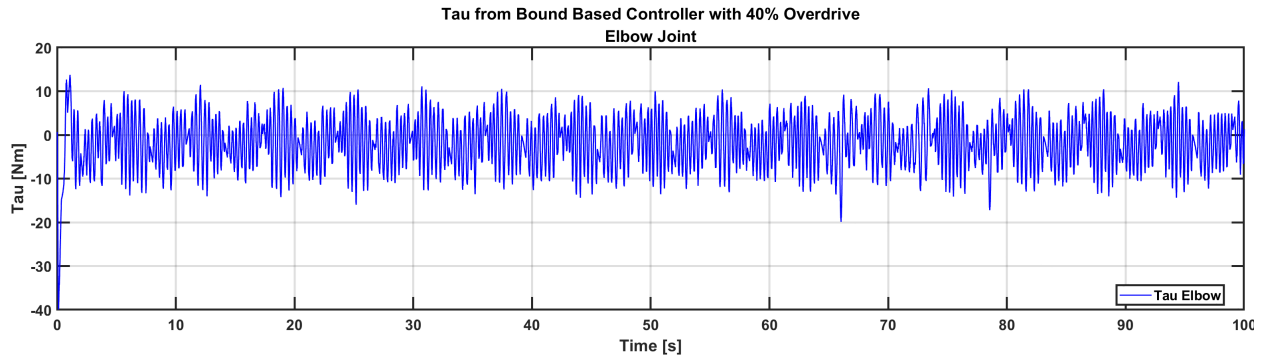
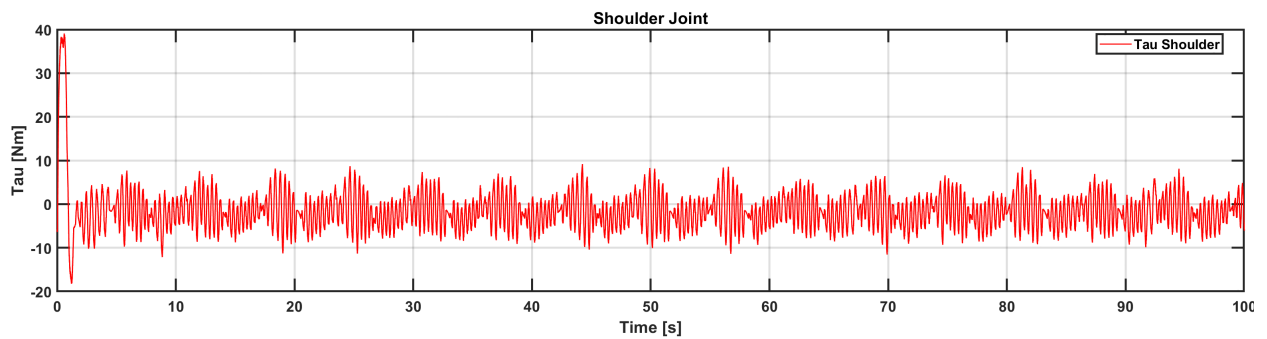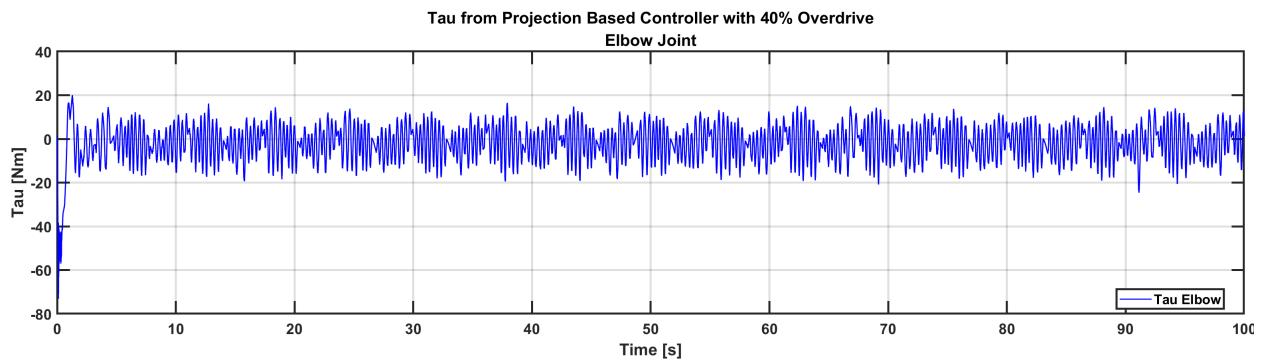*Figure 5.41* Estimated deficiencies via BAC with over actuation (40%).
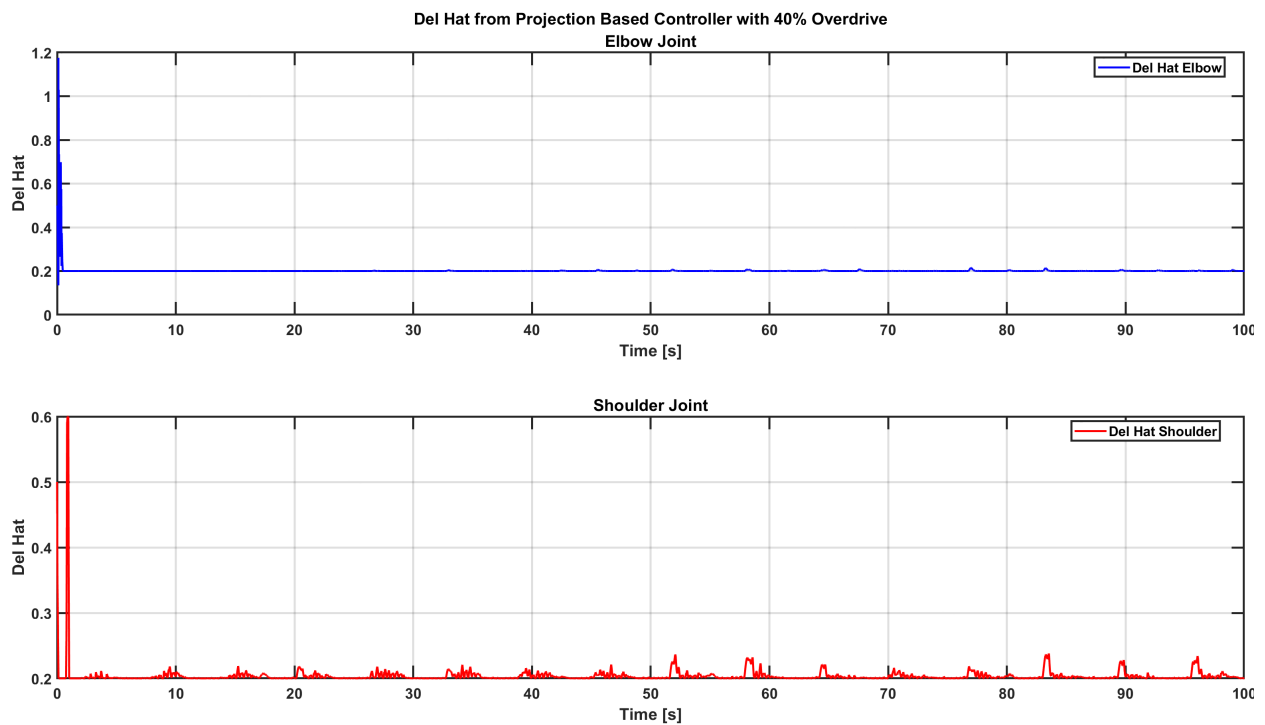
Figure 5.42 Estimated deficiencies via PAC with over actuation (40%).
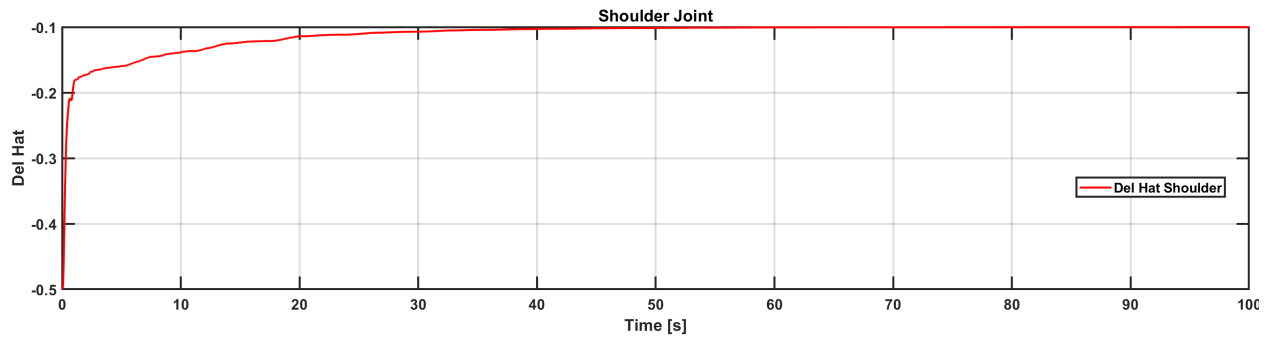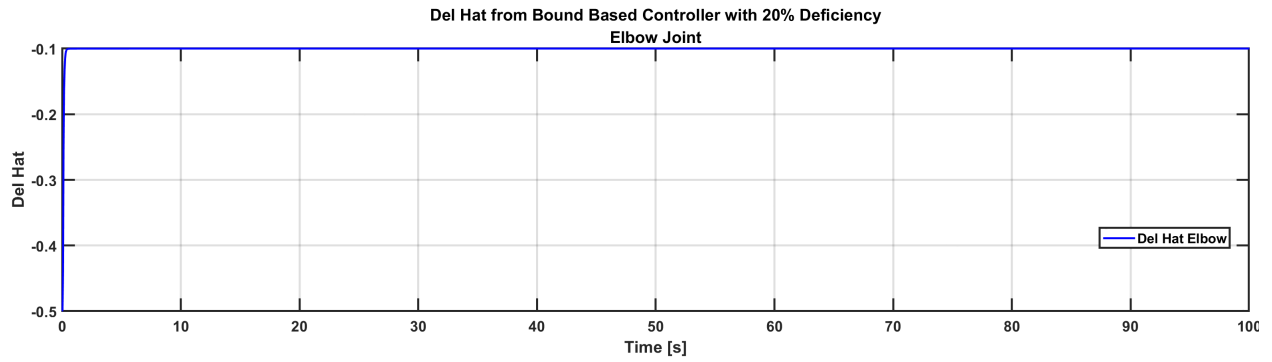
Figure 5.43 Estimated deficiencies via BAC with actuation deficiency (20%).
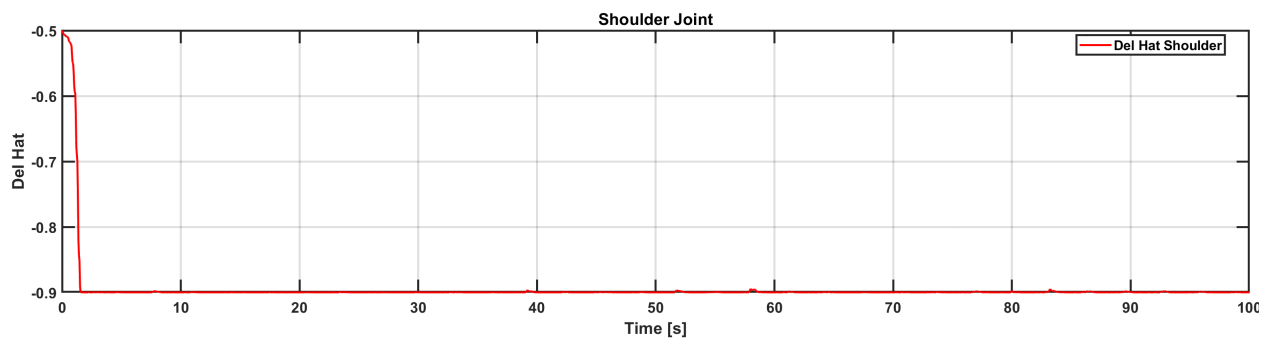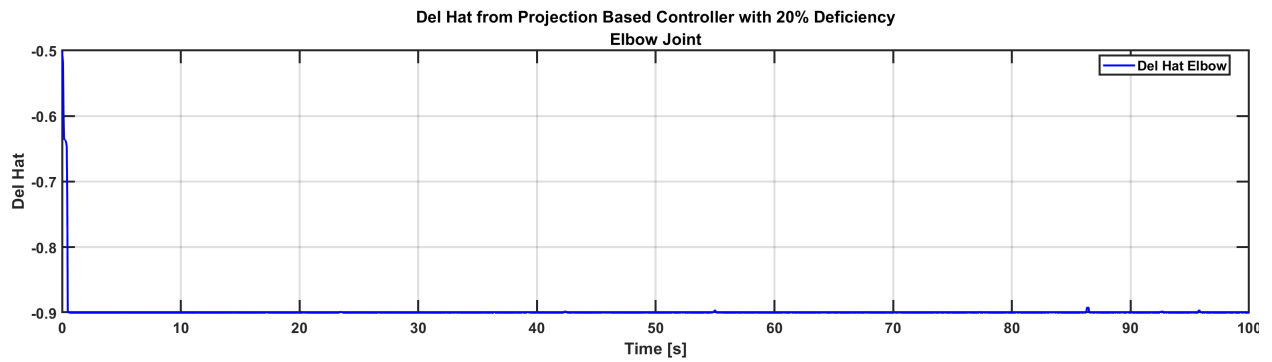
Figure 5.44 Estimated deficiencies via PAC with actuation deficiency (20%).
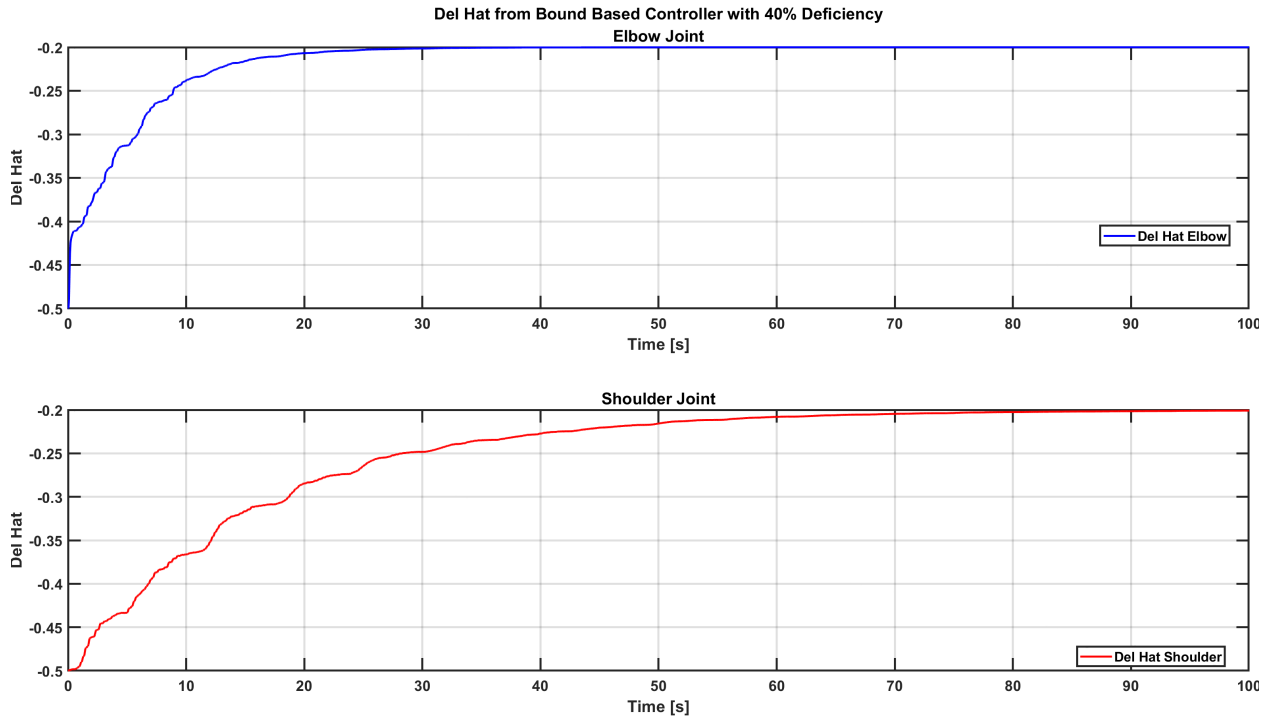
Figure 5.45 Estimated deficiencies via BAC with actuation deficiency (40%).
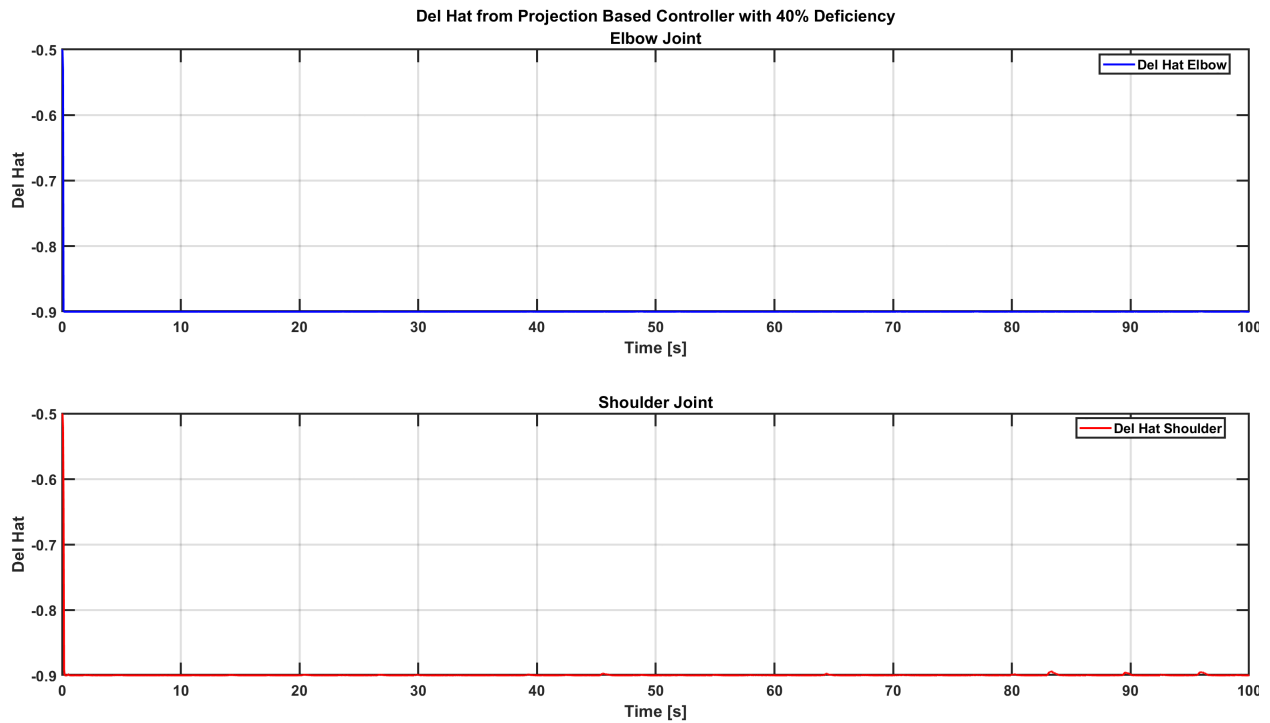
Figure 5.46 Estimated deficiencies via PAC with actuation deficiency (40%).
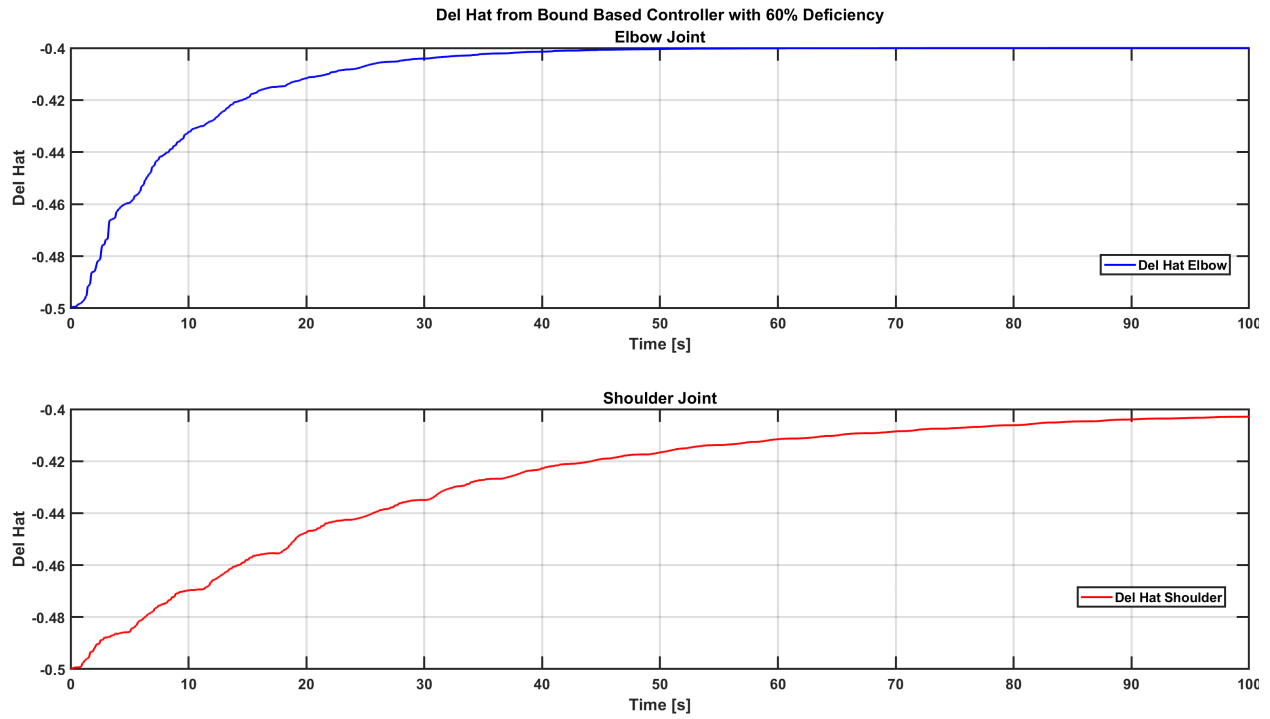
Figure 5.47 Estimated deficiencies via BAC with actuation deficiency (60%).
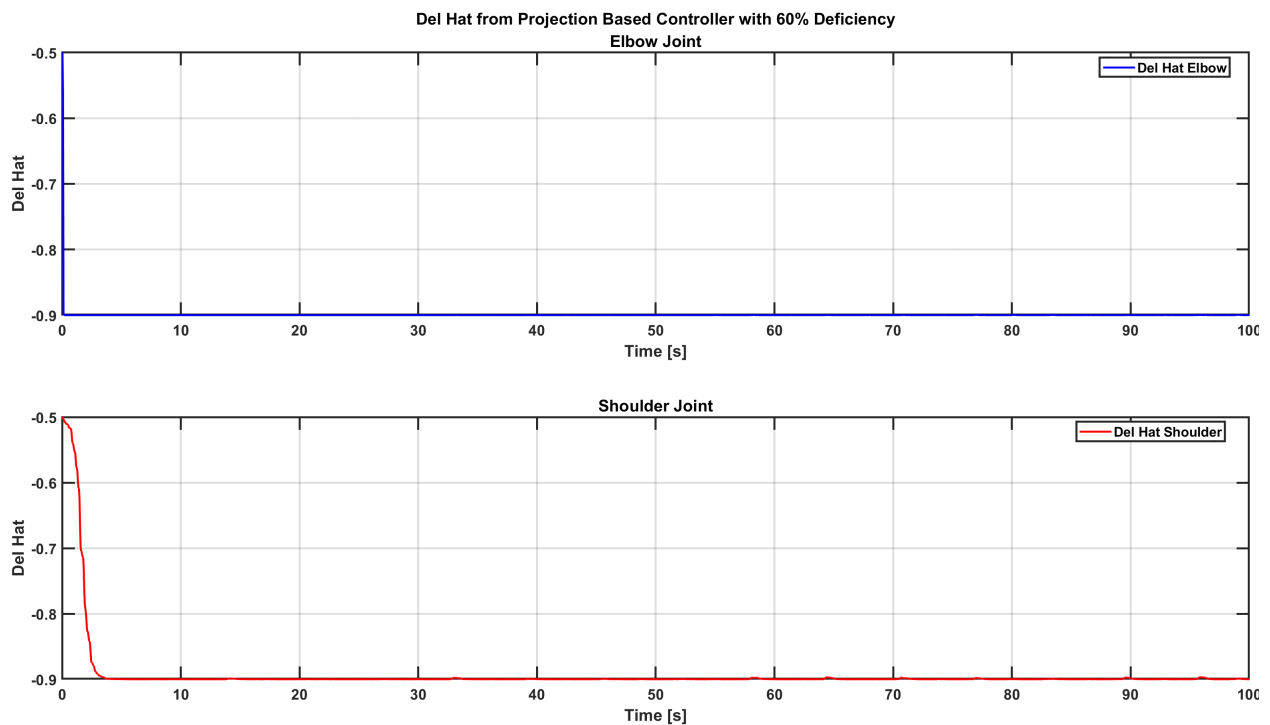
Figure 5.48 Estimated deficiencies via PAC with actuation deficiency (60%).

69
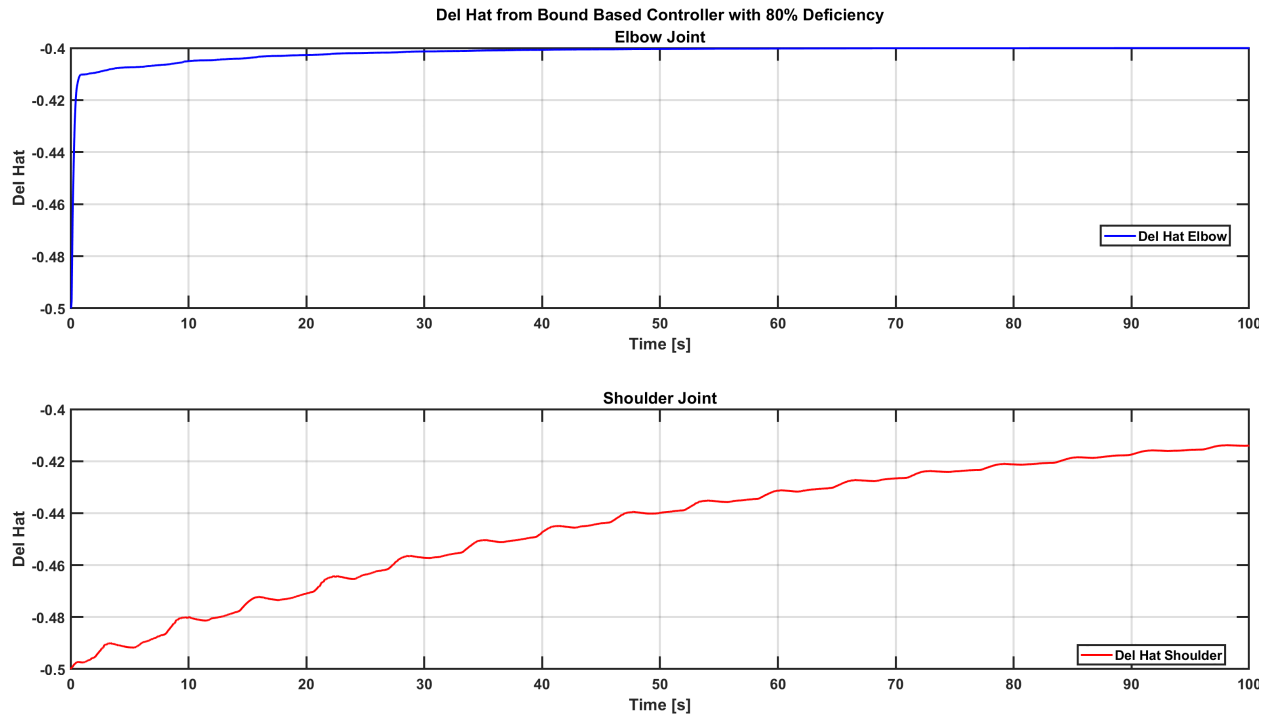
Figure 5.49 Estimated deficiencies via BAC with actuation deficiency (80%).
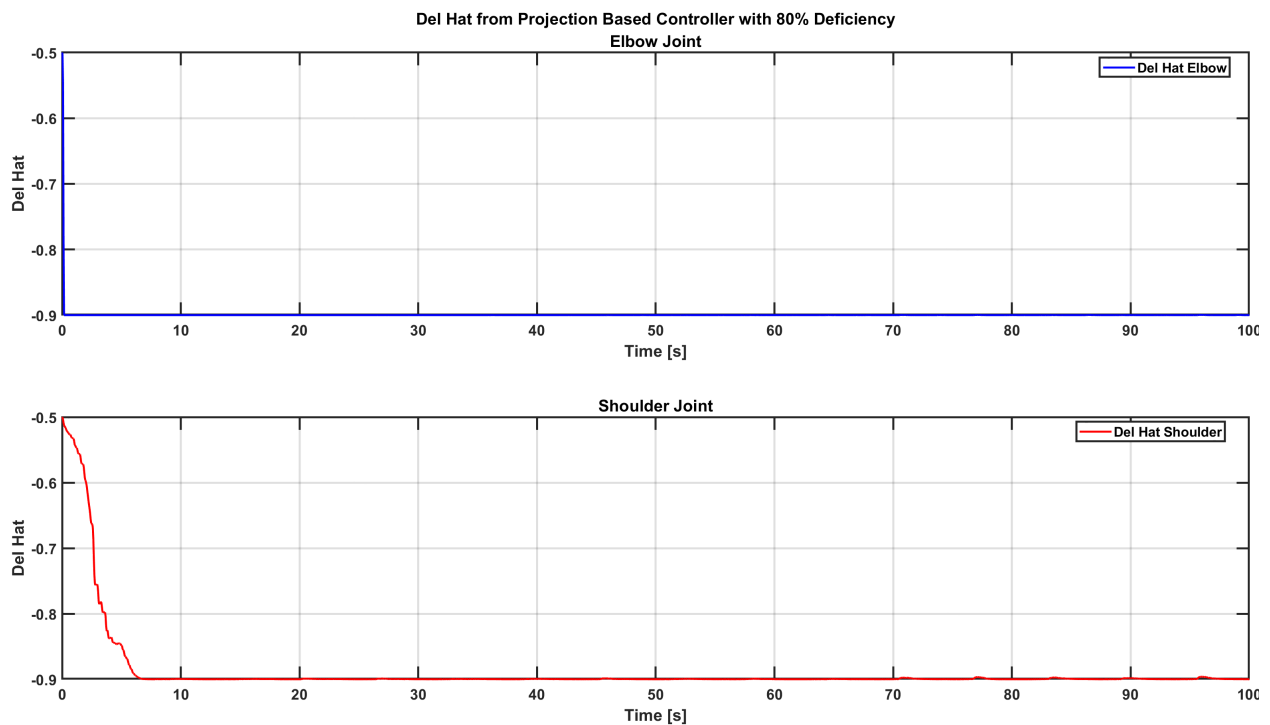
Figure 5.50 Estimated deficiencies via PAC with actuation deficiency (80%).

5.1.6 Estimated Model Parameters

This section carefully presents the experimental results of estimated model parameters, denoted as $\hat{\phi}$, for all cases using two distinct controllers: the bound-based controller and the projection operator-based controller. The figures are systematically arranged in an order of increasing deficiency level, ensuring a logical progression in the data presentation. The results of this section are analyzed in Section 5.2.7 where important conclusions are drawn.

Starting with the 40% overdrive case, Figures 5.51 and 5.52 provide a comparative analysis of the estimated model parameters of the bound-based and projection operator-based controllers respectively. Moving on to deficiency cases, the 20% deficiency case, Figures 5.53 and 5.54 respectively represent the estimated model parameters of the bound-based and projection operator-based controllers. The 40% deficiency case follows next, with Figures 5.55 and 5.56 respectively illustrating the estimated model parameters results for the bound-based and projection operator-based controllers. The 60% deficiency case is then explored where Figures 5.57 and 5.58 respectively depict the estimated model parameters outcomes for the bound-based and projection operator-based controllers. Finally, the most challenging scenario, the 80% deficiency case, is presented. Figures 5.59 and 5.60 respectively show the estimated model parameters results for both controllers.

The control gains were set to $K_r = diag(40, 60)$, $k_n = 1$, and $\mu = 3I_2$ and the desired trajectory was the shoulder joint oscillating 10 degrees and the elbow joint oscillating 15 degrees with a period of about 6.25 seconds. The bounds are the same for both controllers but were set differently for different actuator deficiencies. For the 40% overdrive case, the upper and lower bounds are $\hat{\delta}_{\lambda_{max}} = 0.6$, $\hat{\delta}_{\lambda_{min}} = 0.2$, respectively. For the deficiency cases, the lower bound was always set to $\hat{\delta}_{\lambda_{min}} = -0.9$; however the lower bound changes as the deficiency increases. Specifically, at 20% deficiency $\hat{\delta}_{\lambda_{min}} = -0.1$, at 40% deficiency $\hat{\delta}_{\lambda_{min}} = -0.2$, and at 60% and 80% deficiencies $\hat{\delta}_{\lambda_{min}} = -0.4$. Finally, the initial conditions were set to be inside the bounds; therefore $\hat{\delta}_{\lambda_0} = 0.5$ for the 40% overdrive case and $\hat{\delta}_{\lambda_0} = -0.5$ for all deficiency cases.
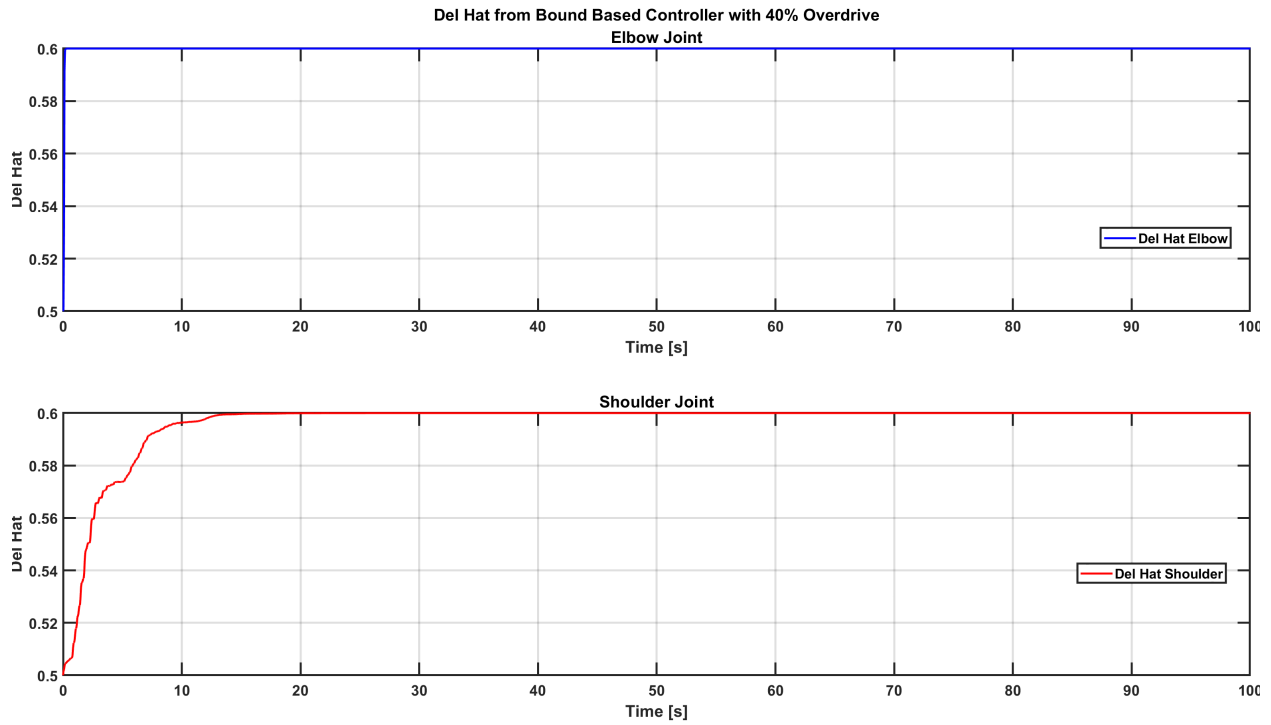
*Figure 5.51* Estimated model parameters via BAC with over actuation (40%).
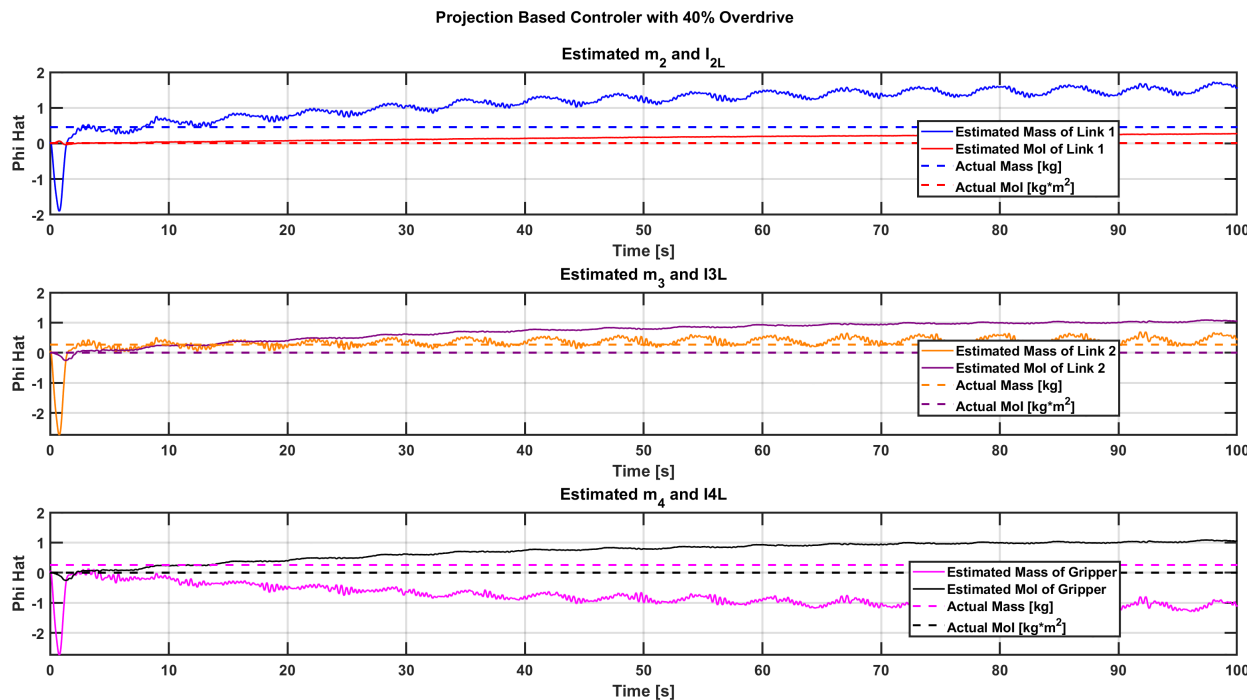
Figure 5.52 Estimated model parameters via PAC with over actuation (40%).
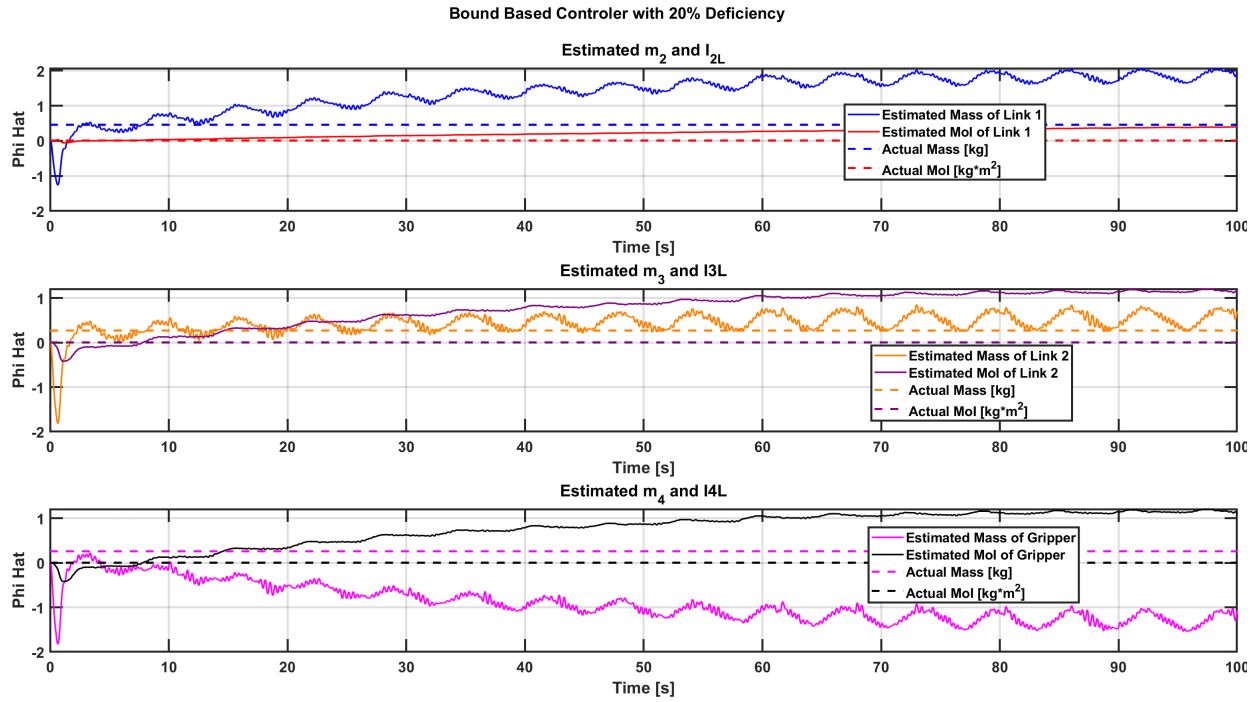
Figure 5.53 Estimated model parameters via BAC with actuation deficiency (20%).
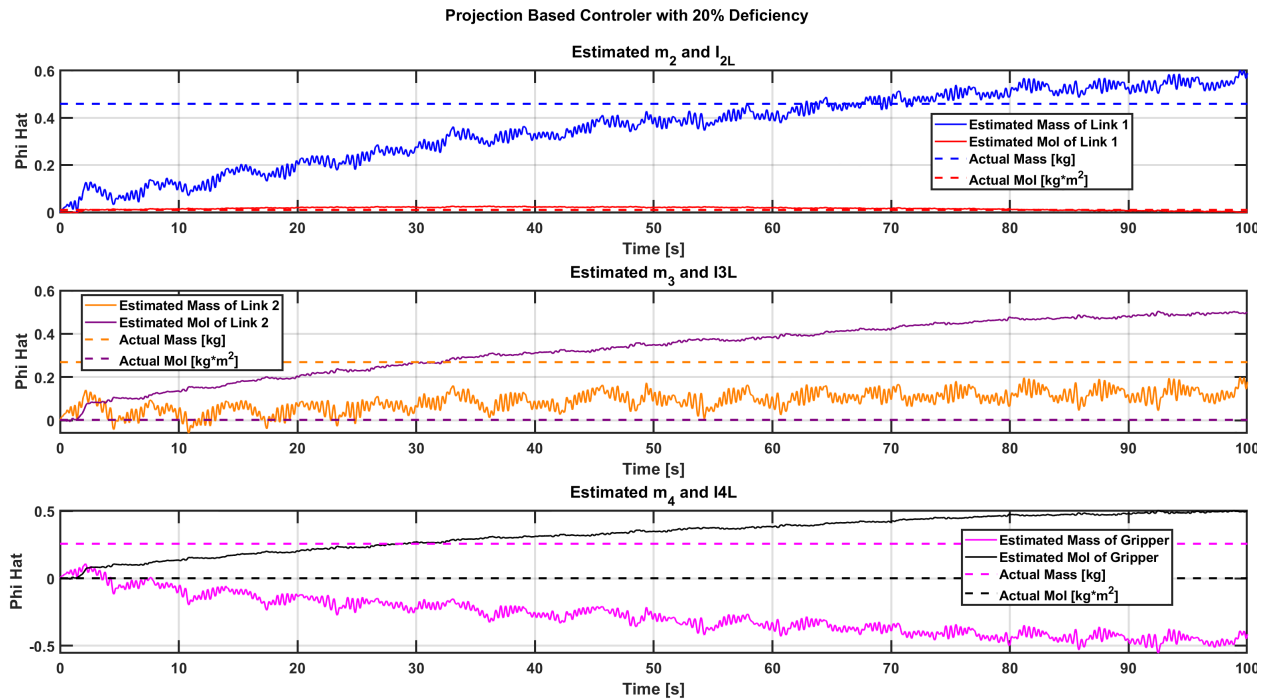
Figure 5.54 Estimated model parameters via PAC with actuation deficiency (20%).
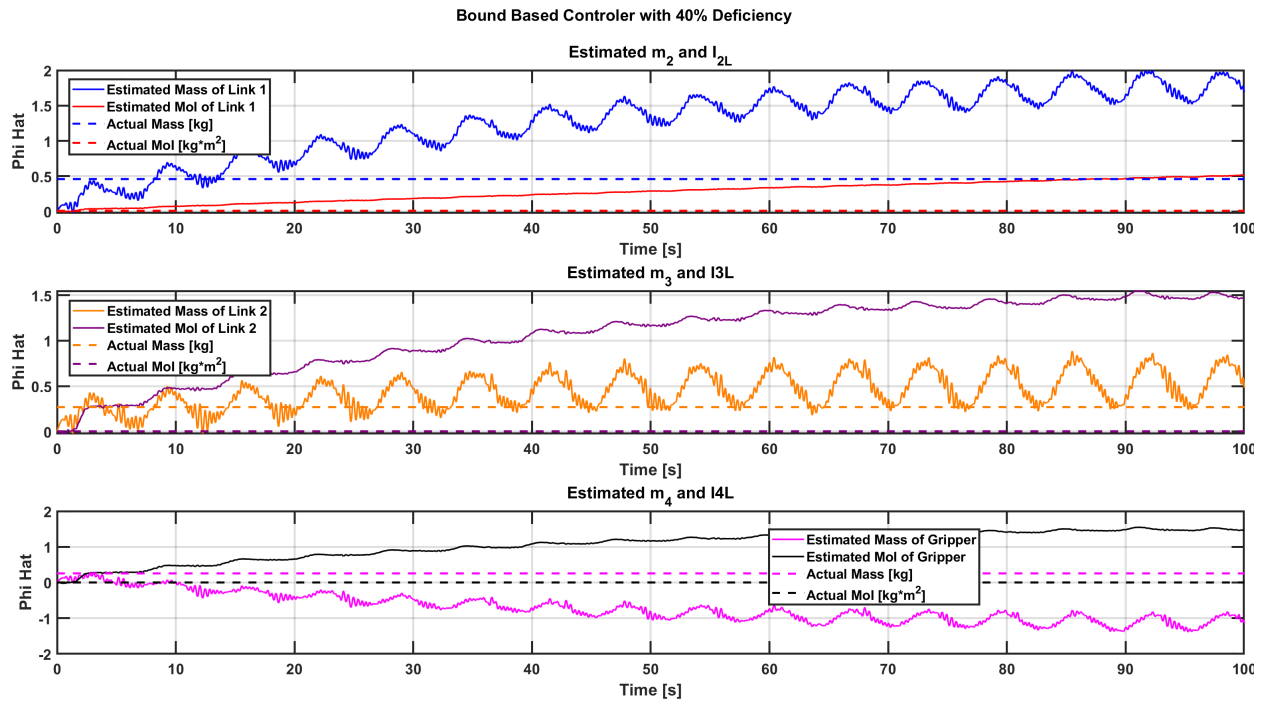
Figure 5.55 Estimated model parameters via BAC with actuation deficiency (40%).
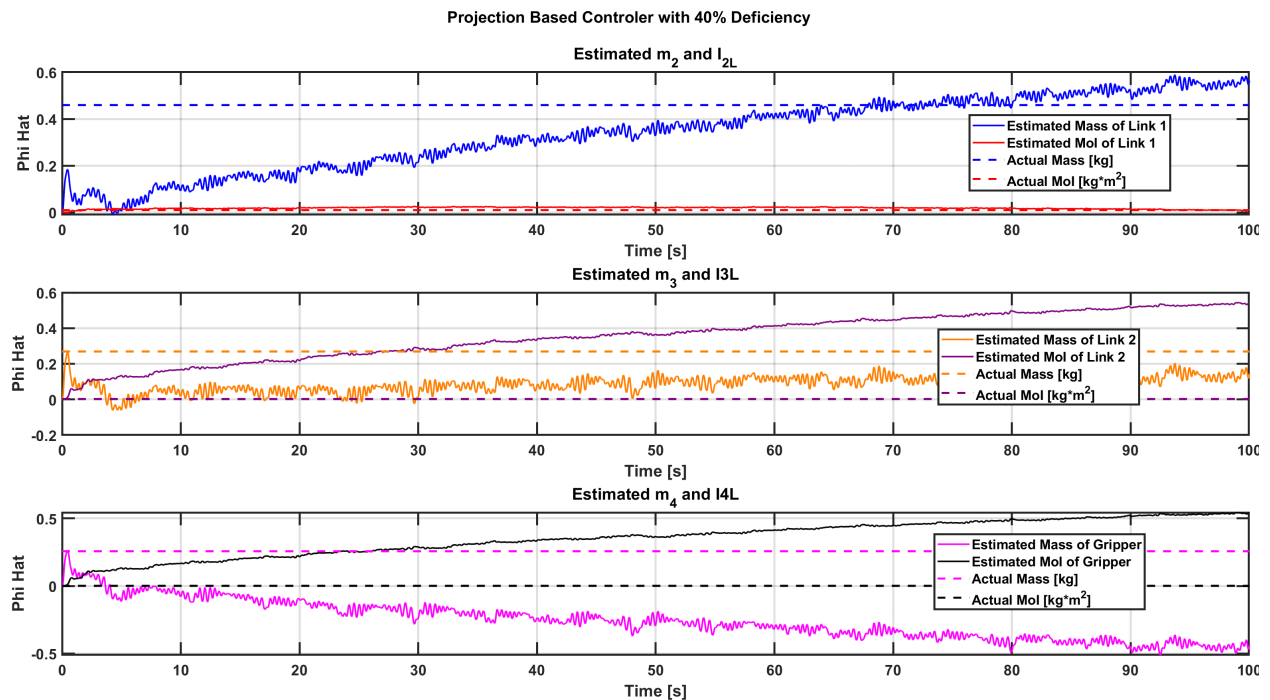
Figure 5.56 Estimated model parameters via PAC with actuation deficiency (40%).
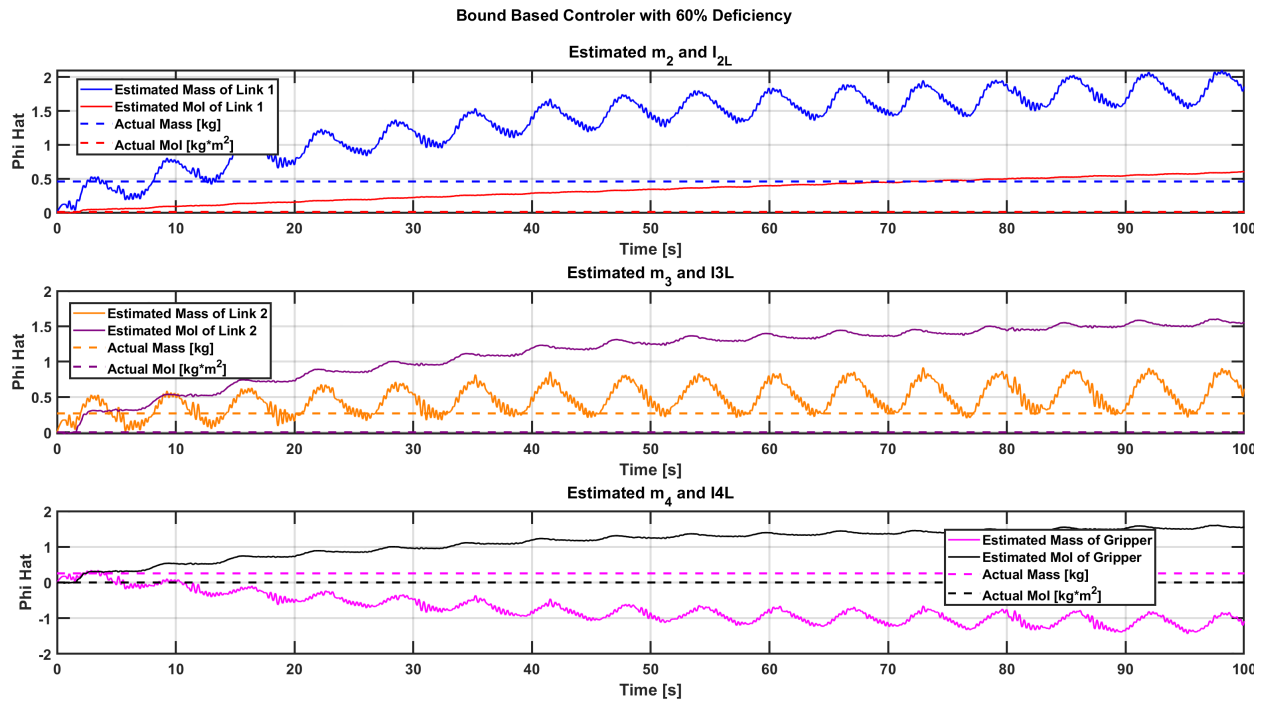
Figure 5.57 Estimated model parameters via BAC with actuation deficiency (60%).
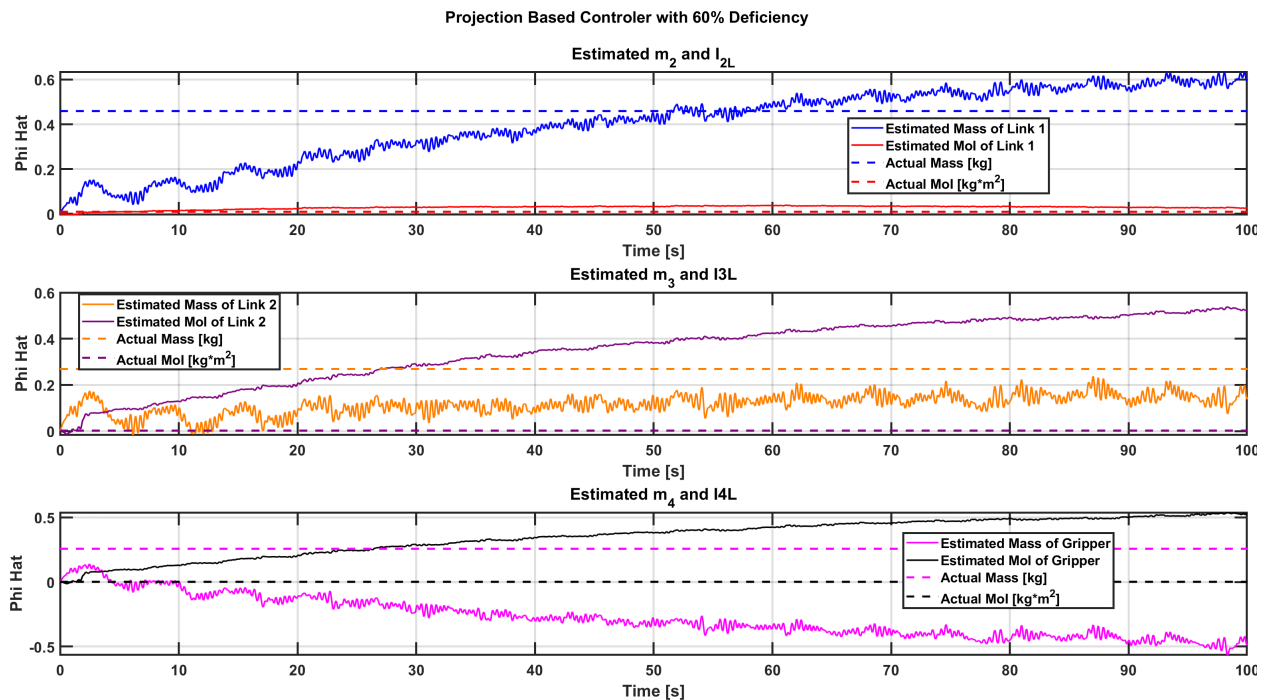
Figure 5.58 Estimated model parameters via PAC with actuation deficiency (60%).
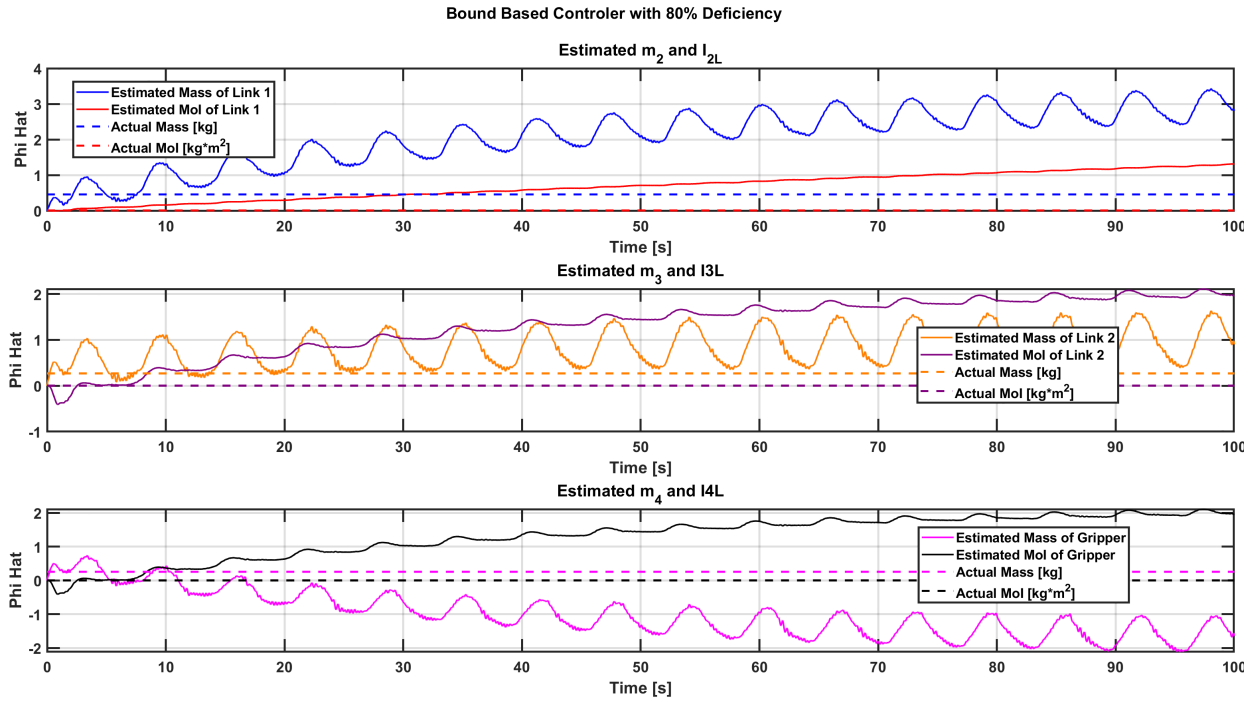
Figure 5.59 Estimated model parameters via BAC with actuation deficiency (80%).
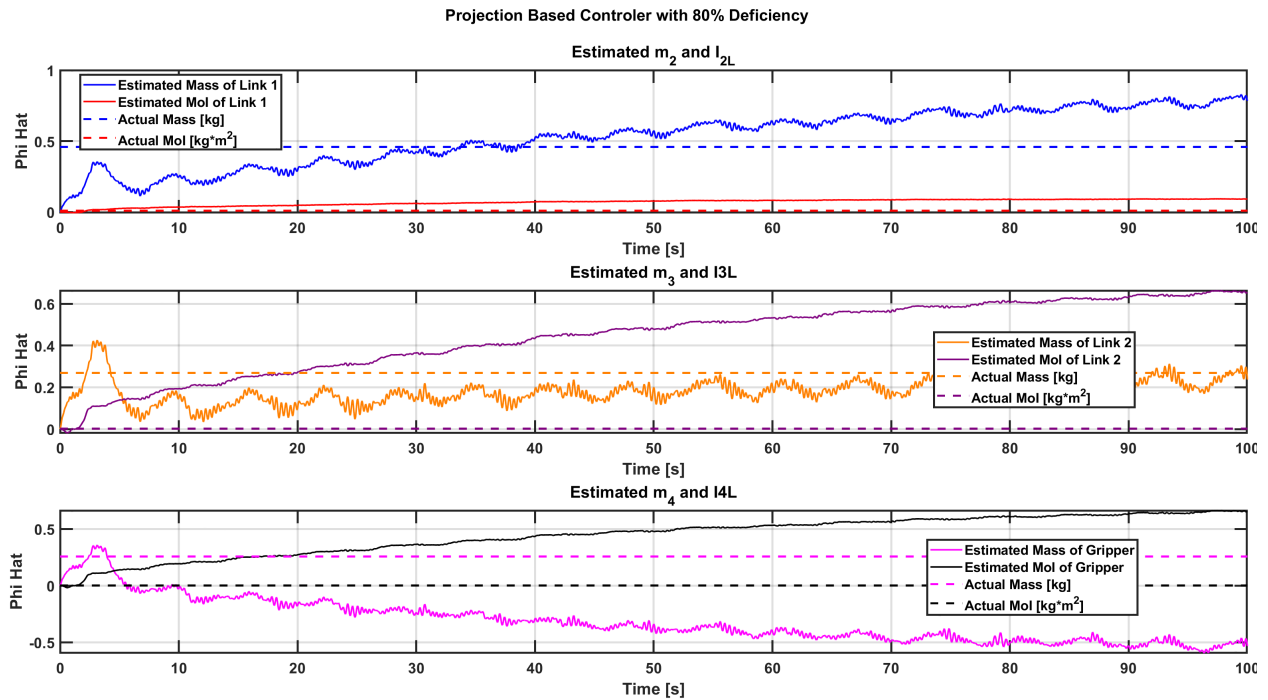
Figure 5.60 Estimated model parameters via PAC with actuation deficiency (80%).

5.2 Discussion

In the following discussion, a detailed analysis of the data obtained from the various experiments with robotic manipulators will be given. According to the results, various patterns are explored, and trends are observed in the estimated model parameters and actuator deficiencies. The discussion also touches upon the performance of the different adaptive controllers under varying conditions. Note that for the results below, subscript 1 corresponds to the shoulder joint and subscript 2 corresponds to the elbow joint.

5.2.1 Performance Measurements

Table 5.1 Performance measurements comparing the adaptive controllers (40% overdrive).

40% Overdrive	Standard	Bound-based	Projection-based
$\int_0^{t_{\text{final}}} \left|e_1(t)\right|^2 \, \mathrm{dt}$	0.2398	0.1800	0.2921
$\int_0^{t_{\text{final}}} \left|e_2(t)\right|^2 \, \mathrm{dt}$	0.6679	1.1833	0.9496
$\int_0^{t_{\text{final}}} \left|\tau_1(t)\right|^2 \, \mathrm{dt}$	1.755×10^5	7.237×10^4	1.311×10^5
$\int_0^{t_{\text{final}}} \left|\tau_2(t)\right|^2 \, \mathrm{dt}$	5.847×10^5	4.357×10^5	2.278×10^5

The performance of different adaptive controllers under a condition of 40% overdrive is given in Table 5.1. Several key findings emerged. The bound-based controller demonstrated superior performance for the shoulder joint, achieving the lowest integral of the square of the norm of the error (0.1800) and the commanded torque (7.237×10^4). This suggests that the bound-based controller is particularly effective in minimizing both error and torque for the shoulder joint under conditions of overdrive.

However, the performance dynamics changed for the elbow joint. Here, the standard controller was most effective in minimizing the error (0.6679), while the projection-based controller was most successful in reducing the commanded torque (2.278×10^5). This indicates that the choice of controller may depend on the specific joint and whether the priority is to minimize error or to minimize torque. Also, when the total error is compared, the standard adaptive controller shows better performance than the projection-based controller and the projection-based controller shows better performance than the bound-based approach in the 40% overdrive case.

The performance of different adaptive controllers under a condition of 20% deficiency is given

Table 5.2 Performance measurements comparing the adaptive controllers (20% deficiency).

20% Deficiency	Standard	Bound-based	Projection-based
$\int_0^{t_{\text{final}}} \lvert e_1(t) \rvert^2 \, dt$	0.3160	0.2602	0.4554
$\int_0^{t_{\text{final}}} \lvert e_2(t) \rvert^2 \, dt$	1.2379	1.4588	0.5494
$\int_0^{t_{\text{final}}} \lvert \tau_1(t) \rvert^2 \, dt$	5.794×10^4	8.567×10^4	5.257×10^6
$\int_0^{t_{\text{final}}} \lvert \tau_2(t) \rvert^2 \, dt$	1.736×10^5	2.816×10^5	1.997×10^7

in Table 5.2, where the commanded torque is multiplied by a factor of 0.8. The bound-based controller demonstrated superior performance for the shoulder joint, achieving the lowest integral of the square of the norm of the error (0.2602). However, it had the highest error for the elbow joint (1.4588). This suggests that the bound-based controller is particularly effective in minimizing error for the shoulder joint under conditions of low deficiency, but not for the elbow joint. Also, when the total error is compared, the projection-based controller shows better performance than the bound-based controller and the bound-based controller shows better performance than the standard adaptive controller in a 20% deficiency case.

On the other hand, the standard controller was most effective in minimizing the commanded torque for the shoulder joint (5.794×10^4), while the projection-based controller had the highest torque (5.257×10^6). For the elbow joint, the standard controller also had the smallest commanded torque (1.736×10^5), and the projection-based controller had the highest torque (1.997×10^7).

Table 5.3 Performance measurements comparing the adaptive controllers (40% deficiency).

40% Deficiency	Standard	Bound-based	Projection-based
$\int_0^{t_{\text{final}}} \lvert e_1(t) \rvert^2 \, dt$	0.6854	0.1944	0.4127
$\int_0^{t_{\text{final}}} \lvert e_2(t) \rvert^2 \, dt$	2.0288	1.3446	0.6510
$\int_0^{t_{\text{final}}} \lvert \tau_1(t) \rvert^2 \, dt$	4.719×10^4	7.005×10^4	2.938×10^6
$\int_0^{t_{\text{final}}} \lvert \tau_2(t) \rvert^2 \, dt$	8.757×10^4	1.607×10^5	1.222×10^7

In the examination of the performance of different adaptive controllers under a condition of 40% deficiency given in Table 5.3, where the commanded torque is multiplied by a factor of 0.6, several key observations can be made. For the shoulder joint, the bound-based controller has the lowest error (0.1944), followed by the projection-based controller (0.4127), and the standard controller has the highest error (0.6854). However, for the elbow joint, the projection-based controller has the lowest error (0.6510), while the standard controller has the highest error (2.0288). Also, when

the total error is compared, the projection-based controller shows better performance than the bound-based controller and the bound-based controller shows better performance than the standard adaptive controller in a 40% deficiency case.

When it comes to the integral of the square of the norm of the commanded torque, the standard controller has the lowest torque (4.719×10^4) for the shoulder joint, while the projection-based controller has the highest torque (2.938×10^6). Similarly, for the elbow joint, the standard controller also has the smallest commanded torque (8.757×10^4), but the projection-based controller still has the highest torque (1.222×10^7).

Table 5.4 Performance measurements comparing the adaptive controllers (60% deficiency).

60% Deficiency	Standard	Bound-based	Projection-based
$\int_0^{t_{\text{final}}} |e_1(t)|^2 \, dt$	2.0778	0.2179	0.3513
$\int_0^{t_{\text{final}}} |e_2(t)|^2 \, dt$	4.4453	1.6447	0.5764
$\int_0^{t_{\text{final}}} |\tau_1(t)|^2 \, dt$	3.817×10^4	5.673×10^4	1.181×10^6
$\int_0^{t_{\text{final}}} |\tau_2(t)|^2 \, dt$	5.094×10^4	1.271×10^5	4.889×10^6

The performance of the different adaptive controllers under a condition of 60% deficiency is given in Table 5.4, where the commanded torque is multiplied by a factor of 0.4. For the shoulder joint, the bound-based controller has the lowest error (0.2179), followed by the projection-based controller (0.3513), and the standard controller has the highest error (2.0778). Similarly, for the elbow joint, the projection-based controller has the lowest error (0.5764), while the standard controller has the highest error (4.4453). Also, when the total error is compared, the projection-based controller shows better performance than the bound-based controller and the bound-based controller shows better performance than the standard adaptive controller in a 60% deficiency case.

Again it can be seen that the standard controller has the lowest torque (3.817×10^4) for the shoulder joint, while the projection-based controller has the highest torque (1.181×10^6). Similarly, for the elbow joint, the standard controller also has the smallest commanded torque (5.094×10^4), but the projection-based controller had the highest torque (4.889×10^6).

In Table 5.5, an examination of the performance of the adaptive controllers under a condition of 80% deficiency is presented, where the commanded torque is multiplied by a factor of 0.2. Several

Table 5.5 Performance measurements comparing the adaptive controllers (80% deficiency).

80% Deficiency	Standard	Bound-based	Projection-based
$\int_0^{t_{\text{final}}} |e_1(t)|^2 \, dt$	11.2912	0.9543	0.2374
$\int_0^{t_{\text{final}}} |e_2(t)|^2 \, dt$	15.7847	6.6455	0.5831
$\int_0^{t_{\text{final}}} |\tau_1(t)|^2 \, dt$	3.102×10^4	3.633×10^4	2.623×10^5
$\int_0^{t_{\text{final}}} |\tau_2(t)|^2 \, dt$	2.773×10^4	4.383×10^4	1.195×10^6

important observations can be drawn from these results. For the shoulder joint, the projection-based controller has the lowest error (0.2374), followed by the bound-based controller (0.9543), and the standard controller has the highest error (11.2912). However, for the elbow joint, the projection-based controller also has the lowest error (0.5831), while the standard controller has the highest error (15.7847) When the total error is compared, the projection-based controller shows better performance than the bound-based controller and the bound-based controller shows better performance than the standard adaptive controller in an 80% deficiency case.

When it comes to the integral of the square of the norm of the commanded torque, the standard controller has the lowest torque (3.102×10^4 for τ_1 and 2.773×10^4 for τ_2), while the projection-based controller has the highest torque (2.623×10^5 for τ_1 and 1.195×10^6 for τ_2). Looking at the trend of the commanded torque values, it can be seen that the commanded torque values decrease as the deficiency increases. This is due to the commanded torque from the adaptive controller is being premultiplied by smaller numbers as deficiency increase resulting in less total commanded torque across the whole experimentation time.

The analysis of the performance of the different adaptive controllers under varying conditions of deficiency reveals several key trends. As the deficiency increases, the error for both the shoulder and elbow joints tends to increase for the standard controller, while, in some cases decreases, for the bound-based and projection-based controllers. This suggests that the latter two controllers are more effective in reducing tracking errors under conditions of high deficiency. Interestingly, the error from the projection-based controller does not seem to fluctuate as much when the deficiency is increased. This is not the case for the bound-based controller where there is a significant jump in error between the 60% and 80% cases.

In terms of the commanded torque, the standard controller consistently has the lowest values across all levels of deficiency. However, the commanded torque for the bound-based and projection-based controllers increases as the deficiency increases. This indicates that these controllers require more control effort to achieve their performance under conditions of high deficiency. As stated before, the magnitude of the control effort decreases as the deficiency increases; however, for the over-driven case, it is expected to have the highest magnitude of the commanded torque for all data sets, but this is not the case. The projection operator for both joints has a lower commanded torque and the bound-based operator for the shoulder has a lower torque. This could be because the controller is overcompensating when the deficiency is present but not too high.

In conclusion, the choice of controller may need to be tailored to the specific joint and the specific performance criteria. If the priority is to minimize error, the bound-based or projection-based controller may be more suitable. However, if the priority is to minimize torque, the standard controller may be more appropriate. These findings underscore the importance of a nuanced approach to the design of adaptive controllers, taking into account the specific requirements and constraints of each application.

5.2.2 Joint Angle Tracking Discussion

This section presents an in-depth analysis of system responses in relation to desired joint trajectories. It was observed that the system responses generally tracked the desired joint trajectories effectively. However, an increase in imposed actuator deficiencies corresponded to an increase in error for the standard and bound-based cases. Refer to Figures 5.1 - 5.10 and Tables 5.1 - 5.5 for details.

Several common results were identified across all data in this section. Initially, the conditions for these experimental tests were not perfectly zero or identical. Despite this, the system's transient response was capable of achieving steady-state oscillation by the first full amplitude peak. This is likely facilitated by a strategic implementation of the desired trajectories, which involved a multiplication by a rapidly decaying exponential. Also, the learning rate of the estimated actuator deficiency γ has a large effect on the transient response. In early experimentation, this value was set

to 25, which would often make the controller immediately unstable due to an aggressive transient response. The value of 0.5 was found to have the most desirable transient response, while $\hat{\delta}$ converges by the final time.

Furthermore, it was noted that the error was at its peak at the first full amplitude oscillation and decreased to a smaller error by the end of the test for all cases. Interestingly, when the actuator deficiency was set to 80%, an overshoot error was observed at the top of the oscillations for both joints, while at the bottom of the oscillations, an overshoot was observed for the shoulder and an undershoot for the elbow. This occurred for both controllers and only near the end of the experiment (see Figure 5.9). This is likely due to the system having a negative ω and a negative θ, corresponding to a downward motion of the end-effector. As the angular velocities decrease and reach 0, the elbow's joint angle does not get the opportunity to reach its most negative value before the end-effector starts to move upward.

Lastly, all responses exhibited some inherent oscillatory error, most evident in the error plots in Section 5.1.3. This is especially evident for the bound-based controller at large actuator deficiencies (see Figure 5.39). This is likely attributable to aggressive learning rates chosen for Γ and γ. A reduction in learning rates would likely result in a smoother system response but with increased error.

5.2.3 Joint Angular Velocities Discussion

The scrutiny of joint angular velocities uncovers a complex landscape, from which it is difficult to draw conclusions due to the large amount of variation. The angular velocities measured for both joints show substantial oscillations around the target ω. Refer to Figures 5.11 - 5.20 for details. However, this pattern is typical in the experimental data derived from robotic manipulators. It is essential to comprehend that these oscillations are not necessarily indicative of an issue, but rather a reflection of the aggressive learning rate implemented in the system alongside large stability gains. Consequently, the manipulator tracks the desired angle in a more abrupt manner rather than a smooth path. If a smoother tracking response is preferred, further gain scheduling and adjustments might be warranted.

An interesting observation to note is that the maximum angular velocity for the elbow joint is approximately 0.4 rad/s and a minimum of about -0.4 rad/s, with no significant fluctuation across different deficiency levels. A noticeable difference exists between the two adaptive controllers; it appears that the projector operator-based controller tends to maintain an ω of zero for longer durations, most prominently in Figure 5.20 for the measured shoulder angle when the desired angular velocity is negative. This could be due to the controller reaching the desired joint angle and subsequently overshooting more frequently with the projection-based operator.

5.2.4 Joint Errors Discussion

Upon analyzing the joint error plots, a stark contrast between the two controllers emerges. Refer to Figures 5.21 - 5.30 for details. The bound-based controller's error exhibits substantial oscillations around zero with some deficiencies, whereas the projection operator-based adaptive controller maintains a steadier course. Interestingly, as the experiment advances, both controllers tend to gravitate towards zero error. This trend underscores the notion that the longer the adaptive controller interacts with the system, the more the error diminishes.

A noteworthy observation arises when comparing the elbow joint error with that of the shoulder joint across all data-sets, regardless of the level of deficiency or the controller employed. The elbow joint error consistently leans towards more negative values. Furthermore, when dealing with higher deficiencies, as depicted in Figures 5.27, 5.28, 5.29, and 5.30, the error does not oscillate around zero but around a certain negative value. This pattern suggests a longer run time or in-depth gain tuning might be required for this error to oscillate around zero, or it might indicate that only a near zero error is achievable for these levels of actuator deficiencies.

5.2.5 Joint Torques Discussion

A compelling observation emerges when analyzing the commanded values of joint torques, particularly the change in torque magnitude as the deficiency increases. Refer to Figures 5.31 - 5.40 and Tables 5.1 - 5.5 for details. It is evident that the maximum commanded torque to the elbow joint, following the attainment of steady-state oscillations, is approximately 50 Nm with a 40% deficiency (as seen in Figure 5.36), and reduces to merely 10 Nm with an 80% deficiency (as

seen in Figure 5.40). This is, of course, also related to the scheduled control gains for a possible best case. While it is logical for the commanded control torque values to halve with increased efficiency, this does not account for a nearly fourfold reduction in the requisite torque to track the desired trajectory. The remarkable aspect here is that, even with a fraction of available torque, the controller can still drive the error towards zero.

A clear distinction arises when comparing the two update laws; the projection operator tends to utilize more torque to track desired joint angles. For instance, at a 40% deficiency, the bound-based controller commands less than half the torque commanded by the projection operator for both joints (see Figures 5.35 and 5.36). This serves as a good illustration of the trade-offs involved in gain tuning for improved system response.

5.2.6 Estimated Actuator Deficiencies Discussion

The crux of this thesis lies in the analysis of the behavior of the estimated actuator deficiency, as it represents the primary addition to the standard adaptive controller framework. As illustrated in Figures 5.41 - 5.50, there are several recurring patterns across all data sets. Notably, in all cases, the $\hat{\delta}$ for the elbow appears to converge more rapidly than the $\hat{\delta}$ for the shoulder. Furthermore, despite the actual estimated deficiency being within the bounds for all experiments, the estimated actuator deficiency invariably converges to one of the bounds.

The projection-based controller consistently causes the estimated actuator deficiency to converge to the lower bound of the projection operator, typically within 5 seconds of the start time. This observation may account for the close performance measures of the projection operators, as referenced in Tables 5.4 and 5.5. The increase in actual deficiency increases the error, but because the lower bound was set at -0.9 in the 20%, 40%, 60%, and 80% deficiency cases, which is very close to the actual deficiency in the 80% case, the error is reduced.

Another conclusion that can be drawn for the projection operator is that the $\hat{\delta}$ consistently exhibits some oscillation after it has converged to the lower bound. This is most evident in Figure 5.42, where it can also be seen that the estimation hits the upper bound before converging to the lower bound. This is also seen in a much more aggressive manner in the simulation results from

Figure 4.6. This is because the estimation is hitting the edge of the projection operator bound and rebounds inside of the selected ε. However, this is not a concern because, due to the nature of the projection operator, $\hat{\delta}$ is only guaranteed to be bounded and is not guaranteed to converge to the actual actuator deficiency.

The bound-based controller seems to always converge to the upper bound of the estimated actuator deficiency. However, the larger the actuator deficiency, the slower the convergence. This is most clearly shown by Figure 5.49, where the estimated shoulder deficiency does not seem to reach the upper bound in the 100-second experiment time. There are also small oscillations in the trajectory around the upper bound which probably correspond to the oscillation of the shoulder.

It also turns out that the bounds of the estimated actuator deficiency, $\hat{\delta}$, have a large impact on the tracking error of the system. This means that tighter the bounds result in smaller error of the system, and the more information that is known about the system, the better response that can be achieved. If not much in known about the system the bounds will be further apart, which could lead to a less accurate system response.

In conclusion, the analysis reveals that the projection-based and bound-based controllers exhibit distinct behaviors in terms of convergence speed and oscillatory behavior in the estimated actuator deficiency. The bounds of the estimated actuator deficiency, $\hat{\delta}$, significantly impact the system error, emphasizing the importance of accurate system knowledge for satisfactory performance.

5.2.7 Estimated Model Parameters Discussion

The analysis of the data uncovers a noteworthy observation: the estimated model parameters do not converge to their actual representative values. Refer to Figures 5.51 - 5.60 for details. This phenomenon, while anticipated given the adaptive control architecture, incites an inquiry into the potential convergence values for the mass and moment of inertia. It is crucial to note that the theoretical framework only assures the asymptotic convergence of the tracking error, not the convergence of estimated parameters to their true value.

The estimated model parameters appear to be converging to a common location for each case, albeit scaled by a certain factor. This is likely attributable to the invariant mathematical expressions

for the regressor matrix, as delineated in Equation 3.1, across experiments. For high deficiency cases, the estimated model parameters do not seam to converge; however they are converging slowly. If the system were to be tuned differently or allowed a longer run time, it would be more clear that the parameters are converging to constants.

Upon comparing the bound-based controller and the projection operator, a discernible pattern emerges. The bound-based controller seems to yield more oscillatory results in this dataset, while the projection operator demonstrates less oscillation.

6 Conclusion

This thesis presented a comprehensive study on the experimental results of the joint tracking problem of robotic manipulators with uncertain dynamical parameters and actuator deficiencies. Two novel adaptive controller formulations were used, tested by simulation, verified by experimentation, and compared. Both controllers demonstrated remarkable resilience, maintaining control of the robotic arm with up to 80% control input deficiencies.

The analysis of system responses and joint error plots revealed that both controllers tend to gravitate towards zero error as the experiment advances, underscoring the notion that the longer the adaptive controller interacts with the system, the more the error diminishes. However, a stark contrast was observed between the two controllers. The bound-based controller's error exhibited substantial oscillations around zero, whereas the projection operator-based adaptive controller maintained a steadier course.

A compelling observation emerged when analyzing the commanded values of joint torques. Even with a fraction of available torque, both controllers could still drive the error towards zero. This underscores the robustness and effectiveness of the proposed adaptive controllers, even under substantial actuator deficiencies. However, it was noted that if initial conditions deviated significantly from zero, the transient response failed to find a steady-state solution. This suggests that further investigations might be warranted to improve system response under such conditions.

The analysis of the estimated actuator deficiency behavior has provided significant insights into the performance of both the projection-based and bound-based controllers. The speed of convergence and the noise in the estimated actuator deficiency after convergence are key characteristics that differentiate the two controllers. The projection-based controller consistently converges to the lower bound, while the bound-based controller tends to converge to the upper bound. The rate of convergence and the final value of the estimated actuator deficiency are influenced by the actual actuator deficiency. Furthermore, the bounds of the estimated actuator deficiency, $\hat{\delta}$, have a substantial impact on the system error. The closer the bounds, the smaller the system error, implying that a better understanding of the system can lead to an improved response. Conversely,

a lack of knowledge about the system can result in wider bounds and potentially a less accurate system response. This analysis underscores the importance of more accurate system knowledge and appropriate controller selection in achieving an acceptable system performance. Future work could focus on output feedback-based controllers, task space controllers, and experimentation on other robotic platforms.

In conclusion, this work contributes to the field of robotics by proposing and validating two novel adaptive controller formulations that can effectively handle uncertainties in dynamical parameters and actuator deficiencies. The findings from this study provide valuable insights for future research in this area, particularly in terms of enhancing robustness and reducing errors in robotic manipulator control. Moreover, this work paves the way for numerous potential future explorations and unresolved issues. These encompass the extension of the results to collaborative or networked robotic systems, the management of nonlinear and time-dependent uncertainties, the development of output feedback controllers, and the integration of learning mechanisms. This research constitutes a foundational step towards further progress in this domain.

REFERENCES

[1] FAST Research Group, "FAST Lab," , 2023. URL `https://www.fastresearchgroup.com/`.

[2] Quanser, "QArm," , 2022. URL `https://www.quanser.com/products/Qarm/`, [Online; accessed April 2022].

[3] Robotis, "XM540-W270-T/R," `https://emanual.robotis.com/docs/en/dxl/x/xm540-w270/`, 2023. Accessed on November 5, 2023.

[4] Lewis, F. L., Dawson, D. M., and Abdallah, C. T., *Robot Manipulator Control: Theory and Practice*, Marcel Decker, Inc., New York, USA, 2003.

[5] Aly, I. A., Comeaux, S., Dogan, K. M., Tatlicioglu, E., and Zergeroglu, E., "On Adaptive Control of Robotic Manipulators with Actuator Deficiencies," *AIAA Scitech Forum*, San Diego, CA, 2023.

[6] Cheah, C., "Approximate Jacobian Robot Control With Adaptive Jacobian Matrix," *IEEE Conference on Decision and Control*, 2003, pp. 5859–5864.

[7] Cheah, C., Hirano, M., Kawamura, S., and Arimoto, S., "Approximate Jacobian Control for Robots With Uncertain Kinematics and Dynamics," *IEEE Trans. Rob. Autom.*, Vol. 19, No. 4, 2003, pp. 692–702.

[8] Cheah, C., Hirano, M., Kawamura, S., and Arimoto, S., "Approximate Jacobian Control With Task-Space Damping for Robot Manipulators," *IEEE Trans. Autom. Control*, Vol. 49, No. 5, 2004, pp. 752–757.

[9] Cheah, C., "Task-Space PD Control of Robot Manipulators: Unified Analysis and Duality Property," *Int. J. Rob. Res.*, Vol. 27, No. 10, 2008, pp. 1152–1170.

[10] Zergeroglu, E., Dawson, D., Walker, I., and Setlur, P., "Nonlinear Tracking Control of Kinematically Redundant Robot Manipulators," *IEEE/ASME Trans. Mechatronics*, Vol. 9, No. 1, 2004, pp. 129–132.

[11] Xian, B., De Queiroz, M., Dawson, D., and Walker, I., "Task Space Tracking Control of Robot Manipulators Via Quaternion Feedback," *IEEE Trans. Rob. Autom.*, Vol. 20, No. 1, 2004, pp. 160–167.

[12] Tatlicioglu, E., McIntyre, M., Dawson, D., and Walker, I., "Adaptive Nonlinear Tracking Control of Kinematically Redundant Robot Manipulators With Sub-Task Extensions," *IEEE International Conference on Decision and Control*, 2005, pp. 4373–4378.

[13] Tatlicioglu, E., McIntyre, M., Dawson, D., and Walker, I., "Adaptive Non-Linear Tracking Control of Kinematically Redundant Robot Manipulators," *Int.J.Rob.Autom*, Vol. 23, No. 2, 2008, pp. 98–105.

[14] Tatlicioglu, E., Braganza, D., Burg, T., and Dawson, D., "Adaptive Control of Redundant Robot Manipulators With Sub-Task Objectives," *American Control Conference*, 2008, pp. 856–861.

[15] Tatlicioglu, E., Braganza, D., Burg, T., and Dawson, D., "Adaptive Control of Redundant Robot Manipulators With Sub-Task Objectives," *Robotica*, Vol. 27, No. 6, 2009, pp. 873–881.

[16] Hara, S., Yamamoto, Y., Omata, T., and Nakano, M., "Repetitive control systems: A new type servo system for periodic exogenous signals," *IEEE Transactions on Robotics*, Vol. 33, No. 7, 1988, pp. 659–668.

[17] Tomizuka, M., Tsao, T., and Chew, K., "Discrete-time domain analysis and synthesis of repetitive controllers," *ASME Journal on Dynamic Systems, Measurement, and Control*, Vol. 111, 1989, pp. 353–358.

[18] Tsai, M., Anwar, G., and Tomizuka, M., "Discrete-time repetitive control for robot manipulators," *Proc. IEEE Int. Conf. Robot. Autom.*, 1988, pp. 1341–1347.

[19] Messner, W., Horowitz, R., Kao, W., and Boals, M., "A new adaptive learning rule," *IEEE Tr. on Autom. Contr.*, Vol. 36, 1991, pp. 188–197.

[20] Horowitz, R., "Learning control of robot manipulators," *ASME J. Dyna. Syst., Meas. Contr.*, Vol. 115, 1993, pp. 402–411.

[21] Sadegh, N., and Horowitz, R., "Stability and robustness analysis of a class of adaptive controllers for robot manipulators," *Int. J. Robotics Research*, Vol. 9, No. 3, 1990, pp. 74–92.

[22] Dixon, W., Zergeroglu, E., Dawson, D., and Costic, B., "Repetitive learning control : A Lyapunov–based approach," *IEEE Tr. on Systems, Man, and Cybernetics*, Vol. 32, No. 4, 2002, pp. 538–545.

[23] Dogan, K., Tatlicioglu, E., Zergeroglu, E., and Cetin, K., "Lyapunov-based output feedback learning control of robot manipulators," *2015 American Control Conference (ACC)*, 2015, pp. 5337–5342.

[24] Dogan, E., K.M.and Tatlicioglu, and Zergeroglu, E., "Operational/task space learning control of robot manipulators with dynamical uncertainties," *2015 IEEE Conference on Control Applications (CCA)*, 2015, pp. 527–532.

[25] Dogan, K., Tatlicioglu, E., Zergeroglu, E., and Cetin, K., "Learning control of robot manipulators in task space," *Asian Journal of Control*, Vol. 20, No. 3, 2018, pp. 1003–1013.

[26] Tee, K., and Yan, R., "Adaptive Operational Space Control of Redundant Robot Manipulators," *American Control Conference*, 2011, pp. 1742–1747.

[27] Galicki, M., "Inverse-Free Control of a Robotic Manipulator in a Task Space," *Robot.Auton.Syst*, Vol. 62, No. 2, 2014, pp. 131–141.

[28] Koropouli, V., Gusrialdi, A., and Hirche, D., "An Extremum Seeking Control Approach for Constrained Robotic Motion Tasks," *Control Eng.Pract.*, Vol. 52, 2016, pp. 1–14.

[29] Rugthum, T., and Tao, G., "An adaptive actuator failure compensation scheme for a cooperative manipulator system with parameter uncertainties," *IEEE Conf. on Decision and Control*, 2015, pp. 6282–6287.

[30] Liu, G., "Control of robot manipulators with consideration of actuator performance degradation and failures," *IEEE Int. Conf. on Robotics and Automation*, 2001, pp. 2566–2571.

[31] De Luca, A., and Mattone, R., "Actuator failure detection and isolation using generalized momenta," *IEEE Int. Conf. on Robotics and Automation*, 2003, pp. 634–639.

[32] Jin, X., "Adaptive fault tolerant control for a class of multi-input multi-output nonlinear systems with both sensor and actuator faults," *Int. J. of Adaptive Control and Signal Processing*, Vol. 31, No. 10, 2017, pp. 1418–1427.

[33] Elghoul, A., Tellili, A., Bouziri, A., and Abdelkrim, M. N., "A fault tolerant control for robot manipulators against actuator fault," *Int. Conf. on Sciences and Techniques of Automatic Control and Computer Engineering*, 2017, pp. 218–222.

[34] Gruenwald, B. C., Wagner, D., Yucelen, T., and Muse, J. A., "Computing actuator bandwidth limits for model reference adaptive control," *Int. J. of Control*, Vol. 89, No. 12, 2016, pp. 2434–2452.

[35] Gruenwald, B. C., Dogan, K. M., Yucelen, T., and Muse, J. A., "A model reference adaptive control framework for uncertain dynamical systems with high-order actuator dynamics and unknown actuator outputs," *Dynamic Systems and Control Conference*, Vol. 58271, American Society of Mechanical Engineers, 2017, p. V001T15A003.

[36] Dogan, K. M., Yucelen, T., and Muse, J. A., "On Asymptotic System Error Convergence of Model Reference Adaptive Control Architectures in the Presence of Unmeasurable Coupled Dynamics," *American Control Conf.*, 2020, pp. 2496–2501.

[37] Cheah, C. C., Liu, C., and Slotine, J. J. E., "Adaptive Jacobian Tracking Control of Robots With Uncertainties in Kinematic, Dynamic and Actuator Models," *IEEE Tr. on Automatic Control*, Vol. 51, No. 6, 2006, pp. 1024–1029.

[38] Driessen, B. J., "Adaptive global tracking for robots with unknown link and actuator dynamics," *Int. J. of Adaptive Control and Signal Processing*, Vol. 20, 2006, pp. 123–138.

[39] Liu, L., Zhang, L., Wang, Y., and Hou, Y., "A novel robust fixed-time fault-tolerant tracking control of uncertain robot manipulators," *IET Control Theory & Applications*, Vol. 15, 2021, pp. 195–208.

[40] Dasdemir, J., and Zergeroglu, E., "A new continuous high-gain controller scheme for a class of uncertain nonlinear systems," *Int. J. of Robust and Nonlinear Control*, Vol. 25, 2013, pp. 125–141.

[41] Dogan, K. M., Tatlicioglu, E., Zergeroglu, E., and Cetin, K., "Lyapunov-based output feedback learning control of robot manipulators," *American Control Conf.*, 2015, pp. 5337–5342.

[42] Dogan, K. M., Tatlicioglu, E., and Zergeroglu, E., "Operational/task space learning control of robot manipulators with dynamical uncertainties," *IEEE Conf. on Control Applications*, 2015, pp. 527–532.

[43] Dogan, K. M., Yucelen, T., and Muse, J. A., "An asymptotic decoupling approach for adaptive control with unmeasurable coupled dynamics," *Int. J. of Adaptive Control and Signal Processing*, Vol. 35, No. 3, 2021, pp. 342–356.

[44] Khalil, H. K., *Nonlinear Systems*, Prentice-Hall, Upper Saddle River, NJ, 1996.

[45] Lavretsky, E., and Wise, K. A., "Robust Adaptive Control," *Robust and Adaptive Control*, Springer, 2013.

[46] Zergeroglu, E., and Tatlicioglu, E., "Observer based adaptive output feedback tracking control of robot manipulators," *IEEE Conf. on Decision and Control*, 2010, pp. 3638–3643.